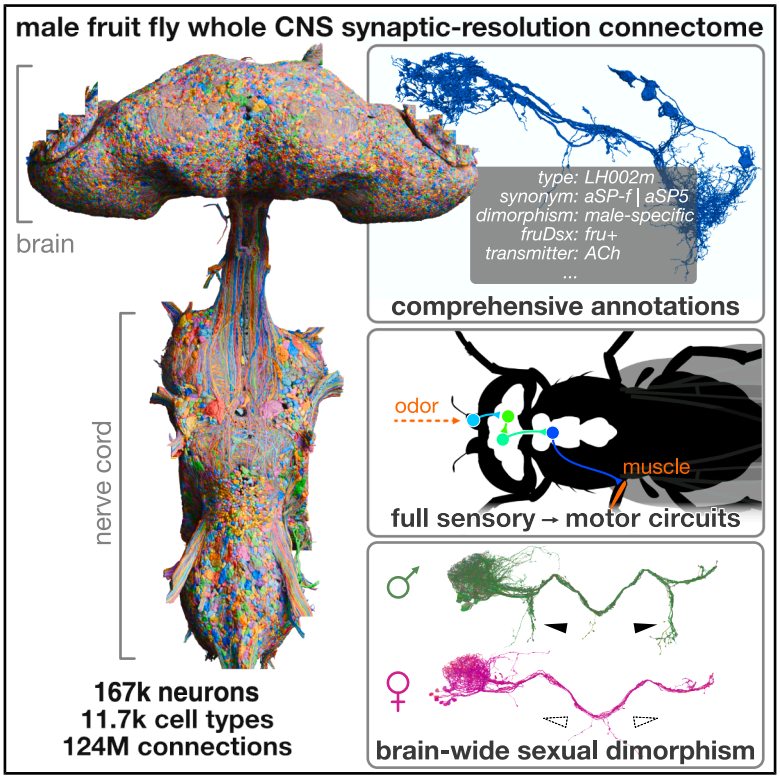
Cell

Sexual dimorphism in the complete *Drosophila* male central nervous system connectome

Graphical abstract



Highlights

- Whole male *Drosophila* CNS connectome enables sensory-to-motor circuit analysis
- First synaptic-resolution comparison of male and female brains
- Sex-specific and dimorphic neurons concentrate in higher-order, integrative centers
- Analysis of visual, auditory, olfactory, and taste pathways reveals shared principles

Authors

Stuart Berg, Isabella R. Beckett, Marta Costa, Philipp Schlegel, ..., Harald F. Hess, Gerald M. Rubin, Gregory S.X.E. Jefferis

Correspondence

bergs@janelia.hhmi.org (S.B.), rubing@janelia.hhmi.org (G.M.R.), jefferis@mrc-lmb.cam.ac.uk (G.S.X.E.J.)

In brief

The *Drosophila* whole male central nervous system connectome enables end-to-end analysis of sensorimotor circuits. Comparison with existing female datasets shows that brain-wide wiring differences between the sexes are concentrated in higher centers.

Berg et al., 2026, Cell *189*, 5504–5526
September 3, 2026 © 2026 MRC Laboratory of Molecular Biology.
Published by Elsevier Inc.
https://doi.org/10.1016/j.cell.2026.08.015

CellPress

CellPress
OPEN ACCESS

Cell

Article

Sexual dimorphism in the complete *Drosophila* male central nervous system connectome

Stuart Berg,[1,2,14,*] Isabella R. Beckett,[3,14] Marta Costa,[4,14] Philipp Schlegel,[3,4,14] Michał Januszewski,[5,14] Elizabeth C. Marin,[4,14] Aljoscha Nern,[1,14] Stephan Preibisch,[1,2,14] Wei Qiu,[1,2,14] Shin-ya Takemura,[1,2,14] Alexandra M.C. Fragniere,[4,14] Andrew S. Champion,[3,4,15] Diane-Yayra Adjavon,[1,15] Michael Cook,[1,2,15] Marina Gkantia,[4,15] Kenneth J. Hayworth,[1,2,15] Gary B. Huang,[1,2,15] William T. Katz,[1,2,15] Florian Kämpf,[3,15] Zhiyuan Lu,[1,2,15] Christopher Ordish,[1,2,15] Tyler Paterson,[1,2,15] Tomke Stürner,[3,15] Eric T. Trautman,[1,2,15] Catherine R. Whittle,[3,15] Laura E. Burnett,[1] Judith Hoeller,[1] Feng Li,[1,2] Frank Loesche,[1] Billy J. Morris,[4] Tobias Pietzsch,[1] Markus W. Pleijzier,[3,4] Valeria Silva,[7] Yijie Yin,[6] Iris Ali,[1,2] Griffin Badalamente,[4] Alexander Shakeel Bates,[7,12] Rory J. Beresford,[9] John Bogovic,[1] Paul Brooks,[4] Sebastian Cachero,[3] Brandon S. Canino,[1,2] Bhumpanya Chaisrisawatsuk,[3] Jody Clements,[1,2] Arthur Crowe,[1] Inês de Haan Vicente,[9] Georgia Dempsey,[7] Erika Donà,[8,3] Márcia Dos Santos,[4] Marisa Dreher,[1] Christopher R. Dunne,[4] Katharina Eichler,[4] Samantha Finley-May,[1,2] Miriam A. Flynn,[1,2] Imran Hameed,[1,2] Gary Patrick Hopkins,[1,2] Philip M. Hubbard,[1,2] Ladann Kiassat,[4] Julie Kovalyak,[1,2] Shirley A. Lauchie,[1,2] Meghan Leonard,[1,2] Alanna Lohff,[1,2] Kit D. Longden,[1] Charli A. Maldonado,[1,2] Ilina Moitra,[4] Sung Soo Moon,[4] Caroline Mooney,[1,2] Eva J. Munnelly,[4] Nneoma Okeoma,[1,2] Donald J. Olbris,[1,2] Anika Pai,[4] Birava Patel,[1,2] Emily M. Phillips,[1,2] Stephen M. Plaza,[1,2] Alana Richards,[4] Jennifer Rivas Salinas,[1,2] Ruairí J.V. Roberts,[13] Edward M. Rogers,[1] Ashley L. Scott,[1,2] Louis A. Scuderi,[1,2] Pavithraa Seenivasan,[1] Laia Serratosa Capdevila,[13] Claire Smith,[1,2] Rob Svirskas,[1,2] Satoko Takemura,[1,2] Ibrahim Tastekin,[9] Alexander Thomson,[1,2] Lowell Umayam,[1,2] John J. Walsh,[1,2] Holly Whittome,[4] C. Shan Xu,[1,2] Emily A. Yakal,[1,2] Tansy Yang,[1,2] Arthur Zhao,[1] Reed George,[1,2] Viren Jain,[11] Vivek Jayaraman,[1,2] Wyatt Korff,[1,2] Geoffrey W. Meissner,[1,2] Sandro Romani,[1] Jan Funke,[1,2] Christopher Knecht,[1,2] Stephan Saalfeld,[1] Louis K. Scheffer,[1,2] Scott Waddell,[7] Gwyneth M. Card,[2,10] Carlos Ribeiro,[9] Michael B. Reiser,[1] Harald F. Hess,[1,2] Gerald M. Rubin,[1,2,*] and Gregory S.X.E. Jefferis[3,4,2,16,*]

[1]Janelia Research Campus, Howard Hughes Medical Institute, Ashburn, VA 20147, USA
[2]Janelia FlyEM Project Team, Howard Hughes Medical Institute, Ashburn, VA 20147, USA
[3]Neurobiology Division, Medical Research Council Laboratory of Molecular Biology, Cambridge CB2 0QH, UK
[4]Department of Zoology, University of Cambridge, Cambridge CB3 3EJ, UK
[5]Google Research, Google LLC, 8004 Zürich, Switzerland
[6]Department of Physiology, Development and Neuroscience, University of Cambridge, Cambridge CB2 3EG, UK
[7]Centre for Neural Circuits and Behaviour, University of Oxford, Oxford OX1 3SR, UK
[8]Institute of Neuroscience, Consiglio Nazionale delle Ricerche (CNR), 20854 Vedano al Lambro, MB, Italy
[9]Champalimaud Foundation, 1400-038 Lisbon, Portugal
[10]Zuckerman Institute, Columbia University, New York, NY 10027, USA
[11]Google Research, Mountain View, CA 94043, USA
[12]Department of Neurobiology, Harvard Medical School, Boston, MA 02115, USA
[13]Aelysia Ltd., Bristol BS9 3BY, UK
[14]These authors contributed equally
[15]These authors contributed equally
[16]Lead contact
*Correspondence: bergs@janelia.hhmi.org (S.B.), rubing@janelia.hhmi.org (G.M.R.), jefferis@mrc-lmb.cam.ac.uk (G.S.X.E.J.)
https://doi.org/10.1016/j.cell.2026.08.015

SUMMARY

Sex differences in behavior exist across all animals, typically under strong genetic regulation. In *Drosophila*, *fruitless/doublesex* transcription factors identify dimorphic neurons, but their organization into functional circuits remains unclear. We present the connectome of the entire *Drosophila* male central nervous system. This contains 166,700 neurons spanning the brain and nerve cord, fully proofread and annotated, including *fruitless/doublesex* expression and 11,710 neuron types. We provide the first comprehensive comparison between male and female brain connectomes to synaptic resolution, finding 8,069 isomorphic, 138 dimorphic, 289 male-specific, and 71 female-specific types. This resource enables analysis of full sensory-to-motor circuits underlying complex behaviors and the impact of dimorphic elements. Sex-specific/dimorphic neurons are concentrated in higher brain centers, while the sensory and motor periphery is largely isomorphic. Within higher centers, male-specific connections are organized into hotspots defined by male-specific neurons or arbors. Dimorphic neurons reroute information across sexes.

 © 2026 MRC Laboratory of Molecular Biology. Published by Elsevier Inc.
This is an open access article under the CC BY license (http://creativecommons.org/licenses/by/4.0/).

INTRODUCTION

To understand how brains transform sensory information and memories into motor actions, we must define the composition and organizational logic of neural circuits and test the functional consequences of circuit manipulation. Sexual dimorphisms provide a natural experimental framework for causal inference. For example, virgin male and female mice respond differently to pups: females parent, but males are infanticidal. These antagonistic behaviors are controlled by a sexually dimorphic population of inhibitory neurons in the medial amygdala.[1] Dissecting the differences in the underlying neural circuits could offer general insights into how the brain produces behavior. But while studies in rodents[2–8] have identified brain regions and broad cell populations implicated in dimorphic behaviors, mapping the entire underlying circuit architecture remains intractable.

The adult fruit fly, *Drosophila melanogaster*, is a powerful model for studying sexual dimorphism from genes to circuits and behavior. Dimorphic behaviors such as courtship and aggression depend on complex sensorimotor integration. Although genetically specified by *fruitless* and *doublesex*,[9–11] they can be modified by experience.[12,13] Molecular genetic toolkits provide access to highly specific cell types expressing these transcription factors, enabling precise dissection of their contributions to many sexually dimorphic behaviors.[14–18]

Until now, studies of sexual dimorphism in *Drosophila* have focused on the impact of individual cell types on physiology and behavior.[19–21] For example, male-specific pC1 neurons, a diverse population expressing *doublesex* and, in some cases, also *fruitless*, promote courtship song[20,22–24] and aggression.[25] pC1 neurons are a key node controlling sex-specific behavior, with strong parallels to mammals,[26] but the circuit architecture that allows them to promote mutually exclusive behaviors remains elusive. In a few exceptional cases, it has been possible to pinpoint circuit nodes that redirect sensory information to opposing downstream circuitry.[27,28]

Connectomes of the fly brain and nerve cord[29–34] now provide a systematic approach to address this circuit gap, placing individual neurons into complete, brain-wide, synaptic-resolution circuits. These static wiring diagrams are transforming investigation of complex behavior in *Drosophila*,[35] even including cognitive processes such as memory that reflect individual life history or the dynamic interaction between visual attention and internal state.[36]

Building on this foundation, we present the first finished connectome of an entire male *Drosophila* central nervous system (CNS). This provides two critical advances: (1) a fully proofread and annotated brain and nerve cord connectome with an intact neck connective and (2) the first example of a male brain. This enables the first brain-wide, synaptic-resolution comparison across sexes of an adult animal with complex anatomy and behavior. We identified several hundred sex-specific and sexually dimorphic cell types, comprising 4.8% of neurons in the male and 2.4% of neurons in the female central brain. We found a high (but not perfect) correspondence between dimorphism status and *fruitless*/*doublesex* expression. Sex-specific and dimorphic neurons are concentrated in higher-order brain centers, while the sensory and motor periphery is largely isomorphic. Although only a small fraction of neurons are overtly dimorphic, they connect with many isomorphic neurons, suggesting that even modest sex differences can exert brain-wide influence. Comparative connectomics of multiple sensory and behavioral circuit modules uncovers general principles of the neural architecture for sex-shared, sex-specific, and flexible behaviors. This resource enables exploration of neural circuits spanning the entire CNS and comparison across sexes to elucidate the circuit-level impact of sexual dimorphism.

RESULTS

A complete connectome of a whole male CNS

We present the fully proofread CNS connectome of an adult *Drosophila melanogaster* male. Using 7 enhanced focused ion beam scanning electron microscopy (eFIB-SEM) systems[37,38] over 13 months, we extended the right optic lobe connectome[39] to generate a 160 teravoxel image volume at $8\times8\times8$ nm isotropic resolution encompassing the central brain, optic lobes, and ventral nerve cord (VNC, insect spinal cord analog) (Figure 1A). After alignment, neurons were automatically segmented with flood-filling networks,[40] and 46 million presynapses connected to 312 million postsynapses were detected with a precision/recall of 0.82/0.81 (Figure S1I; STAR Methods). We extracted additional features, including nuclei and neurotransmitter predictions[41] (Figures S1J and S1K).

The initial neuron segmentation was proofread with an estimated effort of 44 person-years (Figure S8; STAR Methods). In total, we identified, proofread, and annotated 166,700 neurons (including sensory axons) across the entire volume (Figure 1B; Video S1). While absolute certainty is difficult in datasets of this size, we are confident that these numbers represent essentially all traceable neurons (Figure 1E; see STAR Methods). Connectome completeness is typically assessed by the fraction of pre- and postsynapses associated with proofread neurons. With 94% pre- and 42% postsynaptic completion rates, this dataset is similar to or exceeds previously published connectomes[29–31,33,34] (Figures 1C and S8G). Most connectivity analyses focus on proofread neurons, so the fraction of synaptic connections for which both pre- and postsynaptic sites belong to a proofread neuron may be a more useful statistic: it is 40.1% for the male CNS (Figure 1D). This proofread connectome containing 124.2M synaptic connections defines a graph of 25.6M edges between 166,483 neurons (217 neurons without synapses are disconnected).

To maximize utility, we provide comprehensive annotations detailing the organization and structure of the entire *Drosophila* CNS, cross-referenced with recent partial connectome datasets. The coarsest annotation, "*superclass*," describes the direction of information flow, anatomical location, and broad function of neurons. Orthogonal annotations include developmental origin (*hemilineage*), spatial location (*somaSide*, *somaNeuromere*, *entry/exitNerve*), putative function (*class* and *subclass*), and names from the literature (*synonyms*) (Figures 1F and S1B–S1D). At the most granular level, we defined 11,710 unique cell types based on neuron morphology and connectivity across the CNS (Figures 1G and S1A).

To enable across-dataset comparisons, we used NBLAST[42] morphology scores and connectivity similarity[30] to systematically

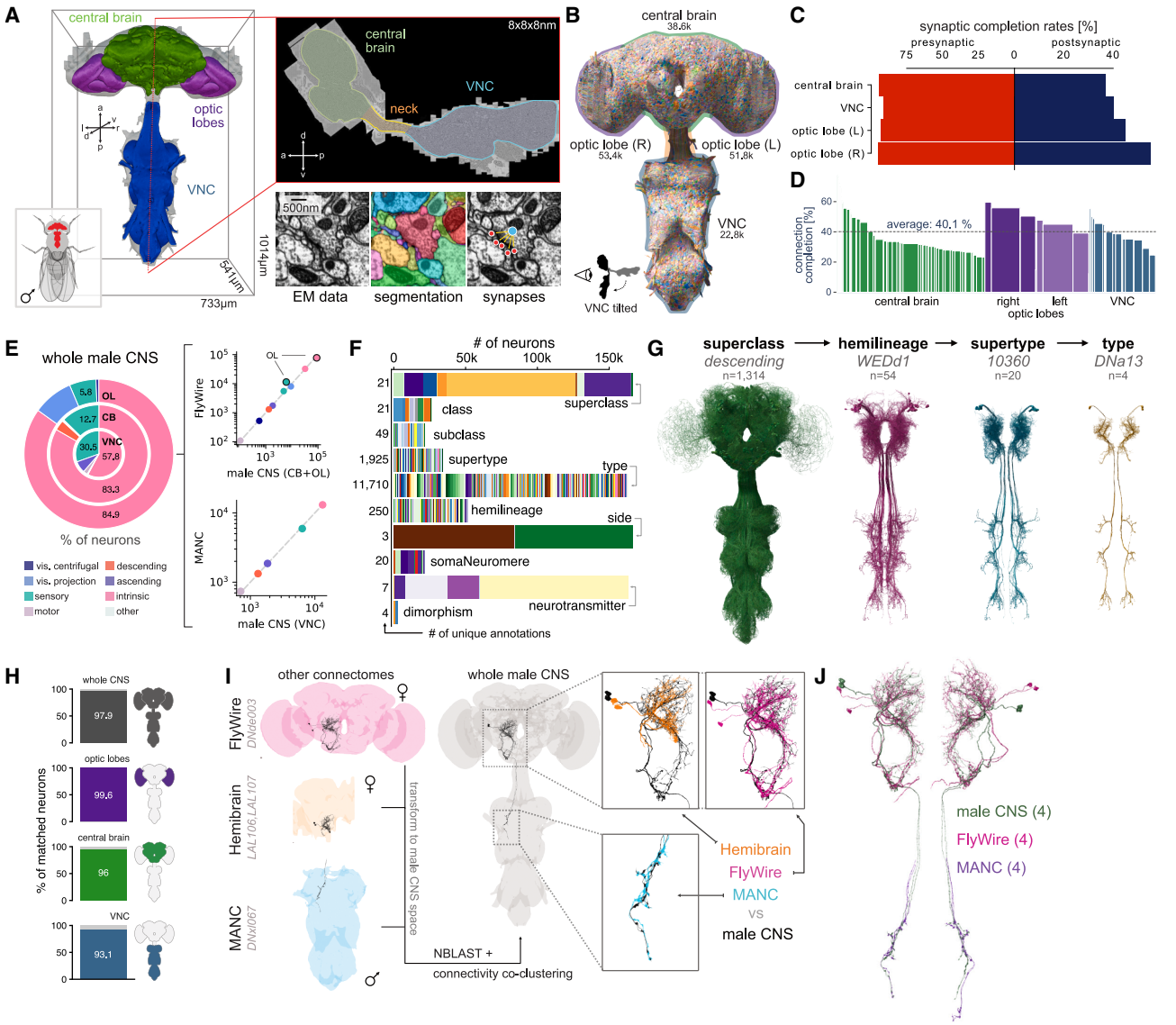


Figure 1. A densely annotated and cross-matched male CNS connectome

(A) Outlines of the aligned male CNS volume (0.082 mm^3), colored by CNS region (left). Sagittal slice through the EM image data (top right). Insets show (from left): image data, neuron segmentation, and synapse detection. Scale bar: 500 nm.

(B) 3D rendering of all neurons in the connectome. Frontal view: VNC tilted down for visualization. Numbers represent neuron counts per brain region, including sensory neurons.

(C) Synaptic completion rates for pre- and postsynapses per brain region.

(D) Percentage of connections where both pre- and postsynaptic partners are proofread, broken down by neuropil region. Bar width corresponds to the size of the neuropil.

(E) Percentages of neurons for main superclasses across brain regions (left). Neuron counts match those in existing connectomes: female brain (FAFB/FlyWire, top right) and male nerve cord (MANC, bottom right).

(F) Number of neurons per annotation field. The number of unique annotations for each field is shown at the top of the bar. *side* combines fields *somaSide* and *rootSide*. *hemilineage* combines fields *itoleeHl* and *trumanHl*.

(G) Example of the hierarchical annotation of neurons, from *superclass* through *hemilineage*, *supertype*, and *type*. The annotation and the number of neurons in that category are shown in gray.

(H) Percentage of neurons matched to an existing dataset in the whole male CNS and for each CNS region.

(I) Neurons were matched to existing connectomes using a combination of spatial transforms + NBLAST and connectivity co-clustering. Example shown here is DNde003, a descending neuron type, with a 1:1 match in FlyWire and MANC and matched to two types in the hemibrain.

(J) Full view of DNde003 in male CNS, FlyWire, and MANC. The number of neurons in each dataset is shown in brackets. EM, electron microscopy; OLs, optic lobes; CB, central brain; MANC, male adult nerve cord connectome; VNC, ventral nerve cord.

See also Figures S1 and S8.

match and annotate cell types across existing connectomes (Figures 1H–1J; see STAR Methods for details). 97.9% of neurons across the CNS have a cell type match to either the FAFB/FlyWire,[29,30,43] hemibrain,[31] and/or male adult nerve cord (MANC)[33,34] datasets (Figures 1H and S1E). Of the remaining 2.1%, some remain unmatched due to limitations of previous partial datasets (Figure S1F; STAR Methods). Male-specific neurons are presented later.

We matched cell types across connectomes with high fidelity, but nomenclature is not yet consistent. We therefore recorded parallel type annotations for other datasets (*mancType*, *flywireType*, and *hemibrainType*) so that the male CNS annotations now serve as a connectomic Rosetta Stone. We revised some cell types in FAFB/FlyWire, hemibrain, and/or MANC when whole-CNS information enabled more accurate cell typing (Figure S1H; see STAR Methods for downloads). Reassuringly, cell type definitions are converging: we revised just 4.6% of FlyWire types (Figure S1H), whereas in earlier work matching the hemibrain and FlyWire, we had to revise over 44% of cell types.[30] The male CNS therefore represents the most accurate and durable consensus cell type atlas to date.

Based on the combination of high-quality connectivity and comprehensive annotation, we believe the male CNS should be the principal reference for researchers exploring the anatomy, connectivity, and development across the *Drosophila* CNS and for unraveling the structure-function relationships linking circuits to behavior. A landing page brings together all resources (raw images, segmentation, neuron reconstructions, connectome graphs, neurotransmitter predictions, annotations, etc.) with interactive tools to explore cell types, connectivity, and male-female dimorphism (see also STAR Methods).

Information flow from sensory to motor

Using a limited repertoire of sensors (sensory neurons) and effectors (motor neurons), flies flexibly perform complex behaviors, including navigation, aggression, and courtship.[24,44–48] We annotated sensory and motor neurons across the brain and nerve cord (Figure 2A), including receptor subtypes for sensory neurons and the exit nerve and muscle innervation of motor neurons (Figure S2A), enabling investigation of full sensorimotor circuits.

Figure 2B gives a bird's-eye view of information flow across the connectome, ordered from sensory to motor. Feedforward connections share similar, predominantly excitatory neurotransmitter compositions, while feedback connections (e.g., central brain to optic lobes) are more inhibitory. The neck connective is a key bottleneck, with descending neurons (DNs) constraining flow from brain to VNC and ascending neurons (ANs) constraining in the reverse. These neurons are also integrators: ascending neurons receive more input from VNC-intrinsic neurons than from direct sensory sources and make as many synapses onto VNC-intrinsic neurons as descending neurons. Although connectivity between superclasses is principally feedforward, neck connective neurons account for most of the feedback in the system.

To investigate how information flows through the nervous system, we implemented an end-to-end maximum flow analysis, a common network analysis technique[49] that finds the greatest possible rate of information flow from a source to a destination without exceeding capacity limits (synaptic weights) of the connections (Figure 2C; see STAR Methods for comparison and details). We focus here on the neck connective given its distinctive role in constraining and integrating information.

Starting from all sensory neurons of a particular modality *class* (source) and terminating at motor neurons from each motor domain *subclass* (target) (Figures 2A, 2C, and S2B), we identified the flow over all neck connective neurons for all pairs of sensory modalities and motor domains on a presynaptic-input-normalized connectome graph. For example, DNp44 descending neurons have high maximum flow to many motor domains from olfactory and hygrosensory neurons, indicating that they may combine information from these modalities (Figures 2D, S2C, and S2D). A detailed analysis of information flow through the neck connective bottleneck is presented in Data S1.

To better understand the logic of information flow through the neck connective, we clustered all descending and ascending neurons based on an embedding of their sensorimotor flows (Figures 2E and S2E). Some clusters are predominantly ascending or descending or have high specificity to a single sensory modality or motor domain, but many are heterogeneous (Figure S2F). Cell types with known functions in the literature were sorted into broad behavioral categories, which often correlated with the clusters (Figure 2F). This method therefore reliably captures known behaviors and will help generate new functional hypotheses.

Identifying sexually dimorphic circuit elements

Sex differences in behavior depend on unique circuit elements, sex-specific wiring, and sex-dependent cell physiology within[27,50–52] and beyond the nervous system.[53] Connectomics enables comparison of all structural differences in the nervous system at synaptic resolution. To distinguish sex-specific or dimorphic from sex-shared circuit elements, we compared our male dataset with existing female connectomes: FAFB/FlyWire[29,30,43] (brain only) (Figure 3A) as a principal reference and hemibrain[31] (approximately half a central brain) for confirmation. Cell types (most consisting of multiple neurons) are the fundamental unit of conservation across brains and hemispheres.[30,54,55] We assigned a male-female type match for 96.1% of neurons in the central brain and 99.7% of the optic lobe (Figures 1H and S1E), spanning both isomorphic and dimorphic neurons. Unmatched neurons were candidate sex-specific types. It was crucial to have specific operational definitions for these categories (Figures 3B and 3C). Isomorphic neurons share a developmental origin and lack consistent morphological sex differences (Figure 3D). Dimorphic neurons also share a developmental origin and are present in all four hemispheres but show clear, consistent sex differences in morphology (Figure 3F). By contrast, sex-specific neurons are present in both hemispheres of one sex, but their closest neurons from the opposite sex have a better isomorphic or dimorphic match (Figure 3E). We investigate "secondarily dimorphic" neurons that are morphologically isomorphic but still make sex-specific connections later in the results. Lacking a fully proofread female VNC connectome, we extended dimorphism labels from prior VNC literature,[28,56,57–61] especially Stürner et al.[62]

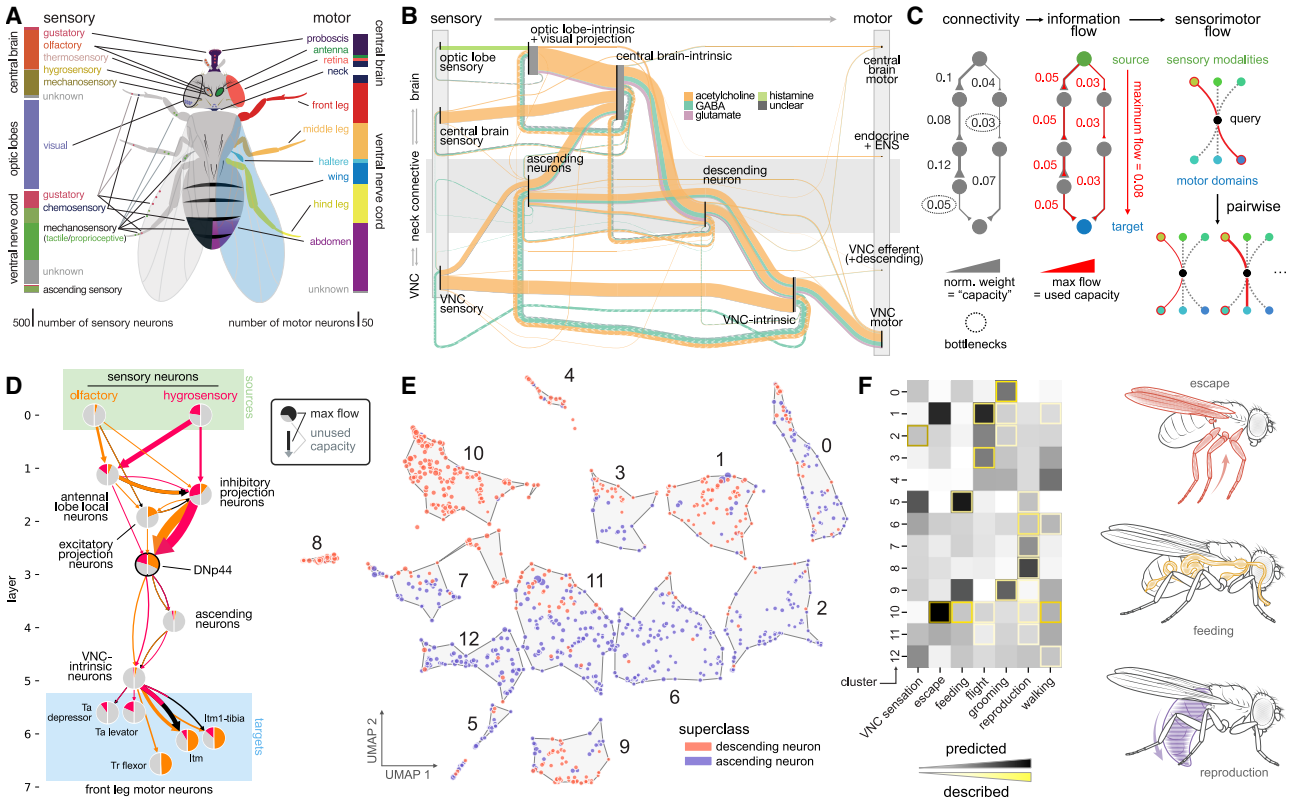


Figure 2. Information flow from sensory input to motor output organizes circuits spanning the brain and nerve cord

(A) Schematic of sensory groups (by *class*) and motor groups (by *subclass*). Bars: number of neurons per group.

(B) Directed flow diagram of connections from sensory to motor (and endocrine) through the CNS. Colors indicate neurotransmitter identity, and dashed lines show feedback connections. Edge width proportional to the number of synapses between groups, node width proportional to synaptic connections within each group. Edges with fewer than 20k synapses omitted.

(C) Schematic of maxflow analysis. Left: normalized edge weights establish potential information flow capacities between nodes. Middle: maxflow assignment of flow value across each edge. Flow is constrained by the minimum capacity along a path. Right: pairwise sensory→motor flow is calculated for all neurons across all sensorimotor pairings.

(D) Example of maxflow routes from olfactory (orange) and hygrosensory (red) inputs to front leg motor outputs. Strong flow partners (by type/class) upstream and downstream of example neurons in type DNp44.

(E) Uniform manifold approximation and projection (UMAP) embedding of DN and AN types by sensorimotor flow, colored by superclass and sized by presynaptic sites, outlined by numbered clusters.

(F) Behavioral categorization of clusters predicted by max flow analysis.

See also Figure S2.

These criteria identified 1,420 sex-specific neurons across the male CNS versus 363 female-specific neurons in FAFB/FlyWire (Table 1; Figure 3H). 948 dimorphic neurons in the male CNS matched 813 neurons in the female. While we expected the same number in both sexes, the discrepancy is explained by biological variability, especially in the numbers of optic lobe columns[39] (male CNS ~900; FAFB ~800). A relatively modest 0.1% of neurons in the male visual system are sex-specific, and 0.3% are sexually dimorphic (Table 1; Figure S3G). In the male central brain, dimorphism is much more prevalent: 3.4% of neurons are male-specific, and 1.4% are sexually dimorphic (Table 1; Figure 3I). By contrast, female-specific neurons make up only 1% of the central brain.

Where do sex-specific neurons originate? Female-specific neuronal apoptosis during pupal development is a key mechanism[63,64] but is not evenly distributed. Of the ~200 hemilineages forming the central brain,[65,66] about a quarter produce sex-specific or sexually dimorphic neurons, but just eight (4%) produce more than half of all sex-specific and dimorphic neurons (Figures 3J and S3I). For example, the DM4 dorsal lineage has 349 neurons in males versus 202 in females, but excluding sex-specific neurons, counts are almost identical across sexes (198 versus 201). Approximately 8% of sexually dimorphic and sex-specific neurons are primary (i.e., early-born neurons that function in the larva) (Figure S3I).

Topology of sexual dimorphism

We observed three categories of morphological differences in dimorphic neurons: completely new arbors, shifts, and expansions of existing branching patterns. These features were sometimes combined (Figure 3G). AOTU008 (part of aSP-i[56]) is a clear example of new arbors: it has ventral axonal projections in males that are completely absent in females (Figure 3F).[28] As expected,

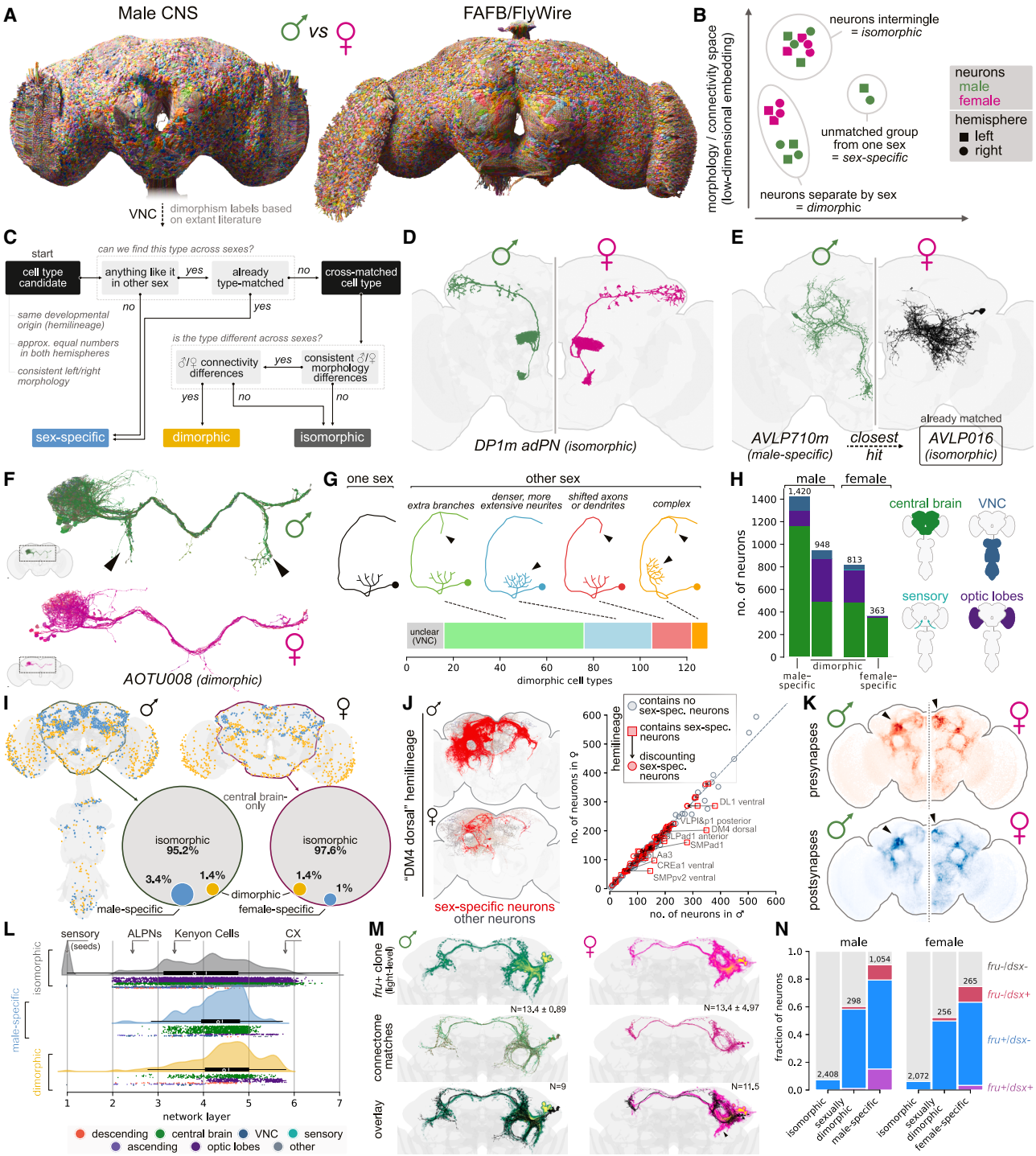


Figure 3. Sexual dimorphism in the fly brain

(A) Comparing the male CNS against the female FAFB/FlyWire connectome.

(B) Differences between iso-, dimorphic, and sex-specific neurons in morphology or connectivity space.

(C) Decision tree for assigning dimorphism labels.

(D–F) Examples for isomorphic (D), sex-specific (E), and dimorphic (F) cell types. Arrowheads in (F) highlight ventro-lateral axons only present in the male. (E) shows the closest isomorphic cell type (AVLP016) for comparison (see Figure S3F for the male version).

(G) Categories of morphological difference for dimorphic central brain cell types. "Unclear (VNC)" indicates differences in the VNC (e.g., axons of descending neurons).

(legend continued on next page)

Table 1. Dimorphism summary

		Male CNS		Female (FAFB/FlyWire)	
Region	Unit	dimorphic	specific	dimorphic	specific
Whole dataset	neurons	948 (0.5%)	1,420 (0.8%)	813 (0.5%)	363 (0.2%)
	types	167 (1.4%)	312 (2.6%)	151 (1.7%)	71 (0.8%)
Central brain	neurons	494 (1.4%)	1,166 (3.4%)	489 (1.4%)	355 (1%)
	types	138 (1.9%)	259 (3.6%)	134 (1.8%)	69 (0.9%)
Optic lobes	neurons	372 (0.3%)	131 (0.1%)	281 (0.3%)	8 (0.01%)
	types	1 (0.1%)	4 (0.6%)	1 (0.1%)	2 (0.3%)
Sensory	neurons	6 (0.03%)	0	6 (0.03%)	0
	types	2 (0.5%)	0	2 (0.9%)	0
VNC	neurons	76 (0.3%)	123 (0.5%)	37 (*)	0 (*)
	types	26 (0.7%)	49 (1.3%)	14 (*)	0 (*)

VNC counts for FlyWire (asterisks) only include ascending neurons.

this cell type has many dimorphic and sex-specific connection partners (5.5% of inputs and 57% of outputs). But perhaps surprisingly, the dimorphic connections are not exclusively localized to the male-specific arbors (Figure S3P): AOTU008 outputs to DNp05 solely from its male-specific branches but uses its whole axon to connect with VES202m (Figure S3Q). We can rationalize this difference by noting that AOTU008 can only connect to the isomorphic dendrites of DNp05 some distance away by extending an extra axon, whereas the male-specific VES202m neuron is directly adjacent to AOTU008, so connections can involve the entire axon.

Where do sex-specific and dimorphic neurons make connections? We find their synaptic distribution is non-uniform with a strong preference for integrative, higher brain regions of the protocerebrum (Figure 3K; Video S2), consistent with the location of *fruitless*-expressing neurons.[56] We also observe weaker enrichment in the lobula and gnathal ganglion, which are closer to the sensory periphery (Figure S3J). This spatial distribution is very similar across sexes, but with exceptions, e.g., in the SMP and SIP, which are enriched in the female and male, respectively (Figures S3H and S3J).

These results suggest that dimorphism is concentrated in integrative neurons at intermediate locations in sensory-motor pathways. We quantified this by applying a probabilistic graph traversal model, which starts from sensory neurons and assigns a layer to every neuron in the connectome graph[67] (Figure 3L). Isomorphic neurons are distributed relatively evenly across 7 layers (mean layer 3.9). By contrast, sex-specific and dimorphic neurons occupied deeper layers (mean at layers 4.3 and 4.5, respectively). The sensory periphery (layers 1–3) contains fewer such neurons: just 2.5% of male-specific versus 18.5% of isomorphic neurons.

Genetic basis for dimorphism

In *Drosophila*, alternative splicing of two master regulator genes, *fruitless* (*fru*) and *doublesex* (*dsx*), shapes neuronal development to produce sex differences in morphology and connectivity.[20,68,69] We can now examine these gene expression patterns alongside brain-wide wiring differences. We co-registered light microscopy datasets of *fruitless*[56,70] or *doublesex*[28] expression with both the MaleCNS and FAFB/FlyWire connectome (Figure 3M). Neurons matching the expression patterns were marked as high/low confidence, and counts were validated against previous studies[28,56,63] (Figure S3K; see STAR Methods). We annotated 4,858 (2,804 high confidence) *fruitless* and 412 (331 high confidence) *doublesex*-expressing neurons in the male CNS (2.9% and 0.2% of neurons) (Figure S3L). 258 neurons co-expressed both transcription factors. Most (75%) *fruitless*/*doublesex* annotations are in the central brain (Figures S3M and S3N), where 10.6% of male neurons are annotated as *fru+*. This represents an upper boundary compared with a lower boundary of 5% when using only high-confidence annotations (Figure S3L).

(H) Dimorphic and sex-specific neuron counts broken down by region.
(I) Proportion of central brain neurons that are dimorphic/sex-specific. Scatterplots show the spatial distribution of the somata of dimorphic and sex-specific neurons.
(J) Left: example of hemilineage with sex-specific neurons highlighted in red. Right: male versus female neuron count per hemilineage. Discounting sex-specific neurons tends to align numbers. The labeled hemilineages collectively generate ~50% of all dimorphic/sex-specific neurons in the male.
(K) Spatial distribution of pre- (outputs) and postsynapses (inputs) of dimorphic/sex-specific neurons. Arrowheads highlight differences between sexes.
(L) Layer assignments relative to sensory inputs for all neurons in the male CNS split by dimorphism. Data points are colored by superclass. Upper half shows the kernel density estimate of the underlying distribution. Mean layers for antennal lobe projection neurons (ALPNs), Kenyon cells, and central complex neurons (CX) are shown as landmarks. Boxplots show the median (vertical line), mean (circle), 1st–3rd quartile (box), and 1.5 interquartile range.
(M) Light-microscopy (LM) image of a *fruitless* (*fru+*) clone (top row) and matching neurons found in the EM (middle row).[56] Arrowhead points at variable branches in female aSP-g clones.
(N) Fraction of neurons in the central brain labeled as *fruitless*- and *doublesex*-expressing (*dsx+*) based on LM-EM matches. Numbers indicate total *fru+* and *dsx+* cell counts.
See also Table 1 and Figure S3.

How well does *fruitless*/*doublesex* expression correlate with sexual dimorphism? 90.4% of male-specific neurons in the central brain were annotated as *fru+*/*dsx+*, compared with 60.3% of dimorphic neurons and just 7.4% of isomorphic neurons (Figure 3N). Conversely, 9.6% of male-specific and 39.7% of dimorphic neurons are *fru−*/*dsx−*. Some of this discrepancy likely results from incomplete gene expression data (see STAR Methods); however, other genetic factors or non-cell autonomous mechanisms may shape some dimorphisms.

We also provide *synonyms* cross-referencing over 900 cell types (e.g., aSP-g; see Kohl et al.[27]) to previous studies[10,20,21,23,25,27,28] (Figure S3O) to the connectome. However, over 100 novel dimorphic/sex-specific connectome cell types could not be matched to the literature.

Visual system

Male fruit flies use visual information to guide courtship: chasing, ipsilateral wing preference, and courtship success depend on effective visual signaling.[23,71–73] To investigate visual sexual dimorphism, we compared the anatomy and connectivity of cells between male[39] and female[74] optic lobes (Figures 4A, 4B, and S4B; male optic lobe annotations are detailed in Data S1).[39,75] Sex-specific and dimorphic neurons are rare: of 249 intrinsic types, only three (Cm26, Tm26, and Mi20) are sex-specific, and only one (TmY21) is dimorphic. Strikingly, of the 335 visual projection neuron (VPN) types, just one is male-specific: LoVP92 (Figures 4B and 4C).

LoVP92 cells connect extensively with male-specific and dimorphic types, which comprise 18% of their inputs and 43% of their outputs (Figure 4G). Their axons converge with the processes of many male-specific central brain interneurons (Figures 4D, top, and S4C). In addition, four sex-shared descending neuron types, each with large isomorphic dendrites innervating distinct territories, extend a dimorphic branch enriched in dimorphic and sex-specific partners precisely to this node (Figures 4D, bottom, and S4D). Therefore, this node surrounding LoVP92 axons may serve as a hotspot, where dimorphic cell types converge to participate in male-specific circuits (Figure 4E, top). Dimorphic hotspot neurons are major targets of isomorphic VPN axons, effectively converting these VPNs into functionally dimorphic types (Figure 4H). We anticipate numerous hotspots in other central brain regions characterized by a high density of dimorphic connections (Figures 3K and 4E, bottom).

The anatomy of the peripheral visual system is largely isomorphic, but visual information flows through VPNs to highly dimorphic circuits in the central brain. 19/335 VPN types direct >9% of their output to male-specific/dimorphic neurons (Figure 4G). For example, isomorphic LC10a neurons, critical for accurate courtship tracking,[31,73,77,78] target dimorphic AOTU008 neurons in both sexes,[28] but AOTU008 makes male-specific projections (Figure 3F) and commits 57% of its output to sex-specific and dimorphic partners.

Of 19 VPN types with strong connections to dimorphic partners, seven have distinctive, frontal-biased visual fields: LoVP92 and 6 isomorphic types are confined to the anterior lobula, which samples the frontal visual field (Figures 4F and S4I).[76] These VPNs have strong input from dimorphic TmY21 interneurons (Figure S4E). TmY21 also receives frontal inputs, including from edge-detecting Dm3 neurons[39,79] targeting its male-specific arbors (Figure S4F), and the Dm3→TmY21 connection is notably stronger in males (Figure S4H). Moreover, two of the three male-specific intrinsic types, Tm26 and Mi20, also have frontal visual fields (Cell Type Explorer: Tm26, Mi20). This organization (Figure S4G)—and its likely behavioral significance—is reinforced by LC10a observations: this type covers the entire visual field, but only a frontal subgroup (Ant LC10a) (Figures 4F and S4I) is required for precise midline steering during arousal.[78]

We propose that frontal-biased VPNs connect to strongly dimorphic central brain circuits, rerouting visual information to support sex-specific behaviors, including courtship, where males follow females, keeping them in their frontal field of view.[36,73,80,81] This specialized processing of frontal visual space is reminiscent both of the fovea and higher acuity eye regions[39,76] in flies and the male "love spot" of larger fly species,[82] where specialized photoreceptors[83] are tuned for visual target tracking during courtship.[84–86] While *Drosophila* males lack prominent external eye specializations, the frontal-biased VPNs may be analogous to neurons in other insects that sample the visual space imaged by the love spot.[87,88]

To link frontal-biased VPNs to dimorphic motor behaviors, we identified 11 downstream DN types, including DNa02 and aSP22, required for effective visual pursuit when aroused[78] and later steps of male courtship[89] (Figures 4H, S4J, and S4K). Besides these known courtship pathways, we found additional connections that could support steering toward flies of either sex: LoVP92 connects, via male-specific inhibitory interneuron VES200m, onto DNg13 (Figure 4I; Video S3), a general-purpose, coarse steering pathway.[90] We hypothesize that, when the female is directly ahead during courtship, LoVP92 inhibits DNg13, favoring fine midline tracking through other descending pathways.

In summary, we provide circuit-level evidence for a behaviorally relevant love spot in *Drosophila*: male flies detect fly-sized objects in their frontal visual field,[73] and this information traverses sexually dimorphic circuits to descending pathways, likely facilitating successful courtship pursuit.

Auditory system

Auditory cues are central to *Drosophila* courtship. Male flies vibrate their wings to produce species-specific songs that can be used to distinguish species identity and mate quality.[91–94] *D. melanogaster* males generate distinct pulse and sine songs, controlled through nested networks in the VNC wing neuropil.[57,95] Songs elicit sexually dimorphic responses: receptive females slow down and allow copulation.[60,93,94,96–98] Males become aroused with increased locomotion, persistent courtship displays, and intermale competition.[99–103]

Song detection begins with mechanosensory neurons of the antennal Johnston's organ (JO), which project a tonotopic map to the AMMC, the first brain auditory processing center (Figures 5A and S5B).[104,105] Low-frequency courtship song is detected by JO-B sensory neurons.[101,106] Despite segmentation issues (Figures S5A and S5C), we found no evidence that these sensory neurons are sexually dimorphic.[99,101,102,107,108] JO-B targets include auditory Projection Neuron 1 (aPN1), a *fru+* but

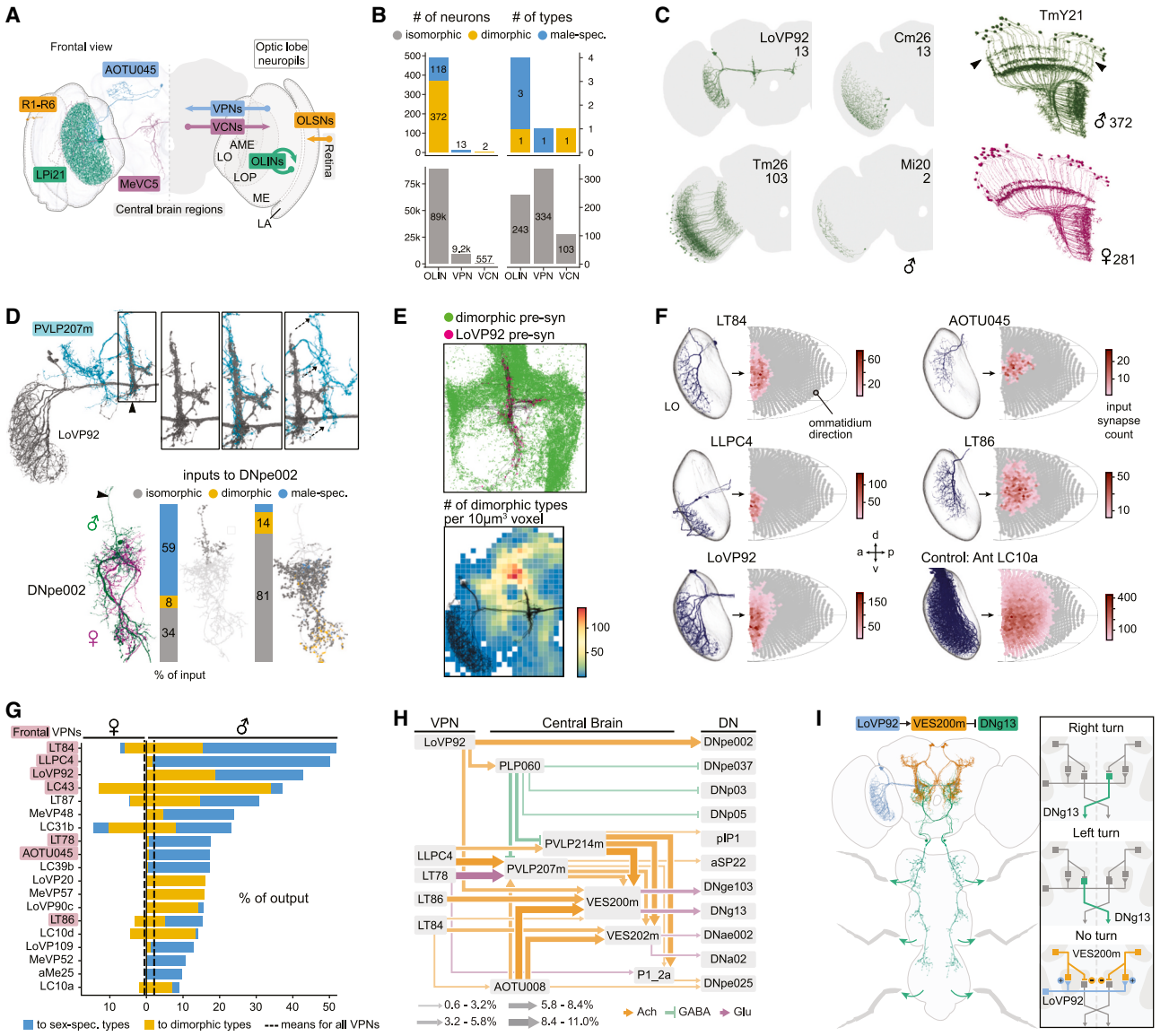


Figure 4. Sexual dimorphism in the visual system reveals a functional "love-spot"

(A) The optic lobe comprises five neuropils (LA, lamina; ME, medulla; LO, lobula; LOP, lobula plate; AME, accessory medulla) and four neuronal superclasses (OLSNs, optic lobe sensory neurons; OLINs, optic lobe intrinsic neurons; VPNs, visual projection neurons; VCNs, visual centrifugal neurons).

(B) Number of isomorphic, dimorphic, and male-specific neurons (left) and types (right) per superclass (outliers in Figure S4A).

(C) Male-specific and dimorphic types with total cell counts. Arrowheads indicate male-specific arborizations.

(D) Top: male-specific interneuron that converges onto LoVP92 axons (arrowhead). Inset: enlarged, shifted view. Bottom: dimorphic DN that extends a male-specific dendrite (arrowhead) toward LoVP92 axons. Stacked bar charts break down the synaptic input onto male-specific (left) versus isomorphic (right) DNpe002 arbors based on the dimorphism status of upstream partner neurons.

(E) Dimorphism around LoVP92 axons (black). Top: presynapses between dimorphic/sex-specific neurons (green). LoVP92 presynapses are shown in magenta. Bottom: density of dimorphic types per 10 μm^3 voxel.

(F) Morphology (left) and input synapse distribution mapped onto a Mollweide projection of the right compound eye's visual field[76] (right) of example frontal-biased VPNs.

(G) Output-normalized percentages of VPN outputs to dimorphic/sex-specific types in female (left) and male (right). Frontal-biased VPNs are highlighted in pink.

(H) Network diagram of male-specific connections between frontal VPNs and relevant DNs (see STAR Methods).

(I) 3D rendering of neurons in the frontal VPN to DN circuit (left). Simplified circuit diagram (right). VES200m links visual detection via LoVP92 to DNg13. Unilateral activation or inhibition of DNg13 causes ipsilateral or contralateral turning, respectively. LoVP92 activates VES200m bilaterally, and VES200m inhibits DNg13 ipsilaterally. LoVP92 activation therefore inhibits both DNg13 neurons, preventing turning.

See also Figure S4.

isomorphic population[99,101] (Figures 5B and S5D) essential for detecting courtship song, especially pulse.[101,108,109] To compare central auditory processing across sexes, we annotated 8 further song-responsive cell types described in the literature.[99,101,102,107,109–111]

Receptive females permit copulation by opening their vaginal plate through the action of vaginal plate opening descending neurons (vpoDNs) (DNp37). This is modulated by excitatory vaginal plate opening excitatory neurons (vpoENs) and inhibitory vaginal plate opening inhibitory neurons (vpoINs), two cell types both tuned to conspecific courtship song.[51] Despite this female-specific behavioral role, we identified vpoEN and vpoIN in the male CNS, surprisingly finding no clear morphological dimorphism (Figures 5C and S5F). However, their connectivity is necessarily very different: vpoDNs (and the vaginal plate) are absent in males. Approximately half of vpoEN outputs (but not inputs) are onto sex-specific/dimorphic cell types in both males and females. In males, vpoIN also has strong outputs onto sex-specific/dimorphic neurons, but female vpoINs primarily target isomorphic types (Figure 5C). Comparing vpoEN downstream partners between males and females, we find strong sex-shared (DNp55) and sex-specific downstream partners (vpoDN in females, pC1_6a in males) (Figures S5E and S5F). This last pair exemplifies a switchboard motif: male and female brains reroute the same sensory information via vpoEN to sex-specific downstream neurons.

In males, courtship song induces chaining, and functional analysis has begun to elucidate the circuit basis of this striking behavior where multiple males court each other. Chaining depends on aPN1 and male-specific *fru+* ventrolateral protocerebrum Projection Neuron 1 (vPN1) neurons,[99] which respond to pulse and sine songs and appear to excite male-specific pC1 neurons.[99] However, vPN1 is strongly predicted as GABAergic, so excitation cannot be direct (Figure S5G). Connectomic analysis likely resolves this by identifying a strong disinhibitory circuit: vPN1 inhibits a male-specific mAL, which inhibits pC1 (Figure S5G). This module may switch male behavior between aggression and courtship.

Downstream, we identified song DNs (pIP10[24] and pMP2[57]) (Figure 5D) and key wing pre-motor neurons in the VNC (TN1A, vPR9, and dPR1[57]) (Figure 5F). Extending previous work,[58,62] we also identified a set of male-specific ascending neurons—AN08B074 and AN08B084 (Figures 5D and S5I)—that feed information from VNC song generation neurons to *fru+* song detection circuits (e.g., aSP-a/pIP-e) in the central brain, as well as directly to song DNs (Figures 5E and 5F). These connections are actually bidirectional: song detection neurons also synapse onto the AN axonal arbors in the brain (Figures 5E, 5F, and S5H). This creates a closed loop in which the motor output of singing likely influences auditory detection of song (Figure 5G). This may form an efference copy circuit allowing males to distinguish their own song from that of others,[112] in turn influencing the male's arousal state.

Chemosensory systems

Flies use volatile and contact pheromones to signal sex and species identity, and these cues elicit sex-specific behavioral responses (Figures 6A and 6I).[113–117] We can now trace these signals from sensory neurons to their targets across the connectome to identify where sex differences arise.

Olfactory system

We first identified and cross-matched all 53 olfactory receptor neuron (ORN) and 8 thermo-/hygrosensory receptor neuron (TRN HRN) types, each projecting to a single antennal lobe (AL) glomerulus (Figures S6A and S6B; STAR Methods). Comparing male and female sensory neuron counts revealed a male bias in just 4/60 types: DA1, VA1v, VA1d, and VL2a (Figure 6B). This includes 3/3 *fru+* types and 3/4 glomeruli known to detect sex pheromones[113,118,119] (Figure 6C), as well as the food-responsive, pheromone-like VL2a.[120] The remaining sensory types had consistent counts between sexes.

Studies in moths linked male-enlarged glomeruli to pheromone processing via receptor neurons that are numerically enriched on the male antenna.[121] Low-resolution studies in *Drosophila* found volume differences[122] in 3/4 glomeruli highlighted above, but no differences in receptor neuron number.[123] Our examination of two brains precludes statistical analysis, but the targeted numerical differences in four biologically relevant glomeruli suggest a true sex difference. Increased sensory neuron numbers may allow males to sustain pheromone responses during courtship despite prolonged exposure over tens of minutes, analogous to the expansion of sensory neurons across drosophilid species to detect host plant volatiles.[124]

These count differences prompted us to look for male-female differences in AL connectivity. There was no clear evidence for differences in, e.g., proportion of sensory, local, and projection neuron connections owing to substantial technical differences across datasets (Figure S6C). This highlights the need for careful analysis of connectivity differences, particularly when interpreting global trends for a neuronal class as opposed to changes between specific cell types within the same class.

We next inspected antennal lobe projection and output neurons (187 types, collectively antennal lobe projection neurons [ALPNs]). While many ALPNs innervate a single olfactory glomerulus, the majority (60%) integrate information across multiple channels.[67] A threshold of 5% pheromone ORN input defined 136 pheromone ALPNs (27 types, including 21 multiglomerular), many of which remain functionally uncharacterized (Figure 6D). Just 2/187 types are sexually dimorphic. One multiglomerular PN, MZ_lv2PN, receives pheromone input from DA1 and VL2a ORNs only in males[125] (Figures 6E and S6D). These two pheromone pathways are known to regulate male courtship behavior.[120,125]

Consistent with our observations in the visual and auditory systems, sexual dimorphism of first- and second-order neurons is extremely limited. Instead, isomorphic projection neurons target sex-specific/dimorphic third-order partners. 17/187 ALPN types send at least 10% of their output to sex-specific/dimorphic third-order neurons in the male (Figure 6F, left). 12/17 are multiglomerular types, and, strikingly, half are GABAergic vPNs, including the inhibitory VA1v vPN, which sends >50% of its output to sex-specific/dimorphic neurons. These connections are primarily in the anteroventral lateral horn (LH), consistent with previous studies of pheromone representation[126] (Figure 6F, right).

We predicted that pheromone PNs would have many dimorphic partners, and this is mostly the case (Figures 6G and 6H).

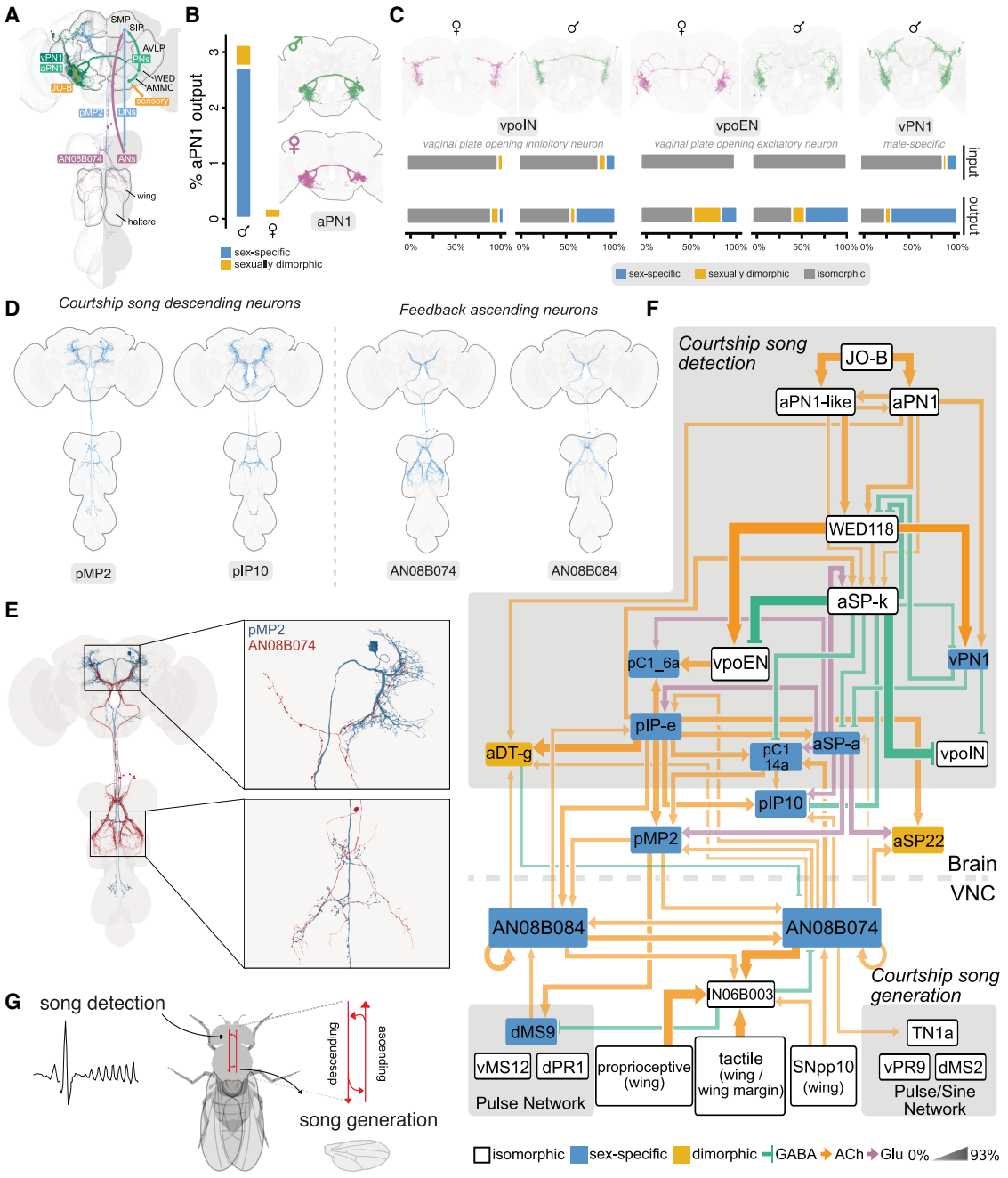


Figure 5. A recurrent feedback loop controls courtship song detection and action in the auditory system

(A) Overview of auditory pathway and recurrent feedback circuit. Song-induced vibrations move the arista to activate JO-B neurons, activating a sensorimotor loop that provides feedback from song-generating networks back to the central brain (SMP, superior medial protocerebrum; SIP, superior intermediate protocerebrum; AVLP, anterior ventrolateral protocerebrum; WED, wedge; AMMC, antennal mechanosensory and motor center).

(B) Proportion of aPN1 outputs to dimorphic (yellow) and sex-specific (blue) neurons in males (left) and females (right).

(C) Fraction of sex-specific/dimorphic inputs and outputs in females and males for vpoIN, vpoEN, and vPN1.

(D) Morphology of male-specific descending neurons (pMP2 and pIP10) that drive courtship song and male-specific ascending neurons (AN08B074 and AN08B084) that connect song generation circuits back to song detection in the central brain.

(E) Morphologies of a descending neuron that drives song (pMP2) and an ascending neuron downstream of song production circuits (AN08B074).

(F) Connectivity between central brain song detection and VNC song production circuits: the established pulse and sine song network in the wing neuropil is reproduced and connected to identified DNs and to male-specific ANs that project back to central brain nodes. Line widths denote input-normalized connection strengths. Scale bars as indicated.

(G) Schematic of reciprocal influence between song detection and generation.

See also Figure S5.

However, pheromone-responsive DA1 lPNs, DL3 lPNs, and VA1v adPNs have a low fraction of sex-specific/dimorphic partners. Unlike most multiglomerular PNs, these uniglomerular PNs also target the mushroom body, the principal site of learning and memory,[127–129] in addition to the LH. We see no obvious sex differences in pheromone PN outputs in the mushroom body (Figure S6E), but there are notable changes in dopaminergic punishment and reward signals (V.S. and M.W.P., unpublished data).

Gustatory system

Gustatory receptor neurons (GRNs) fall into six anatomically distinct subclasses primarily based on their precise location on the mouth parts, legs, and wings[130] (Figures 6J and S6F). A detailed typing and cross-matching of all gustatory sensory neurons is reported in our companion paper.[131] Combining this with identification and analysis of proboscis motor neurons reveals how sensory input is transformed into the motor programs underlying feeding and foraging behavior.[132]

Some foreleg gustatory sensory neurons have dimorphic axon projections,[133] but we otherwise see minimal dimorphism at this first layer.[131] However, there are clear sex differences in downstream circuit organization, with substantial dimorphism arising at the second order, earlier than in other sensory systems. Local leg bristles engaged most strongly with dimorphic circuits (11% of outputs in males). Wing bristles also had a high fraction (6%), but ascending leg, pharyngeal, and labellar sensory neurons were all much lower (~1%) (Figure 6K). Early gustatory processing is therefore more dimorphic in the VNC than the brain. The more limited dimorphic connectivity in the brain is concentrated in a subset of GRN types (12/43 types in males) (Figure 6L). This suggests a clear anatomical division: information entering via a larger number of gustatory information channels associated with the mouth parts directs general sex-shared behaviors like feeding, while a more specific set of receptors in the rest of the body focuses on sex-relevant cues.

We next compared the anatomy of sex-specific/dimorphic versus isomorphic second-order gustatory neurons in the male CNS (Figure 6M). Isomorphic downstream partners of mouthpart sensory neurons are confined to primary taste processing areas in the gnathal ganglion (GNG). By contrast, dimorphic partners immediately project widely across the central brain and VNC (Figures 6M and S6G), including to higher brain areas characterized by many dimorphic connections (Figures 3K and 4E). Dimorphic partners of nerve cord GRNs target these same brain areas and show some specificity for foreleg neuropils (likely associated with male tapping). Neuroanatomical comparison of dimorphic and isomorphic second-order gustatory neurons in females showed similar trends and included some female-specific taste projection neurons (Figure S6H).

Global analysis of sexually dimorphic connectivity

In Figure 3, we identified isomorphic, dimorphic, and sex-specific neurons principally through morphological analysis before examining how some of these neurons are wired into specific circuits (Figures 4, 5, and 6) to propose general principles of dimorphic circuit organization. How do these dimorphic elements translate into male-female wiring differences? To address this question, we represented male and female brain connectomes as a pair of weighted graphs, the union of which contains 8,302 nodes representing cell types (cross-matched or sex-specific) and 3.76 M weighted connections (edges) between them. The dimorphism labels of the pre- and postsynaptic cell types define a set of expectations (see Figure 7A for male and Figure S7A for female):

- Most connections (3.4M or 89.9%) are between two isomorphic types, and we expect these to be isomorphic.
- 242k (6.4%) connections involve a sex-specific type and therefore can exist only in one sex.
- 137k (3.7%) connections involve dimorphic types at one or both ends. We expect these to be a mix of isomorphic and dimorphic connections.

A connectivity-based approach to find dimorphic edges

Connectivity varies between individuals of the same sex due to both genuine biological variability and technical noise (imaging, segmentation, proofreading, and annotation).[30] To account for these factors, we combined two filters: a noise threshold and a t-statistic. Since the distribution of edge weights is highly skewed and the majority of connections are weak and unreliable,[30] we defined a threshold for each dataset to separate signal from noise by labeling weak edges (<11 synapses for male CNS, <8 for FAFB/FlyWire) (Figure S7E; see STAR Methods for details) as noisy. While this removes 80% of connections, most synapses (~90%) belong to strong connections that are reliably observed within and across datasets. We then developed a simple statistical approach to highlight connections that are significantly different between male and female while accounting for biological/technical variability.

For example, despite their name, the two *fru+* excitatory vaginal plate-opening neurons (vpoENs) show no significant morphological male-female differences (Figure 7B), but they do make many synaptic connections to/from sex-specific (7.6% in females; 21% in males) and dimorphic (16% in females; 7.4% in males) cell types such as female-specific AVLP569. This connection is, by definition, dimorphic (Figure 7C). Less clear is vpoEN's connection onto dimorphic cell type aSP10C_a: with 420 synapses in males and only 237 in females, this connection is a strong candidate for dimorphic connectivity. Applying our statistical analysis, we first break the connection into male and female left/right (Figure 7D). Because synapse counts differ systematically across datasets (mostly for technical reasons[30]), we scaled male connection strengths down to match the female (Figure S7D; see STAR Methods). We computed a t-statistic where the mean difference between male and female edge weights is divided by the within-sex (left versus right) standard deviation. Intuitively, this highlights connections with large differences between datasets and low variability across hemispheres of the same dataset (Figure 7D). Given the large number of tests, we used false discovery rate (FDR) correction[134] to balance sensitivity and specificity (see STAR Methods). Finally, we required at least a 30% difference between (scaled) male and female weights (see Figure 7E for the full decision tree). Based on this approach, the connection between vpoEN and aSP10C_a is not significantly different between sexes ($p = 0.55$): raw synapse counts must be compared with caution.

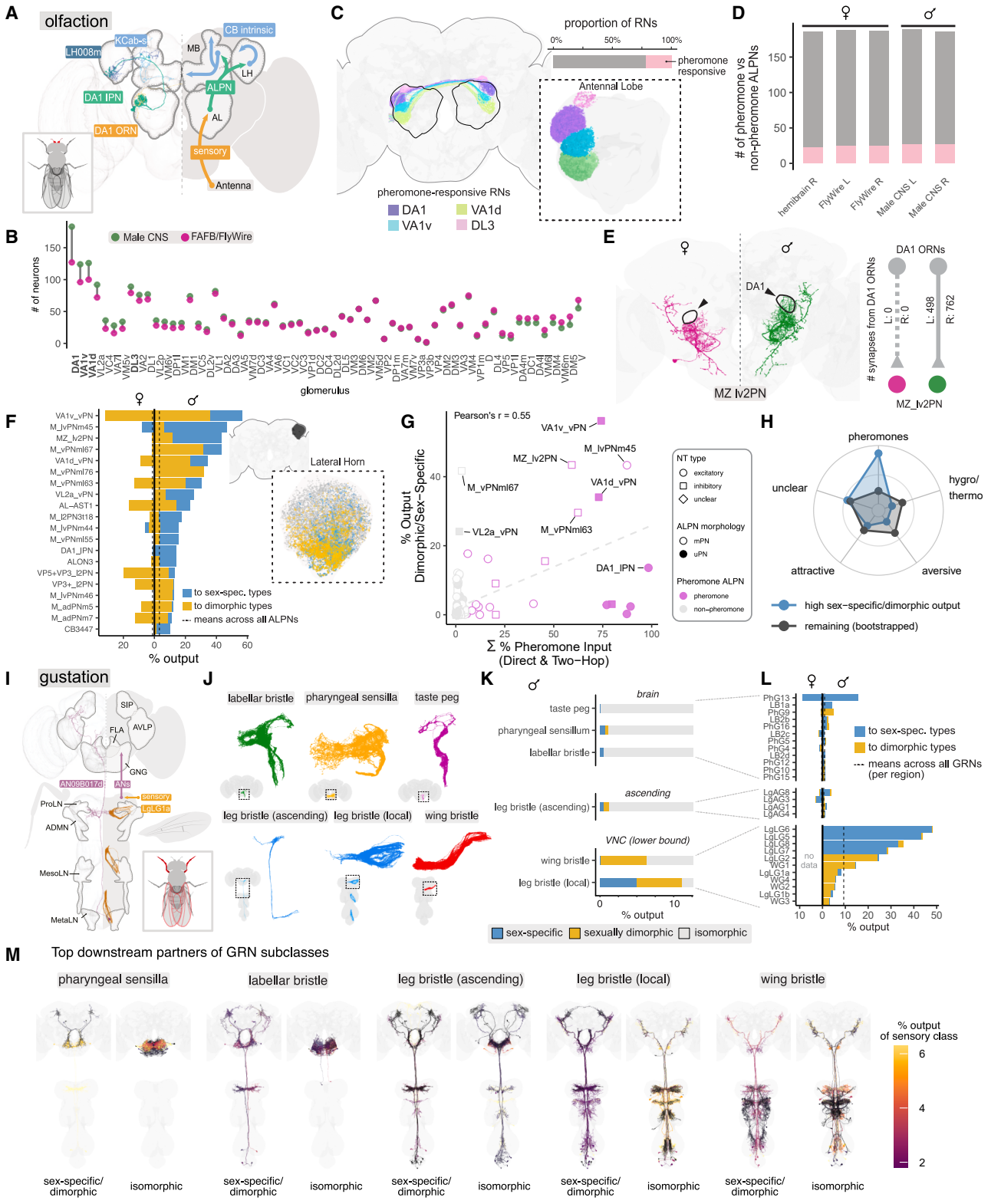


Figure 6. Dimorphism in chemosensory systems

(A) Information flow from antennal lobe (AL) sensory neurons to the lateral horn (LH) and mushroom body (MB, CB intrinsic) via AL projection neurons (ALPN). Left: example neurons. Right: information flow schematic. Inset: Antennae highlighted in red.

(legend continued on next page)

Around half of vpoEN output connections are dimorphic (48% in males; 28% in females), but fewer than 1% of inputs are dimorphic (Figure 7F). This illustrates a general theme of "secondary" dimorphism where otherwise isomorphic cell types have substantial dimorphic connectivity. We applied this pipeline (Figure 7E) across the central brain, labeling each edge as dimorphic, isomorphic, or noisy (Figure 7G). We found that 11% of all isomorphic cell types in the male (3.2% in females) have more than 5% dimorphic in- or outputs (Figure 7H). This equates to 6.9% of all neurons (1.9% in females), so secondary dimorphism is fairly common (Figures 7H and S7I). *fru*/*dsx*-expressing neurons are more likely to participate in dimorphic connections, in line with these transcription factors regulating guidance molecules that make neurites extend to new regions, presumably enabling sex-specific connections.[133,135] This bias is conserved among isomorphic *fru*/*dsx* neurons. We suggest that sex-specific expression of target-recognition factors in neurons without morphological sex differences is another mechanism generating dimorphic connectivity.

Ignoring noisy edges, 5.8% of connections in the male central brain (and 1.2% in the female) are dimorphic, with similar numbers for synapses (Figures 7I and 7J). There are therefore slightly more dimorphic connections than sex-specific/dimorphic neurons in males, but the opposite is true in females (compare to Figure 3I). Identifying all dimorphic edges enables many additional analyses: for example, the highly punctate spatial distribution of the contributing synapses (Figure 7K) reinforces our earlier observations about dimorphic hotspots (e.g., Figure 3K).

Dimorphic neurons are strongly clustered and interconnected

Having defined both dimorphic cell types and connections, we investigated network-level features of dimorphism in the central brain. Communities of cell types were identified by similar connectivity to other cell types (Figures 7L and 7M; STAR Methods), revealing two key modes of involvement of the dimorphic and male-specific types in the network structure.

Firstly, the majority of dimorphic or male-specific types formed few communities, constituting distinct male-specific subnetworks (Figure 7N). Remaining male-specific/dimorphic types are sparsely distributed and integrated into the isomorphic subgraph. Second, the male-enriched communities are densely interconnected with other enriched communities. For example, the most enriched community (labeled 102) (Figure 7P) principally contains many pC1 subtypes (Figure 7O; see Rubin et al.[136]). Finally, the proportion of *fru+*/*dsx+* neurons is much higher in enriched versus non-enriched communities (Figure 7Q), paralleling recent observations in females[137] and confirming the long-standing hypothesis that *fruitless* neurons preferentially connect with each other to form circuits regulating male behavior.[122]

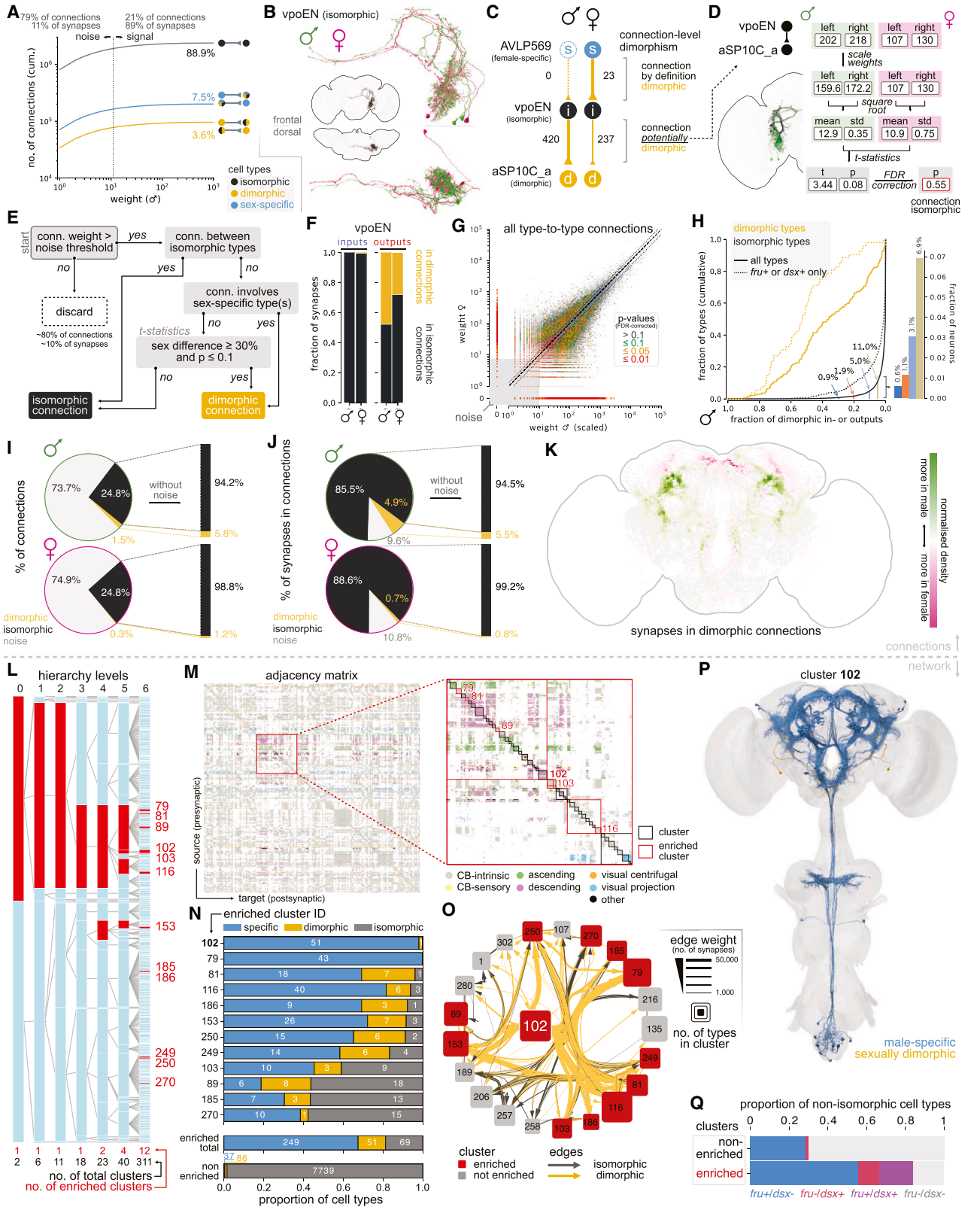
DISCUSSION

The complete and fully proofread male central nervous connectome represents a major advance in linking neural circuits and behavior, enabling end-to-end analysis from eyes to legs. Rich annotations link over 95% of neurons to previously reported cell types and functional analysis.

The number of sex-specific and dimorphic neurons is relatively modest (approximately 5% of the male brain and 2% of the female brain) (Figure 3I), but they can have major impacts on function. One explanation is that an additional 6.9% of male central brain neurons (1.9% for females) participate in dimorphic connections (secondarily dimorphic) (Figure 7H). At the cellular level, perhaps surprisingly, we find male-specific neurons to be more common than dimorphic neurons, whereas the opposite is true in females. A greater proportion of male-specific versus female-specific neurons is also observed in *C. elegans*, although the difference is more extreme (23.6% versus 2.6%).[138] This consistent bias may reflect selection pressure on male behaviors.

Sexually dimorphic elements are concentrated in higher brain areas (Figure 3K). This is compatible with the pattern of *fruitless*-expressing neurons in the brain[122,139] and volumetric differences between male and female brains.[56] However, we can now place these neurons in circuits: they are in deep layers of the connectome between the sensory and motor periphery (Figure 3L). This

(B) RN counts per type in male (green) and female (magenta) sorted by male-female difference.
(C) Pheromone-responsive ORNs: DA1, DL3, VA1d, VA1v. 10 neurons shown per type. Right: proportion of pheromone ORNs among all RNs (O/T/HRN). Inset: presynapses from pheromone ORNs.
(D) Number of pheromone and non-pheromone ALPNs per hemisphere.
(E) One of two sexually dimorphic ALPNs, MZ_lv2PN, in males and females. Right: synapse counts from DA1 ORNs onto MZ_lv2PN.
(F) Left: ALPN percentage outputs to dimorphic (yellow) and sex-specific (blue) neurons in males or females. Right: LH postsynapses for ALPN types shown in the plot, colored by dimorphism status.
(G) Correlation between the percentage of pheromone input for ALPNs (direct and two-hop) versus the percentage output to dimorphic/sex-specific neurons.
(H) Bootstrapped comparisons of sex-specific/dimorphic targeting across ALPN groups defined by dominant RN input valence.
(I) Schematic of the taste sensory pathway (SIP, superior intermediate protocerebrum; AVLP, anterior ventrolateral protocerebrum; FLA, flange; GNG, gnathal ganglia; ProLN, prothoracic leg neuropil; ADMN, anterior dorsal metathoracic nerve; MesoLN, mesothoracic leg neuropil; MetaLN, metathoracic leg neuropil). Inset: Location of gustatory receptor neurons highlighted in red; mouth parts not shown.
(J) Taste peg, labellar bristle, and pharyngeal sensilla GRNs (top) enter via nerves targeting the brain. Leg and wing bristle GRNs (bottom) enter via the VNC.
(K) Proportion (%) of GRN output to types annotated as sex-specific (blue) or sexually dimorphic (yellow) according to subclass/anatomical location: brain (top), ascending (middle), VNC (bottom).
(L) For each subclass, the main GRN cell types targeting sex-specific and sexually dimorphic neurons (>1% in either sex) in females (left) and males (right). See Figure S6F for included subclasses.
(M) Visualization of top sex-specific and sexually dimorphic (left) versus isomorphic (right) downstream partner cell types for taste sensory subclasses, colored by percent output from each subclass (see STAR Methods for cell types and details). Sex-specific and sexually dimorphic neurons extend distinct projections to AVLP, SMP, SLP, SIP, FLA, and LegNpT1 (see Figure S6G).
See also Figure S6.



(legend on next page)

suggests a hierarchy in which sex differences primarily modify integrative and decision-making areas while sensory detection and the highly tuned motor interface remain more constant. This logic appears distinct from *C. elegans*, where male-specific neurons are scarce in the nerve ring.[138] It will be very interesting to see which of these patterns apply to circuit evolution across species.[140]

Even within higher brain centers, there is additional structure: dimorphic cell types have spatially clustered synapses (Figure 3K) associated with feedforward and feedback connections in particular sensorimotor pathways such as vision (Figure 4E) or ascending taste neurons (Figure 6M). Downstream of sex-shared VPNs, we see wiring motifs including sign inversion by male-specific inhibitory interneurons (e.g., VES200m) (Figure 4H) and new feed-forward excitation pathways (e.g., PVLP207m) (Figure 4H). By contrast, some sex-shared interneurons are nodes for dimorphic connectivity without showing any sign of dimorphic morphology (vpoENs in Figures 5C, 7B, and 7F). Zooming out, while some dimorphic neurons integrate more sparsely across the connectome, the dominant organizational principle seems to be tightly coupled sex-specific hubs (Figure 7). It may be easier to evolve such discrete modules to produce major changes in sex-specific behavior, consistent with our observations that most sex-specific and dimorphic neurons originate from a small number of neuroblast lineages (Figures 3J and S3I).

We see a strong correspondence between *fru*/*dsx* expression and dimorphic and male-specific neurons, albeit with potentially interesting discrepancies. *fru*/*dsx* are expressed in over 2,000 positive neurons that are not dimorphic in the connectome. Technical limitations likely play a role, but they may be regulating features other than wiring. For example, we can confidently identify cell type LHPV6q1 (pSP-e, FMRFa-WED). It has documented sex differences in electrophysiological properties, including spontaneous firing rate,[50] but shows no wiring differences in the connectome. Conversely, many dimorphic or sex-specific neurons in the connectome appear not to express *fru*/*dsx*. This includes high-confidence cases (e.g., ~200 neurons in the central brain with known lineage), raising the possibility of alternative sex differentiation mechanisms.

Connectomics is in a rapid growth phase, but low sample numbers still pose significant challenges for comparative connectomics. Lessons learned during this project leave us cautious in some areas but optimistic overall. We believe that attempts to extract biological differences from direct comparison of two raw connectome graphs are unlikely to be successful. Rather, we recommend analyzing cell type graphs, capturing the fundamental unit of conservation across connectomes while accounting for interindividual variation.[30] A strong quantitative understanding of that variability (and its technical and biological origins) is also essential. Crucially, considering bilateral consistency of cell type morphology and wiring enabled us to draw robust conclusions about the identity of dimorphic elements. A specific example may be instructive. We previously noted a unique VPN (LoVP109/LTe12) present once in each optic lobe of the FAFB/FlyWire female brain[29,30] was missing in the single male optic lobe of Nern et al.[39] However, we now find this cell in the second optic lobe of the complete male CNS, suggesting a developmental error in one optic lobe. We estimate this error rate at <1% for neurons in each hemisphere.[30] If errors occur independently in the two hemispheres—as observed here—then the chance of missing an entire cell type is <0.01%, or about 3 pairs of neurons in the central brain. This is a very low false positive rate compared with our observation of >1,000 male-specific neurons. Similar principles apply for connectivity, echoing recent work on cross-species comparisons of the larval *Drosophila*

Figure 7. Sexual dimorphism in central brain connectivity and networks

(A) Distribution of male type-to-type connection weights broken down by dimorphism of pre- and postsynaptic cell type. Dotted vertical line indicates the noise threshold. See Figure S7 for female data.

(B) Example of an isomorphic cell type (vpoEN) with a large fraction of dimorphic outputs (by synapse count) in both males and females.

(C) Illustration of neuron-level dimorphism and expected resulting edge dimorphisms.

(D) t-statistic to find significant differences in male-female connectivity. The denominator is a pooled standard deviation combining the standard deviations for male and female edge weights (see STAR Methods).

(E) Decision tree to determine the dimorphism status of a connection.

(F) Proportion of vpoEN pre- (outputs) and post- (inputs) synapses in dimorphic versus isomorphic connections in males and females.

(G) Male (scaled) versus female type-to-type central brain edge weights colored by FDR-corrected *p* value. Dotted envelope demarcates a 30% difference in connection weights.

(H) Cumulative fraction of iso- and dimorphic cell types (*y* axis) with more than a given fraction in- or outputs (*x* axis, by synapse count) in males. Arrows indicate fractions at various thresholds. For example, 0.9% of isomorphic types have >=30% dimorphic inputs and outputs. Bar chart (right) translates thresholds into a fraction of neurons.

(I) Proportion of edge types by total number in males (top) and females (bottom). Bar plots (right) show the fraction of dimorphic edges/synapses after discounting noisy connections.

(J) Same as (I) for synapses.

(K) Male-female differences in spatial distribution of synapses in dimorphic edges.

(L) Hierarchical community detection partitions the cell types of the male central brain into blocks of similar connectivity. IDs of male-enriched clusters are shown in red.

(M) Type-to-type adjacency matrix sorted by hierarchical clustering (L) reveals highly structured connectivity. Rows (sources) are colored by their superclass.

(N) Breakdown of cell type identity in the 12 enriched clusters at level 6.

(O) Network graph of the neighborhood around enriched cluster 102. It includes many other enriched clusters, highlighting concentration into highly interconnected modules. Only connections of ≥1,000 synapses are shown.

(P) Rendering of enriched cluster 102, the most statistically overrepresented for male-specific or dimorphic cell types, such as male-specific pC1 (P1) and mALs.

(Q) *Fruitless* and *doublesex* expression among non-isomorphic cell types in enriched versus non-enriched clusters.

See also Figure S7.

olfactory system.[141] Nevertheless, expert curation was still essential to separate biological signal from technical noise (which is more commonly correlated across both sides of one brain).

Limitations of the study

Our dataset includes the entire male CNS, but we could only make comprehensive across-sex comparisons to the female brain.[29,30,43] Comparisons to the partially proofread female nerve cord (FANC) dataset[32,142] were necessarily more restricted. The new female brain and nerve cord (BANC)[143] dataset should allow male-female comparisons in the future, but at the time of writing, further proofreading, careful joint cell typing, and a quantitative understanding of variation will be essential to draw robust conclusions about sex differences.

The connectome provides the structural wiring diagram, but functional analysis is required to confirm predictions about differences in information flow and their impact on behavior. We are heartened by the recent success of brain-scale simulation studies.[144,145] In the future, *in silico* manipulation of neuronal connectivity and activity may help understand the impact of dimorphic elements and prioritize the many experimental hypotheses emerging from connectomics.

We have likely failed to identify some developmentally homologous neurons because their structure and connections are too divergent. Integration with molecular and developmental studies may be essential to resolve these issues.[146–148] However, providing the most detailed picture yet of the end state of sexually dimorphic development should prove invaluable for studies examining the molecular specification of brain wiring.[149]

Similarly, this connectome represents a snapshot in the lifetime of an animal. This study confirmed our previous observations that the core wiring diagram is stable.[30] However, even strongly innate dimorphic behaviors can be modified by experience.[150,151] Building on developments in comparative connectomics—including this study—opens exciting opportunities to learn about the footprint that experience leaves in the wiring diagram of the brain.

RESOURCE AVAILABILITY

Lead contact

Further information and requests should be directed to and will be fulfilled by the lead contact Gregory Jefferis (jefferis@mrc-lmb.cam.ac.uk).

Materials availability

This study did not generate any new, unique reagents.

Data and code availability

Primary data artifacts can be downloaded from a Google bucket, gs://flyem-male-cns, with further download and interactive web tools at https://male-cns.janelia.org. Derived data products specific to this paper are available at https://github.com/flyconnectome/2025malecns. Updated annotations for FAFB-FlyWire are at https://github.com/flyconnectome/flywire_annotations.

ACKNOWLEDGMENTS

This work was principally funded by Wellcome Trust collaborative awards (220343/Z/20/Z and 221300/Z/20/Z) to G.S.X.E.J., G.M.R., S.W., and G.C.; by the Howard Hughes Medical Institute at Janelia for the FlyEM project team led by S.B. for proofreading, annotation, and analysis of male CNS neurons; and by core funding from the Medical Research Council (MC_U105188491) to G.S.X.E.J. Collaboration was supported in part by the Janelia Visiting Scientist Program. I.R.B. was supported by Boehringer Ingelheim Fonds and the Cambridge Commonwealth, European and International Trust. Development of the natverse has been supported by the NIH Brain Initiative (1RF1MH120679-01) and NSF/MRC Neuronex2 (NSF 2014862/MC_EX_MR/T046279/1). We thank Sven Dorkenwald and Arie Matsliah for sharing data artifacts for new synapse predictions for FAFB/FlyWire[152] and the MRC LMB Scientific Computing group for assistance with compute and web infrastructure. We thank Hiroshi Shiozaki and Davi Bock for their comments. For the purpose of open access, the MRC Laboratory of Molecular Biology has applied a CC BY public copyright license to any author-accepted manuscript version arising. This article is subject to HHMI's Open Access to Publications policy. The HHMI lab heads have previously granted a nonexclusive CC BY 4.0 license to the public and a sublicensable license to HHMI in their research articles. Pursuant to those licenses, the author-accepted manuscript of this article can be made freely available under a CC BY 4.0 license immediately upon publication.

AUTHOR CONTRIBUTIONS

K.J.H. and Z.L. prepared the sample. W.Q., A.C., C.S.X., and H.F.H. imaged the sample. S.P., E.T.T., T. Pietzsch, and S.S. aligned the electron microscopy (EM) data. S.B., M.J., and C.O. produced the automated segmentation. I.R.B., M. Costa, E.C.M., S.-y.T., A.M.C.F., M. Cook, M.G., C.O., T. Paterson, F. Li, B.J.M., I.A., P.B., B.S.C., I.d.H.V., C.R.D., S.F.M., M.A.F., I.H., G.P.H., L.K., J.K., S.A.L., M.L., A.L., C.A.M., I.M., C.M., E.M., N.O., A.P., B.P., E.M.P., A.R., J.R.S., R.J.V.R., A.L.S., L.A.S., L.S.C., C.S., S.T., A.T., J.J.W., H.W., E.A.Y., and T.Y. proofread the segmentation. G.B.H. and C.O. produced the automated synapse detections. S.B., A.N., D.A., G.B.H., and A.S.B. identified neurotransmitters. P. Schlegel, A.N., J.B., and S.C. developed spatial transforms. I.R.B., M. Costa, P. Schlegel, E.C.M., A.N., S.-y.T., A.M.C.F., M.G., T.S., C.R.W., F. Li, B.J.M., M.W.P., V.S., G.B., R.J.B., P.B., B.C., I.d.H.V., G.D., E.D., M.D.S., C.R.D., K.E., L.K., I.M., E.M., A.P., A.R., I.T., H.W., C.R., and G.S.X.E.J. typed and annotated cells. S.B., I.R.B., M. Costa, P. Schlegel, E.C.M., A.N., S.-y.T., A.M.C.F., M. Cook, M.G., C.O., T. Paterson, T.S., K.D.L., C.M., C.K., and G.S.X.E.J. provided quality control. S.B., P. Schlegel, S.P., W.T.K., E.T.T., L.E.B., J.H., F. Loesche, J.C., P.M.H., D.J.O., R.S., L.U., A.Z., S.S., and G.S.X.E.J. developed software tools. S.B., I.R.B., P. Schlegel, A.M.C.F., L.E.B., F. Loesche, P.M.H., and E.M.R. developed visualizations and presentation tools. I.R.B., M. Costa, P. Schlegel, A.S.C., and G.S.X.E.J. drafted the main text with input from S.B., A.N., A.M.C.F., S.S.M., C.R., M.B.R., and G.M.R. S.B., M. Costa, P. Schlegel, M.J., A.N., S.P., D.A., G.B.H., J.H., and M.B.R. wrote the methods. S.B., I.R.B., M. Costa, P. Schlegel, A.N., A.M.C.F., A.S.C., M.G., G.B.H., F.K., T.S., C.R.W., V.S., Y.Y., M.D., S.S.M., E.M.R., P. Seenivasan, A.Z., M.B.R., and G.S.X.E.J. analyzed the connectome and designed figures. M. Costa, P. Schlegel, E.C.M., G.W.M., S.R., S.S., M.B.R., and G.S.X.E.J. provided supervision. V. Jain, W.K., S.W., G.M.C., G.M.R., and G.S.X.E.J. acquired funding. S.B., S.P., S.M.P., R.G., V. Jayaraman, W.K., J.F., L.K.S., G.M.C., H.F.H., G.M.R., and G.S.X.E.J. guided the project.

DECLARATION OF INTERESTS

L.S.C. declares a financial interest in Aelysia Ltd.

STAR★METHODS

Detailed methods are provided in the online version of this paper and include the following:

- KEY RESOURCES TABLE
- EXPERIMENTAL MODEL AND STUDY PARTICIPANT DETAILS
- METHOD DETAILS
  - EM Sample Preparation
  - Hot-knife cutting
  - EM Volume Imaging
  - EM Volume Alignment

- EM Volume Segmentation
- EM Volume Synapse Identification
- Neurotransmitter prediction
- EM Volume Proofreading
- Spatial Transforms
- Defining anatomical regions in the EM volume
- Analysis Software
- Annotations
- Connectivity co-clustering
- Morphological co-clustering
- Inspection of clusterings
- Sensorimotor information flow analysis
- Sensorimotor clusters
- Effective connectivity
- Edge normalization
- Definition of dimorphic edges

- GRAPH TRAVERSAL
- OLFACTORY SYSTEM ANALYSIS
  - Gustatory system analysis
  - Network analyses
  - Optic lobe analysis
  - Sex-specific branch analysis
- QUANTIFICATION AND STATISTICAL ANALYSIS
- ADDITIONAL RESOURCES

SUPPLEMENTAL INFORMATION

Supplemental information can be found online at https://doi.org/10.1016/j.cell.2026.08.015.

Received: October 29, 2025
Revised: June 4, 2026
Accepted: August 7, 2026
Published: September 3, 2026

REFERENCES

1. Chen, P.B., Hu, R.K., Wu, Y.E., Pan, L., Huang, S., Micevych, P.E., and Hong, W. (2019). Sexually dimorphic control of parenting behavior by the medial amygdala. Cell *176*, 1206–1221.e18. https://doi.org/10.1016/j.cell.2019.01.024.
2. Beach, F.A. (1940). Effects of cortical lesions upon the copulatory behavior of male rats. J. Comp. Psychol. *29*, 193–245. https://doi.org/10.1037/h0058820.
3. Goy, R.W., and Phoenix, C.H. (1963). Hypothalamic regulation of female sexual behaviour; establishment of behavioural oestrus in spayed guinea-pigs following hypothalamic lesions. J. Reprod. Fertil. *5*, 23–40. https://doi.org/10.1530/jrf.0.0050023.
4. Lin, D., Boyle, M.P., Dollar, P., Lee, H., Lein, E.S., Perona, P., and Anderson, D.J. (2011). Functional identification of an aggression locus in the mouse hypothalamus. Nature *470*, 221–226. https://doi.org/10.1038/nature09736.
5. Remedios, R., Kennedy, A., Zelikowsky, M., Grewe, B.F., Schnitzer, M.J., and Anderson, D.J. (2017). Social behaviour shapes hypothalamic neural ensemble representations of conspecific sex. Nature *550*, 388–392. https://doi.org/10.1038/nature23885.
6. Bergan, J.F., Ben-Shaul, Y., and Dulac, C. (2014). Sex-specific processing of social cues in the medial amygdala. eLife *3*, e02743. https://doi.org/10.7554/eLife.02743.
7. Ishii, K.K., Osakada, T., Mori, H., Miyasaka, N., Yoshihara, Y., Miyamichi, K., and Touhara, K. (2017). A labeled-line neural circuit for pheromone-mediated sexual behaviors in mice. Neuron *95*, 123–137.e8. https://doi.org/10.1016/j.neuron.2017.05.038.
8. Wu, Z., Autry, A.E., Bergan, J.F., Watabe-Uchida, M., and Dulac, C.G. (2014). Galanin neurons in the medial preoptic area govern parental behaviour. Nature *509*, 325–330. https://doi.org/10.1038/nature13307.
9. Ryner, L.C., and Baker, B.S. (1991). Regulation of doublesex pre-mRNA processing occurs by 3′-splice site activation. Genes Dev. *5*, 2071–2085. https://doi.org/10.1101/gad.5.11.2071.
10. Ryner, L.C., Goodwin, S.F., Castrillon, D.H., Anand, A., Villella, A., Baker, B.S., Hall, J.C., Taylor, B.J., and Wasserman, S.A. (1996). Control of male sexual behavior and sexual orientation in Drosophila by the fruitless gene. Cell *87*, 1079–1089. https://doi.org/10.1016/s0092-8674(00)81802-4.
11. Inoue, K., Hoshijima, K., Higuchi, I., Sakamoto, H., and Shimura, Y. (1992). Binding of the Drosophila transformer and transformer-2 proteins to the regulatory elements of doublesex primary transcript for sex-specific RNA processing. Proc. Natl. Acad. Sci. USA *89*, 8092–8096. https://doi.org/10.1073/pnas.89.17.8092.
12. Felsenberg, J., Barnstedt, O., Cognigni, P., Lin, S., and Waddell, S. (2017). Re-evaluation of learned information in Drosophila. Nature *544*, 240–244. https://doi.org/10.1038/nature21716.
13. Griffith, L.C., and Ejima, A. (2009). Courtship learning in Drosophila melanogaster: diverse plasticity of a reproductive behavior. Learn. Mem. *16*, 743–750. https://doi.org/10.1101/lm.956309.
14. Meissner, G.W., Vannan, A., Jeter, J., Close, K., DePasquale, G.M., Dorman, Z., Forster, K., Beringer, J.A., Gibney, T., Hausenfluck, J.H., et al. (2025). A split-GAL4 driver line resource for Drosophila neuron types. eLife *13*, RP98405. https://doi.org/10.7554/eLife.98405.
15. Tirian, L., and Dickson, B.J. (2017). The VT GAL4, LexA, and split-GAL4 driver line collections for targeted expression in the Drosophila nervous system. Preprint at bioRxiv, 198648. https://doi.org/10.1101/198648.
16. Jenett, A., Rubin, G.M., Ngo, T.-T.B., Shepherd, D., Murphy, C., Dionne, H., Pfeiffer, B.D., Cavallaro, A., Hall, D., Jeter, J., et al. (2012). A GAL4-driver line resource for Drosophila neurobiology. Cell Rep. *2*, 991–1001. https://doi.org/10.1016/j.celrep.2012.09.011.
17. Pfeiffer, B.D., Jenett, A., Hammonds, A.S., Ngo, T.-T.B., Misra, S., Murphy, C., Scully, A., Carlson, J.W., Wan, K.H., Laverty, T.R., et al. (2008). Tools for neuroanatomy and neurogenetics in Drosophila. Proc. Natl. Acad. Sci. USA *105*, 9715–9720. https://doi.org/10.1073/pnas.0803697105.
18. Lee, T., and Luo, L. (2001). Mosaic analysis with a repressible cell marker (MARCM) for Drosophila neural development. Trends Neurosci. *24*, 251–254. https://doi.org/10.1016/s0166-2236(00)01791-4.
19. Demir, E., and Dickson, B.J. (2005). fruitless splicing specifies male courtship behavior in Drosophila. Cell *121*, 785–794. https://doi.org/10.1016/j.cell.2005.04.027.
20. Kimura, K.-I., Ote, M., Tazawa, T., and Yamamoto, D. (2005). Fruitless specifies sexually dimorphic neural circuitry in the Drosophila brain. Nature *438*, 229–233. https://doi.org/10.1038/nature04229.
21. Asahina, K., Watanabe, K., Duistermars, B.J., Hoopfer, E., González, C.R., Eyjólfsdóttir, E.A., Perona, P., and Anderson, D.J. (2014). Tachykinin-expressing neurons control male-specific aggressive arousal in Drosophila. Cell *156*, 221–235. https://doi.org/10.1016/j.cell.2013.11.045.
22. Kohatsu, S., Koganezawa, M., and Yamamoto, D. (2011). Female contact activates male-specific interneurons that trigger stereotypic courtship behavior in Drosophila. Neuron *69*, 498–508. https://doi.org/10.1016/j.neuron.2010.12.017.
23. Pan, Y., Meissner, G.W., and Baker, B.S. (2012). Joint control of Drosophila male courtship behavior by motion cues and activation of male-specific P1 neurons. Proc. Natl. Acad. Sci. USA *109*, 10065–10070. https://doi.org/10.1073/pnas.1207107109.
24. von Philipsborn, A.C., Liu, T., Yu, J.Y., Masser, C., Bidaye, S.S., and Dickson, B.J. (2011). Neuronal control of Drosophila courtship song. Neuron *69*, 509–522. https://doi.org/10.1016/j.neuron.2011.01.011.
25. Hoopfer, E.D., Jung, Y., Inagaki, H.K., Rubin, G.M., and Anderson, D.J. (2015). P1 interneurons promote a persistent internal state that enhances

inter-male aggression in Drosophila. eLife *4*, e11346. https://doi.org/10.7554/eLife.11346.

26. Anderson, D.J. (2016). Circuit modules linking internal states and social behaviour in flies and mice. Nat. Rev. Neurosci. *17*, 692–704. https://doi.org/10.1038/nrn.2016.125.

27. Kohl, J., Ostrovsky, A.D., Frechter, S., and Jefferis, G.S.X.E. (2013). A bidirectional circuit switch reroutes pheromone signals in male and female brains. Cell *155*, 1610–1623. https://doi.org/10.1016/j.cell.2013.11.025.

28. Nojima, T., Rings, A., Allen, A.M., Otto, N., Verschut, T.A., Billeter, J.-C., Neville, M.C., and Goodwin, S.F. (2021). A sex-specific switch between visual and olfactory inputs underlies adaptive sex differences in behavior. Curr. Biol. *31*, 1175–1191.e6. https://doi.org/10.1016/j.cub.2020.12.047.

29. Dorkenwald, S., Matsliah, A., Sterling, A.R., Schlegel, P., Yu, S.-C., McKellar, C.E., Lin, A., Costa, M., Eichler, K., Yin, Y., et al. (2024). Neuronal wiring diagram of an adult brain. Nature *634*, 124–138. https://doi.org/10.1038/s41586-024-07558-y.

30. Schlegel, P., Yin, Y., Bates, A.S., Dorkenwald, S., Eichler, K., Brooks, P., Han, D.S., Gkantia, M., Dos Santos, M., Munnelly, E.J., et al. (2024). Whole-brain annotation and multi-connectome cell typing of Drosophila. Nature *634*, 139–152. https://doi.org/10.1038/s41586-024-07686-5.

31. Scheffer, L.K., Xu, C.S., Januszewski, M., Lu, Z., Takemura, S.-Y., Hayworth, K.J., Huang, G.B., Shinomiya, K., Maitlin-Shepard, J., Berg, S., et al. (2020). A connectome and analysis of the adult Drosophila central brain. eLife *9*, e57443. https://doi.org/10.7554/eLife.57443.

32. Azevedo, A., Lesser, E., Phelps, J.S., Mark, B., Elabbady, L., Kuroda, S., Sustar, A., Moussa, A., Khandelwal, A., Dallmann, C.J., et al. (2024). Connectomic reconstruction of a female Drosophila ventral nerve cord. Nature *631*, 360–368. https://doi.org/10.1038/s41586-024-07389-x.

33. Marin, E.C., Morris, B.J., Stürner, T., Champion, A.S., Krzeminski, D., Badalamente, G., Gkantia, M., Dunne, C.R., Eichler, K., Takemura, S.-Y., et al. (2024). Systematic annotation of a complete adult male Drosophila nerve cord connectome reveals principles of functional organisation. eLife. https://doi.org/10.7554/elife.97766.1.

34. Takemura, S.-Y., Hayworth, K.J., Huang, G.B., Januszewski, M., Lu, Z., Marin, E.C., Preibisch, S., Xu, C.S., Bogovic, J., Champion, A.S., et al. (2024). A connectome of the male Drosophila ventral nerve cord. eLife. https://doi.org/10.7554/elife.97769.1.

35. Galili, D.S., Jefferis, G.S., and Costa, M. (2022). Connectomics and the neural basis of behaviour. Curr. Opin. Insect Sci. *54*, 100968. https://doi.org/10.1016/j.cois.2022.100968.

36. Schretter, C.E., Hindmarsh Sten, T., Klapoetke, N., Shao, M., Nern, A., Dreher, M., Bushey, D., Robie, A.A., Taylor, A.L., Branson, K., et al. (2025). Social state alters vision using three circuit mechanisms in Drosophila. Nature *637*, 646–653. https://doi.org/10.1038/s41586-024-08255-6.

37. Xu, C.S., Hayworth, K.J., Lu, Z., Grob, P., Hassan, A.M., García-Cerdán, J.G., Niyogi, K.K., Nogales, E., Weinberg, R.J., and Hess, H.F. (2017). Enhanced FIB-SEM systems for large-volume 3D imaging. eLife *6*, e25916. https://doi.org/10.7554/eLife.25916.

38. Xu, C.S., Pang, S., Shtengel, G., Müller, A., Ritter, A.T., Hoffman, H.K., Takemura, S.-Y., Lu, Z., Pasolli, H.A., Iyer, N., et al. (2021). An open-access volume electron microscopy atlas of whole cells and tissues. Nature *599*, 147–151. https://doi.org/10.1038/s41586-021-03992-4.

39. Nern, A., Loesche, F., Takemura, S.-Y., Burnett, L.E., Dreher, M., Gruntman, E., Hoeller, J., Huang, G.B., Januszewski, M., Klapoetke, N.C., et al. (2025). Connectome-driven neural inventory of a complete visual system. Nature *641*, 1225–1237. https://doi.org/10.1038/s41586-025-08746-0.

40. Januszewski, M., Kornfeld, J., Li, P.H., Pope, A., Blakely, T., Lindsey, L., Maitin-Shepard, J., Tyka, M., Denk, W., and Jain, V. (2018). High-precision automated reconstruction of neurons with flood-filling networks. Nat. Methods *15*, 605–610. https://doi.org/10.1038/s41592-018-0049-4.

41. Eckstein, N., Bates, A.S., Champion, A., Du, M., Yin, Y., Schlegel, P., Lu, A.K.-Y., Rymer, T., Finley-May, S., Paterson, T., et al. (2024). Neurotransmitter classification from electron microscopy images at synaptic sites in Drosophila melanogaster. Cell *187*, 2574–2594.e23. https://doi.org/10.1016/j.cell.2024.03.016.

42. Costa, M., Manton, J.D., Ostrovsky, A.D., Prohaska, S., and Jefferis, G.S.X.E. (2016). NBLAST: Rapid, Sensitive Comparison of Neuronal Structure and Construction of Neuron Family Databases. Neuron *91*, 293–311. https://doi.org/10.1016/j.neuron.2016.06.012.

43. Zheng, Z., Lauritzen, J.S., Perlman, E., Robinson, C.G., Nichols, M., Milkie, D., Torrens, O., Price, J., Fisher, C.B., Sharifi, N., et al. (2018). A Complete Electron Microscopy Volume of the Brain of Adult Drosophila melanogaster. Cell *174*, 730–743.e22. https://doi.org/10.1016/j.cell.2018.06.019.

44. Bidaye, S.S., Machacek, C., Wu, Y., and Dickson, B.J. (2014). Neuronal control of Drosophila walking direction. Science *344*, 97–101. https://doi.org/10.1126/science.1249964.

45. Okubo, T.S., Patella, P., D'Alessandro, I., and Wilson, R.I. (2020). A neural network for wind-guided compass navigation. Neuron *107*, 924–940.e18. https://doi.org/10.1016/j.neuron.2020.06.022.

46. Duistermars, B.J., and Frye, M.A. (2008). Crossmodal visual input for odor tracking during fly flight. Curr. Biol. *18*, 270–275. https://doi.org/10.1016/j.cub.2008.01.027.

47. Seelig, J.D., and Jayaraman, V. (2015). Neural dynamics for landmark orientation and angular path integration. Nature *521*, 186–191. https://doi.org/10.1038/nature14446.

48. Schretter, C.E., Aso, Y., Robie, A.A., Dreher, M., Dolan, M.-J., Chen, N., Ito, M., Yang, T., Parekh, R., Branson, K.M., et al. (2020). Cell types and neuronal circuitry underlying female aggression in Drosophila. eLife *9*, e58942. https://doi.org/10.7554/eLife.58942.

49. Dinitz, Y. (2006). Dinitz' Algorithm: The Original Version and Even's Version. In Theoretical Computer Science, O. Goldreich, A.L. Rosenberg, and A.L. Selman, eds. (Springer Berlin Heidelberg), pp. 218–240. https://doi.org/10.1007/11685654_10.

50. Wu, G., Ma, T., Hancock, C.E., Gonzalez, S., Aryal, B., Vaz, S., Chan, G., Palarca-Wong, M., Allen, N., Chung, C.-I., et al. (2024). Opposing GPCR signaling programs protein intake setpoint in Drosophila. Cell *187*, 5376–5392.e17. https://doi.org/10.1016/j.cell.2024.07.047.

51. Wang, K., Wang, F., Forknall, N., Yang, T., Patrick, C., Parekh, R., and Dickson, B.J. (2021). Neural circuit mechanisms of sexual receptivity in Drosophila females. Nature *589*, 577–581. https://doi.org/10.1038/s41586-020-2972-7.

52. Wang, F., Wang, K., Forknall, N., Patrick, C., Yang, T., Parekh, R., Bock, D., and Dickson, B.J. (2020). Neural circuitry linking mating and egg laying in Drosophila females. Nature *579*, 101–105. https://doi.org/10.1038/s41586-020-2055-9.

53. Mank, J.E., and Rideout, E.J. (2021). Developmental mechanisms of sex differences: from cells to organisms. Development *148*, dev199750. https://doi.org/10.1242/dev.199750.

54. Bates, A.S., Janssens, J., Jefferis, G.S., and Aerts, S. (2019). Neuronal cell types in the fly: single-cell anatomy meets single-cell genomics. Curr. Opin. Neurobiol. *56*, 125–134. https://doi.org/10.1016/j.conb.2018.12.012.

55. Zeng, H. (2022). What is a cell type and how to define it? Cell *185*, 2739–2755. https://doi.org/10.1016/j.cell.2022.06.031.

56. Cachero, S., Ostrovsky, A.D., Yu, J.Y., Dickson, B.J., and Jefferis, G.S.X.E. (2010). Sexual dimorphism in the fly brain. Curr. Biol. *20*, 1589–1601. https://doi.org/10.1016/j.cub.2010.07.045.

57. Lillvis, J.L., Wang, K., Shiozaki, H.M., Xu, M., Stern, D.L., and Dickson, B.J. (2024). Nested neural circuits generate distinct acoustic signals during Drosophila courtship. Curr. Biol. *34*, 808–824.e6. https://doi.org/10.1016/j.cub.2024.01.015.

58. Yu, J.Y., Kanai, M.I., Demir, E., Jefferis, G.S.X.E., and Dickson, B.J. (2010). Cellular organization of the neural circuit that drives Drosophila courtship behavior. Curr. Biol. *20*, 1602–1614. https://doi.org/10.1016/j.cub.2010.08.025.

59. Feng, K., Palfreyman, M.T., Häsemeyer, M., Talsma, A., and Dickson, B.J. (2014). Ascending SAG neurons control sexual receptivity of Drosophila females. Neuron *83*, 135–148. https://doi.org/10.1016/j.neuron.2014.05.017.

60. Shirangi, T.R., Stern, D.L., and Truman, J.W. (2013). Motor control of Drosophila courtship song. Cell Rep. *5*, 678–686. https://doi.org/10.1016/j.celrep.2013.09.039.

61. von Philipsborn, A.C., Jörchel, S., Tirian, L., Demir, E., Morita, T., Stern, D.L., and Dickson, B.J. (2014). Cellular and behavioral functions of fruitless isoforms in Drosophila courtship. Curr. Biol. *24*, 242–251. https://doi.org/10.1016/j.cub.2013.12.015.

62. Stürner, T., Brooks, P., Serratosa Capdevila, L., Morris, B.J., Javier, A., Fang, S., Gkantia, M., Cachero, S., Beckett, I.R., Marin, E.C., et al. (2025). Comparative connectomics of Drosophila descending and ascending neurons. Nature *643*, 158–172. https://doi.org/10.1038/s41586-025-08925-z.

63. Ren, Q., Awasaki, T., Huang, Y.-F., Liu, Z., and Lee, T. (2016). Cell Class-Lineage Analysis Reveals Sexually Dimorphic Lineage Compositions in the Drosophila Brain. Curr. Biol. *26*, 2583–2593. https://doi.org/10.1016/j.cub.2016.07.086.

64. Kimura, K.-I., Hachiya, T., Koganezawa, M., Tazawa, T., and Yamamoto, D. (2008). Fruitless and doublesex coordinate to generate male-specific neurons that can initiate courtship. Neuron *59*, 759–769. https://doi.org/10.1016/j.neuron.2008.06.007.

65. Ito, M., Masuda, N., Shinomiya, K., Endo, K., and Ito, K. (2013). Systematic analysis of neural projections reveals clonal composition of the Drosophila brain. Curr. Biol. *23*, 644–655. https://doi.org/10.1016/j.cub.2013.03.015.

66. Yu, H.-H., Awasaki, T., Schroeder, M.D., Long, F., Yang, J.S., He, Y., Ding, P., Kao, J.-C., Wu, G.Y.-Y., Peng, H., et al. (2013). Clonal development and organization of the adult Drosophila central brain. Curr. Biol. *23*, 633–643. https://doi.org/10.1016/j.cub.2013.02.057.

67. Schlegel, P., Bates, A.S., Stürner, T., Jagannathan, S.R., Drummond, N., Hsu, J., Serratosa Capdevila, L.S., Javier, A., Marin, E.C., Barth-Maron, A., et al. (2021). Information flow, cell types and stereotypy in a full olfactory connectome. Elife *10*, e66018. https://doi.org/10.7554/eLife.66018.

68. Luo, S.D., Shi, G.W., and Baker, B.S. (2011). Direct targets of the D. melanogaster DSXF protein and the evolution of sexual development. Development *138*, 2761–2771. https://doi.org/10.1242/dev.065227.

69. Neville, M.C., Nojima, T., Ashley, E., Parker, D.J., Walker, J., Southall, T., Van de Sande, B., Marques, A.C., Fischer, B., Brand, A.H., et al. (2014). Male-specific fruitless isoforms target neurodevelopmental genes to specify a sexually dimorphic nervous system. Curr. Biol. *24*, 229–241. https://doi.org/10.1016/j.cub.2013.11.035.

70. Chiang, A.-S., Lin, C.-Y., Chuang, C.-C., Chang, H.-M., Hsieh, C.-H., Yeh, C.-W., Shih, C.-T., Wu, J.-J., Wang, G.-T., Chen, Y.-C., et al. (2011). Three-dimensional reconstruction of brain-wide wiring networks in Drosophila at single-cell resolution. Curr. Biol. *21*, 1–11. https://doi.org/10.1016/j.cub.2010.11.056.

71. Connolly, K., Burnet, B., and Sewell, D. (1969). SELECTIVE MATING AND EYE PIGMENTATION: AN ANALYSIS OF THE VISUAL COMPONENT IN THE COURTSHIP BEHAVIOR OF DROSOPHILA MELANOGASTER. Evolution *23*, 548–559. https://doi.org/10.1111/j.1558-5646.1969.tb03540.x.

72. Markow, T.A., and Manning, M. (1980). Mating success of photoreceptor mutants of Drosophila melanogaster. Behav. Neural Biol. *29*, 276–280. https://doi.org/10.1016/s0163-1047(80)90612-3.

73. Ribeiro, I.M.A., Drews, M., Bahl, A., Machacek, C., Borst, A., and Dickson, B.J. (2018). Visual Projection Neurons Mediating Directed Courtship in Drosophila. Cell *174*, 607–621.e18. https://doi.org/10.1016/j.cell.2018.06.020.

74. Matsliah, A., Yu, S.-C., Kruk, K., Bland, D., Burke, A.T., Gager, J., Hebditch, J., Silverman, B., Willie, K.P., Willie, R., et al. (2024). Neuronal parts list and wiring diagram for a visual system. Nature *634*, 166–180. https://doi.org/10.1038/s41586-024-07981-1.

75. Bogovic, J.A., Otsuna, H., Heinrich, L., Ito, M., Jeter, J., Meissner, G., Nern, A., Colonell, J., Malkesman, O., Ito, K., et al. (2020). An unbiased template of the Drosophila brain and ventral nerve cord. PLoS One *15*, e0236495. https://doi.org/10.1371/journal.pone.0236495.

76. Zhao, A., Gruntman, E., Nern, A., Iyer, N., Rogers, E.M., Koskela, S., Siwanowicz, I., Dreher, M., Flynn, M.A., Laughland, C., et al. (2025). Eye structure shapes neuron function in Drosophila motion vision. Nature *646*, 135–142. https://doi.org/10.1038/s41586-025-09276-5.

77. Hindmarsh Sten, T., Li, R., Otopalik, A., and Ruta, V. (2021). Sexual arousal gates visual processing during Drosophila courtship. Nature *595*, 549–553. https://doi.org/10.1038/s41586-021-03714-w.

78. Collie, M.F., Jin, C., Rockwell, V., Kellogg, E., Vanderbeck, Q.X., Hartman, A.K., Holtz, S.L., and Wilson, R.I. (2026). Specialized parallel pathways for adaptive control of visual object pursuit. Neuron *114*, 1833–1847.e9. https://doi.org/10.1016/j.neuron.2026.01.001.

79. Seung, H.S. (2024). Predicting visual function by interpreting a neuronal wiring diagram. Nature *634*, 113–123. https://doi.org/10.1038/s41586-024-07953-5.

80. Cowley, B.R., Calhoun, A.J., Rangarajan, N., Ireland, E., Turner, M.H., Pillow, J.W., and Murthy, M. (2024). Mapping model units to visual neurons reveals population code for social behaviour. Nature *629*, 1100–1108. https://doi.org/10.1038/s41586-024-07451-8.

81. Keleş, M.F., and Frye, M.A. (2017). Object-Detecting Neurons in Drosophila. Curr. Biol. *27*, 680–687. https://doi.org/10.1016/j.cub.2017.01.012.

82. Perry, M.W., and Desplan, C. (2016). Love spots. Curr. Biol. *26*, R484–R485. https://doi.org/10.1016/j.cub.2016.02.020.

83. Hardie, R.C. (1983). Projection and connectivity of sex-specific photoreceptors in the compound eye of the male housefly (Musca domestica). Cell Tissue Res. *233*, 1–21. https://doi.org/10.1007/BF00222228.

84. Land, M.F., and Collett, T.S. (1974). Chasing behaviour of houseflies (Fannia canicularis). J. Comp. Physiol. *89*, 331–357. https://doi.org/10.1007/bf00695351.

85. Hausen, K., and Strausfeld, N.J. (1980). Sexually dimorphic interneuron arrangements in the fly visual system. Proc. R. Soc. Lond. A *208*, 57–71. https://doi.org/10.1098/rspb.1980.0042.

86. Land, M.F., and Eckert, H. (1985). Maps of the acute zones of fly eyes. J. Comp. Physiol. A: Neuroethol. Sens. Neural Behav. Physiol. *156*, 525–538. https://doi.org/10.1007/bf00613976.

87. Nordström, K., Barnett, P.D., Moyer de Miguel, I.M., Brinkworth, R.S.A., and O'Carroll, D.C. (2008). Sexual dimorphism in the hoverfly motion vision pathway. Curr. Biol. *18*, 661–667. https://doi.org/10.1016/j.cub.2008.03.061.

88. Gilbert, C., and Strausfeld, N.J. (1991). The functional organization of male-specific visual neurons in flies. J. Comp. Physiol. A *169*, 395–411. https://doi.org/10.1007/BF00197653.

89. McKellar, C.E., Lillvis, J.L., Bath, D.E., Fitzgerald, J.E., Cannon, J.G., Simpson, J.H., and Dickson, B.J. (2019). Threshold-Based Ordering of Sequential Actions during Drosophila Courtship. Curr. Biol. *29*, 426–434.e6. https://doi.org/10.1016/j.cub.2018.12.019.

90. Yang, H.H., Brezovec, B.E., Serratosa Capdevila, L., Vanderbeck, Q.X., Adachi, A., Mann, R.S., and Wilson, R.I. (2024). Fine-grained descending control of steering in walking Drosophila. Cell *187*, 6290–6308.e27. https://doi.org/10.1016/j.cell.2024.08.033.

91. Ewing, A.W., and Bennet-Clark, H.C. (1968). The courtship songs of Drosophila. Behaviour *31*, 288–301. https://doi.org/10.1163/156853968X00298.

92. Cowling, D.E., and Burnet, B. (1981). Courtship songs and genetic control of their acoustic characteristics in sibling species of the Drosophila melanogaster subgroup. Anim. Behav. *29*, 924–935. https://doi.org/10.1016/s0003-3472(81)80030-9.

93. Spieth, H.T. (1974). Courtship behavior in Drosophila. Annu. Rev. Entomol. *19*, 385–405. https://doi.org/10.1146/annurev.en.19.010174.002125.

94. Hall, J.C. (1994). The mating of a fly. Science *264*, 1702–1714. https://doi.org/10.1126/science.8209251.

95. Shiozaki, H.M., Wang, K., Lillvis, J.L., Xu, M., Dickson, B.J., and Stern, D.L. (2024). Activity of nested neural circuits drives different courtship songs in Drosophila. Nat. Neurosci. *27*, 1954–1965. https://doi.org/10.1038/s41593-024-01738-9.

96. Bennet-Clark, H.C., and Ewing, A.W. (1969). Pulse interval as a critical parameter in the courtship song of Drosophila melanogaster. Anim. Behav. *17*, 755–759. https://doi.org/10.1016/s0003-3472(69)80023-0.

97. von Schilcher, F. (1976). The role of auditory stimuli in the courtship of Drosophila melanogaster. Anim. Behav. *24*, 18–26. https://doi.org/10.1016/s0003-3472(76)80095-4.

98. Schilcher, F. von (1976). The function of pulse song and sine song in the courtship of Drosophila melanogaster. Anim. Behav. *24*, 622–625. https://doi.org/10.1016/s0003-3472(76)80076-0.

99. Zhou, C., Franconville, R., Vaughan, A.G., Robinett, C.C., Jayaraman, V., and Baker, B.S. (2015). Central neural circuitry mediating courtship song perception in male Drosophila. eLife *4*, e08477. https://doi.org/10.7554/eLife.08477.

100. Hindmarsh Sten, T., Li, R., Hollunder, F., Eleazer, S., and Ruta, V. (2025). Male-male interactions shape mate selection in Drosophila. Cell *188*, 1486–1503.e25. https://doi.org/10.1016/j.cell.2025.01.008.

101. Vaughan, A.G., Zhou, C., Manoli, D.S., and Baker, B.S. (2014). Neural pathways for the detection and discrimination of conspecific song in D. melanogaster. Curr. Biol. *24*, 1039–1049. https://doi.org/10.1016/j.cub.2014.03.048.

102. Kamikouchi, A., Inagaki, H.K., Effertz, T., Hendrich, O., Fiala, A., Göpfert, M.C., and Ito, K. (2009). The neural basis of Drosophila gravity-sensing and hearing. Nature *458*, 165–171. https://doi.org/10.1038/nature07810.

103. Eberl, D.F., Duyk, G.M., and Perrimon, N. (1997). A genetic screen for mutations that disrupt an auditory response in Drosophila melanogaster. Proc. Natl. Acad. Sci. USA *94*, 14837–14842. https://doi.org/10.1073/pnas.94.26.14837.

104. Hampel, S., Eichler, K., Yamada, D., Bock, D.D., Kamikouchi, A., and Seeds, A.M. (2020). Distinct subpopulations of mechanosensory chordotonal organ neurons elicit grooming of the fruit fly antennae. eLife *9*, e59976. https://doi.org/10.7554/eLife.59976.

105. Patella, P., and Wilson, R.I. (2018). Functional Maps of Mechanosensory Features in the Drosophila Brain. Curr. Biol. *28*, 1189–1203.e5. https://doi.org/10.1016/j.cub.2018.02.074.

106. Kim, H., Horigome, M., Ishikawa, Y., Li, F., Lauritzen, J.S., Card, G., Bock, D.D., and Kamikouchi, A. (2020). Wiring patterns from auditory sensory neurons to the escape and song-relay pathways in fruit flies. J. Comp. Neurol. *528*, 2068–2098. https://doi.org/10.1002/cne.24877.

107. Lai, J.S.-Y., Lo, S.-J., Dickson, B.J., and Chiang, A.-S. (2012). Auditory circuit in the Drosophila brain. Proc. Natl. Acad. Sci. USA *109*, 2607–2612. https://doi.org/10.1073/pnas.1117307109.

108. Tootoonian, S., Coen, P., Kawai, R., and Murthy, M. (2012). Neural representations of courtship song in the Drosophila brain. J. Neurosci. *32*, 787–798. https://doi.org/10.1523/JNEUROSCI.5104-11.2012.

109. Baker, C.A., McKellar, C., Pang, R., Nern, A., Dorkenwald, S., Pacheco, D.A., Eckstein, N., Funke, J., Dickson, B.J., and Murthy, M. (2022). Neural network organization for courtship-song feature detection in Drosophila. Curr. Biol. *32*, 3317–3333.e7. https://doi.org/10.1016/j.cub.2022.06.019.

110. Deutsch, D., Clemens, J., Thiberge, S.Y., Guan, G., and Murthy, M. (2023). Shared Song Detector Neurons in Drosophila Male and Female Brains Drive Sex-Specific Behaviors. Curr. Biol. *33*, 3796–3800. https://doi.org/10.1016/j.cub.2023.08.006.

111. Clemens, J., Girardin, C.C., Coen, P., Guan, X.-J., Dickson, B.J., and Murthy, M. (2018). Connecting Neural Codes with Behavior in the Auditory System of Drosophila. Neuron *97*, 475. https://doi.org/10.1016/j.neuron.2017.12.033.

112. Poulet, J.F.A., and Hedwig, B. (2002). A corollary discharge maintains auditory sensitivity during sound production. Nature *418*, 872–876. https://doi.org/10.1038/nature00919.

113. Kurtovic, A., Widmer, A., and Dickson, B.J. (2007). A single class of olfactory neurons mediates behavioural responses to a Drosophila sex pheromone. Nature *446*, 542–546. https://doi.org/10.1038/nature05672.

114. Stowers, L., and Logan, D.W. (2010). Sexual dimorphism in olfactory signaling. Curr. Opin. Neurobiol. *20*, 770–775. https://doi.org/10.1016/j.conb.2010.08.015.

115. Antony, C., Davis, T.L., Carlson, D.A., Pechine, J.M., and Jallon, J.M. (1985). Compared behavioral responses of maleDrosophila melanogaster (Canton S) to natural and synthetic aphrodisiacs. J. Chem. Ecol. *11*, 1617–1629. https://doi.org/10.1007/BF01012116.

116. Billeter, J.-C., Atallah, J., Krupp, J.J., Millar, J.G., and Levine, J.D. (2009). Specialized cells tag sexual and species identity in Drosophila melanogaster. Nature *461*, 987–991. https://doi.org/10.1038/nature08495.

117. Ferveur, J.F., Savarit, F., O'Kane, C.J., Sureau, G., Greenspan, R.J., and Jallon, J.M. (1997). Genetic feminization of pheromones and its behavioral consequences in Drosophila males. Science *276*, 1555–1558. https://doi.org/10.1126/science.276.5318.1555.

118. van der Goes van Naters, W., and Carlson, J.R. (2007). Receptors and neurons for fly odors in Drosophila. Curr. Biol. *17*, 606–612. https://doi.org/10.1016/j.cub.2007.02.043.

119. Ha, T.S., and Smith, D.P. (2006). A pheromone receptor mediates 11-cis-vaccenyl acetate-induced responses in Drosophila. J. Neurosci. *26*, 8727–8733. https://doi.org/10.1523/JNEUROSCI.0876-06.2006.

120. Grosjean, Y., Rytz, R., Farine, J.-P., Abuin, L., Cortot, J., Jefferis, G.S.X.E., and Benton, R. (2011). An olfactory receptor for food-derived odours promotes male courtship in Drosophila. Nature *478*, 236–240. https://doi.org/10.1038/nature10428.

121. Hansson, B.S., Christensen, T.A., and Hildebrand, J.G. (1991). Functionally distinct subdivisions of the macroglomerular complex in the antennal lobe of the male sphinx moth Manduca sexta. J. Comp. Neurol. *312*, 264–278. https://doi.org/10.1002/cne.903120209.

122. Stockinger, P., Kvitsiani, D., Rotkopf, S., Tirián, L., and Dickson, B.J. (2005). Neural circuitry that governs Drosophila male courtship behavior. Cell *121*, 795–807. https://doi.org/10.1016/j.cell.2005.04.026.

123. Grabe, V., Baschwitz, A., Dweck, H.K.M., Lavista-Llanos, S., Hansson, B.S., and Sachse, S. (2016). Elucidating the neuronal architecture of olfactory glomeruli in the Drosophila antennal lobe. Cell Rep. *16*, 3401–3413. https://doi.org/10.1016/j.celrep.2016.08.063.

124. Takagi, S., Sancer, G., Abuin, L., Stupski, S.D., Roman Arguello, J., Prieto-Godino, L.L., Stern, D.L., Cruchet, S., Álvarez-Ocaña, R., Wienecke, C.F.R., et al. (2024). Olfactory sensory neuron population expansions influence projection neuron adaptation and enhance odour tracking. Nat. Commun. *15*, 7041. https://doi.org/10.1038/s41467-024-50808-w.

125. Tanaka, N.K., Hirao, T., Chida, H., and Ejima, A. (2021). A Sexually Dimorphic Olfactory Neuron Mediates Fixed Action Transition during Courtship Ritual in Drosophila melanogaster. J. Neurosci. *41*, 9732–9741. https://doi.org/10.1523/JNEUROSCI.1168-21.2021.

126. Jefferis, G.S.X.E., Potter, C.J., Chan, A.M., Marin, E.C., Rohlfing, T., Maurer, C.R., Jr., and Luo, L. (2007). Comprehensive maps of Drosophila higher olfactory centers: spatially segregated fruit and pheromone representation. Cell *128*, 1187–1203. https://doi.org/10.1016/j.cell.2007.01.040.

127. de Belle, J.S., and Heisenberg, M. (1994). Associative odor learning in Drosophila abolished by chemical ablation of mushroom bodies. Science *263*, 692–695. https://doi.org/10.1126/science.8303280.

128. Davis, R.L. (1993). Mushroom bodies and Drosophila learning. Neuron *11*, 1–14. https://doi.org/10.1016/0896-6273(93)90266-t.

129. Heisenberg, M., Borst, A., Wagner, S., and Byers, D. (1985). Drosophila mushroom body mutants are deficient in olfactory learning. J. Neurogenet. *2*, 1–30. https://doi.org/10.3109/01677068509100140.

130. Stocker, R.F. (1994). The organization of the chemosensory system in Drosophila melanogaster: a review. Cell Tissue Res. *275*, 3–26. https://doi.org/10.1007/BF00305372.

131. Tastekin, I., de Haan Vicente, I., Beresford, R.J., Morris, B.J., Beckett, I., Schlegel, P., Gkantia, M., FlyEM Project Team; Cambridge Connectomics Group, and Marin, E.C., et al. (2026). The complete gustatory connectome of adult *Drosophila* reveals how taste guides feeding, foraging, and social behavior. Cell *189*. https://doi.org/10.1016/j.cell.2026.08.016.

132. Tastekin, I., de Haan Vicente, I., Beresford, R.J., Otto, N., Dempsey, G., Waddell, S., and Ribeiro, C. (2025). Connectomics reveals a feed-forward swallowing circuit driving protein appetite. Preprint at bioRxiv. https://doi.org/10.1101/2025.08.25.671815.

133. Mellert, D.J., Knapp, J.-M., Manoli, D.S., Meissner, G.W., and Baker, B.S. (2010). Midline crossing by gustatory receptor neuron axons is regulated by fruitless, doublesex and the Roundabout receptors. Development *137*, 323–332. https://doi.org/10.1242/dev.045047.

134. Benjamini, Y., and Hochberg, Y. (1995). Controlling the false discovery rate: A practical and powerful approach to multiple testing. J. R. Stat. Soc. B *57*, 289–300. https://doi.org/10.1111/j.2517-6161.1995.tb02031.x.

135. Ito, H., Sato, K., Kondo, S., Ueda, R., and Yamamoto, D. (2016). Fruitless represses robo1 transcription to shape male-specific neural morphology and behavior in Drosophila. Curr. Biol. *26*, 1532–1542. https://doi.org/10.1016/j.cub.2016.04.067.

136. Rubin, G.M., Managan, C.M., Dreher, M., Kim, E., Miller, S.W., Boone, K., Robie, A., Taylor, A.L., Branson, K., Schretter, C.E., et al. (2026). Networks of sexually dimorphic neurons that regulate social behaviors in *Drosophila*. Current Biology *36*. https://doi.org/10.1016/j.cub.2026.08.013.

137. Deutsch, D., Matsliah, A., Wang, K., Dorkenwald, S., Mondal, A., Burke, A., Hebditch, J., Gager, J., Yu, S.-C., Sterling, A., et al. (2025). Sexually-dimorphic neurons in the Drosophila whole-brain connectome. Preprint at bioRxiv. https://doi.org/10.1101/2025.06.10.658788.

138. Cook, S.J., Jarrell, T.A., Brittin, C.A., Wang, Y., Bloniarz, A.E., Yakovlev, M.A., Nguyen, K.C.Q., Tang, L.T.-H., Bayer, E.A., Duerr, J.S., et al. (2019). Whole-animal connectomes of both Caenorhabditis elegans sexes. Nature *571*, 63–71. https://doi.org/10.1038/s41586-019-1352-7.

139. Manoli, D.S., Foss, M., Villella, A., Taylor, B.J., Hall, J.C., and Baker, B.S. (2005). Male-specific fruitless specifies the neural substrates of Drosophila courtship behaviour. Nature *436*, 395–400. https://doi.org/10.1038/nature03859.

140. Roberts, R.J.V., Pop, S., and Prieto-Godino, L.L. (2022). Evolution of central neural circuits: state of the art and perspectives. Nat. Rev. Neurosci. *23*, 725–743. https://doi.org/10.1038/s41583-022-00644-y.

141. Roberts, R.J.V., Giez, C., Dhawan, S., Pang, S., Randel, N., Lu, Z., Gong, H., Dekens, L., Di Frisco, J., Xu, C.S., et al. (2025). Cross-species comparative connectomics reveals the evolution of an olfactory circuit. Preprint at bioRxiv. https://doi.org/10.1101/2025.06.11.659158.

142. Phelps, J.S., Hildebrand, D.G.C., Graham, B.J., Kuan, A.T., Thomas, L.A., Nguyen, T.M., Buhmann, J., Azevedo, A.W., Sustar, A., Agrawal, S., et al. (2021). Reconstruction of motor control circuits in adult Drosophila using automated transmission electron microscopy. Cell *184*, 759–774.e18. https://doi.org/10.1016/j.cell.2020.12.013.

143. Bates, A.S., Phelps, J.S., Kim, M., Yang, H.H., Matsliah, A., Ajabi, Z., Perlman, E., Delgado, K.M., Osman, M.A.M., Salmon, C.K., et al. (2026). Distributed control circuits across a brain-and-cord connectome. Nature. https://doi.org/10.1038/s41586-026-10735-w.

144. Lappalainen, J.K., Tschopp, F.D., Prakhya, S., McGill, M., Nern, A., Shinomiya, K., Takemura, S.-Y., Gruntman, E., Macke, J.H., and Turaga, S.C. (2024). Connectome-constrained networks predict neural activity across the fly visual system. Nature *634*, 1132–1140. https://doi.org/10.1038/s41586-024-07939-3.

145. Shiu, P.K., Sterne, G.R., Spiller, N., Franconville, R., Sandoval, A., Zhou, J., Simha, N., Kang, C.H., Yu, S., Kim, J.S., et al. (2024). A Drosophila computational brain model reveals sensorimotor processing. Nature *634*, 210–219. https://doi.org/10.1038/s41586-024-07763-9.

146. Cachero, S., Mitletton, M., Beckett, I.R., Marin, E.C., Serratosa Capdevila, L., Gkantia, M., Soffers, J.H.M., Lacin, H., Jefferis, G.S.X.E., and Donà, E. (2026). A global molecular code for birth order and neuronal identity in Drosophila. Nature. https://doi.org/10.1038/s41586-026-10797-w.

147. Allen, A.M., Neville, M.C., Nojima, T., Alejevski, F., and Goodwin, S.F. (2026). Differential neuronal survival defines a novel axis of sexual dimorphism in the Drosophila brain. Cell Genom. *6*, 101125. https://doi.org/10.1016/j.xgen.2025.101125.

148. Elkahlah, N.A., Lin, Y., Pan, Y., Carter, J.A., Shirangi, T.R., and Clowney, E.J. (2026). Transcription factor codes patterning neuronal groundplans of the cerebrum. Nature *655*, 1252–1261. https://doi.org/10.1038/s41586-026-10526-3.

149. Kovács, I.A., Barabási, D.L., and Barabási, A.-L. (2020). Uncovering the genetic blueprint of the C. elegans nervous system. Proc. Natl. Acad. Sci. USA *117*, 33570–33577. https://doi.org/10.1073/pnas.2009093117.

150. Pan, Y., and Baker, B.S. (2014). Genetic identification and separation of innate and experience-dependent courtship behaviors in Drosophila. Cell *156*, 236–248. https://doi.org/10.1016/j.cell.2013.11.041.

151. Ishii, K., Cortese, M., Leng, X., Shokhirev, M.N., and Asahina, K. (2022). A neurogenetic mechanism of experience-dependent suppression of aggression. Sci. Adv. *8*, eabg3203. https://doi.org/10.1126/sciadv.abg3203.

152. Yu, S.-C., Bae, J.A., Matsliah, A., Dorkenwald, S., Gager, J., Hebditch, J., Silverman, B., Willie, K.P., Willie, R., Burke, A.T., et al. (2025). New synapse detection in the whole-brain connectome of *Drosophila*. Preprint at bioRxiv. https://doi.org/10.1101/2025.07.11.664377.

153. Bates, A.S., Manton, J.D., Jagannathan, S.R., Costa, M., Schlegel, P., Rohlfing, T., and Jefferis, G.S. (2020). The natverse, a versatile toolbox for combining and analysing neuroanatomical data. eLife *9*, e53350. https://doi.org/10.7554/eLife.53350.

154. Schlegel, P., Barnes, C., Loesche, F., Champion, A., Jagannathan, S., Court, R., Choi, J., Collman, F., Tanadi, G., Berg, S., et al. navis-org/navis, Version 1.11.0. Zenodo.https://doi.org/10.5281/zenodo.18801093.

155. Plaza, S.M., Clements, J., Dolafi, T., Umayam, L., Neubarth, N.N., Scheffer, L.K., and Berg, S. (2022). neuPrint: An open access tool for EM connectomics. Front. Neuroinform. *16*, 896292. https://doi.org/10.3389/fninf.2022.896292.

156. Schlegel, P., and Court, R. navis-org/navis-flybrains, Version 0.6.3. Zenodo. https://doi.org/10.5281/zenodo.17632973.

157. Peixoto, T.P. (2017). The Graph-Tool Python Library (figshare). https://doi.org/10.6084/M9.FIGSHARE.1164194.

158. Peixoto, T.P. (2017). Nonparametric Bayesian inference of the microcanonical stochastic block model. Phys. Rev. E *95*, 012317. https://doi.org/10.1103/PhysRevE.95.012317.

159. Hayworth, K.J., Xu, C.S., Lu, Z., Knott, G.W., Fetter, R.D., Tapia, J.C., Lichtman, J.W., and Hess, H.F. (2015). Ultrastructurally smooth thick partitioning and volume stitching for large-scale connectomics. Nat. Methods *12*, 319–322. https://doi.org/10.1038/nmeth.3292.

160. Bates, A.S., Jefferis, G.S.X.E., Adjavon, D.-Y., and Funke, J. drosophila_-neurotransmitters: A curated database of neurotransmitter usage by Drosophila cell types. Zenodo. https://doi.org/10.5281/zenodo.20818141.

161. He, K., Zhang, X., Ren, S., and Sun, J. (2016). Deep residual learning for image recognition. In 2016 IEEE Conference on Computer Vision and Pattern Recognition (CVPR) (Institute of Electrical and Electronics Engineers), pp. 770–778. https://doi.org/10.1109/CVPR.2016.90.

162. Lesser, E., Azevedo, A.W., Phelps, J.S., Elabbady, L., Cook, A., Syed, D.S., Mark, B., Kuroda, S., Sustar, A., Moussa, A., et al. (2024). Synaptic architecture of leg and wing premotor control networks in Drosophila. Nature *631*, 369–377. https://doi.org/10.1038/s41586-024-07600-z.

163. Zhao, T., Olbris, D.J., Yu, Y., and Plaza, S.M. (2018). NeuTu: Software for collaborative, large-scale, segmentation-based connectome reconstruction. Front. Neural Circuits *12*, 101. https://doi.org/10.3389/fncir.2018.00101.

164. Hubbard, P.M., Berg, S., Zhao, T., Olbris, D.J., Umayam, L., Maitin-Shepard, J., Januszewski, M., Katz, W.T., Neace, E.R., and Plaza, S.M. (2020). Accelerated EM connectome reconstruction using 3D visualization and segmentation graphs. Preprint at bioRxiv. https://doi.org/10.1101/2020.01.17.909572.

165. Katz, W.T., and Plaza, S.M. (2019). DVID: Distributed versioned image-oriented dataservice. Front. Neural Circuits *13*, 5. https://doi.org/10.3389/fncir.2019.00005.

166. Huang, G.B., Katz, W.M., Berg, S., and Scheffer, L. (2025). Autoproof: Automated Segmentation Proofreading for Connectomics. Preprint at arXiv. https://doi.org/10.48550/ARXIV.2509.26585.

167. Klein, S., Staring, M., Murphy, K., Viergever, M.A., and Pluim, J.P.W. (2010). Elastix: A toolbox for intensity-based medical image registration. IEEE Trans. Med. Imaging *29*, 196–205. https://doi.org/10.1109/TMI.2009.2035616.

168. Bogovic, J.A., Hanslovsky, P., Wong, A., and Saalfeld, S. (2016). Robust registration of calcium images by learned contrast synthesis. In 13th International Symposium on Biomedical Imaging (ISBI) (IEEE) https://doi.org/10.1109/isbi.2016.7493463.

169. Lovick, J.K., Ngo, K.T., Omoto, J.J., Wong, D.C., Nguyen, J.D., and Hartenstein, V. (2013). Postembryonic lineages of the Drosophila brain: I. Development of the lineage-associated fiber tracts. Dev. Biol. *384*, 228–257. https://doi.org/10.1016/j.ydbio.2013.07.008.

170. Wong, D.C., Lovick, J.K., Ngo, K.T., Borisuthirattana, W., Omoto, J.J., and Hartenstein, V. (2013). Postembryonic lineages of the Drosophila brain: II. Identification of lineage projection patterns based on MARCM clones. Dev. Biol. *384*, 258–289. https://doi.org/10.1016/j.ydbio.2013.07.009.

171. Harris, R.M., Pfeiffer, B.D., Rubin, G.M., and Truman, J.W. (2015). Neuron hemilineages provide the functional ground plan for the Drosophila ventral nervous system. eLife *4*, e04493. https://doi.org/10.7554/eLife.04493.

172. Taisz, I., Donà, E., Münch, D., Bailey, S.N., Morris, B.J., Meechan, K.I., Stevens, K.M., Varela-Martínez, I., Gkantia, M., Schlegel, P., et al. (2023). Generating parallel representations of position and identity in the olfactory system. Cell *186*, 2556–2573.e22. https://doi.org/10.1016/j.cell.2023.04.038.

173. Court, R., Costa, M., Pilgrim, C., Millburn, G., Holmes, A., McLachlan, A., Larkin, A., Matentzoglu, N., Kir, H., Parkinson, H., et al. (2023). Virtual Fly Brain-An interactive atlas of the nervous system. Front. Physiol. *14*, 1076533. https://doi.org/10.3389/fphys.2023.1076533.

174. Wu, J.S., and Luo, L. (2006). A protocol for dissecting Drosophila melanogaster brains for live imaging or immunostaining. Nat. Protoc. *1*, 2110–2115. https://doi.org/10.1038/nprot.2006.336.

175. Costa, M., Ostrovsky, A.D., Cachero, S., and Jefferis, G.S.X. (2014). Cross-Referenced Nomenclature for Fruitless Neurons in the Drosophila Brain (figshare). https://doi.org/10.6084/m9.figshare.1030641.v1.

176. Hulse, B.K., Haberkern, H., Franconville, R., Turner-Evans, D., Takemura, S.-Y., Wolff, T., Noorman, M., Dreher, M., Dan, C., Parekh, R., et al. (2021). A connectome of the Drosophila central complex reveals network motifs suitable for flexible navigation and context-dependent action selection. eLife *10*, e66039. https://doi.org/10.7554/eLife.66039.

177. Cheong, H.S.J., Eichler, K., Stürner, T., Asinof, S.K., Champion, A.S., Marin, E.C., Oram, T.B., Sumathipala, M., Venkatasubramanian, L., Namiki, S., et al. (2025). Transforming descending input into motor output: An analysis of the Drosophila Male Adult Nerve Cord connectome. eLife *13*, RP96084. https://doi.org/10.7554/elife.96084.2.

178. Virtanen, P., Gommers, R., Oliphant, T.E., Haberland, M., Reddy, T., Cournapeau, D., Burovski, E., Peterson, P., Weckesser, W., Bright, J., et al. (2020). SciPy 1.0: fundamental algorithms for scientific computing in Python. Nat. Methods *17*, 261–272. https://doi.org/10.1038/s41592-019-0686-2.

179. Yin, Y., Hoeller, J., Mathiasen, A., Tsang, J.M.F., Charrier, M.E., and Cardona, A. (2025). The Connectome Interpreter Toolkit. Preprint at bioRxiv. https://doi.org/10.1101/2025.09.29.679410.

180. Winding, M., Pedigo, B.D., Barnes, C.L., Patsolic, H.G., Park, Y., Kazimiers, T., Fushiki, A., Andrade, I.V., Khandelwal, A., Valdes-Aleman, J., et al. (2023). The connectome of an insect brain. Science *379*, eadd9330. https://doi.org/10.1126/science.add9330.

181. Vosshall, L.B., Wong, A.M., and Axel, R. (2000). An olfactory sensory map in the fly brain. Cell *102*, 147–159. https://doi.org/10.1016/s0092-8674(00)00021-0.

182. Bates, A.S., Schlegel, P., Roberts, R.J.V., Drummond, N., Tamimi, I.F.M., Turnbull, R., Zhao, X., Marin, E.C., Popovici, P.D., Dhawan, S., et al. (2020). Complete Connectomic Reconstruction of Olfactory Projection Neurons in the Fly Brain. Curr. Biol. *30*, 3183–3199.e6. https://doi.org/10.1016/j.cub.2020.06.042.

183. Task, D., Lin, C.-C., Vulpe, A., Afify, A., Ballou, S., Brbic, M., Schlegel, P., Raji, J., Jefferis, G.S.X.E., Li, H., et al. (2022). Chemoreceptor co-expression in Drosophila melanogaster olfactory neurons. eLife *11*, e72599. https://doi.org/10.7554/eLife.72599.

184. Wilson, R.I., and Mainen, Z.F. (2006). Early events in olfactory processing. Annu. Rev. Neurosci. *29*, 163–201. https://doi.org/10.1146/annurev.neuro.29.051605.112950.

185. Marin, E.C., Büld, L., Theiss, M., Sarkissian, T., Roberts, R.J.V., Turnbull, R., Tamimi, I.F.M., Pleijzier, M.W., Laursen, W.J., Drummond, N., et al. (2020). Connectomics Analysis Reveals First-, Second-, and Third-Order Thermosensory and Hygrosensory Neurons in the Adult Drosophila Brain. Curr. Biol. *30*, 3167–3182.e4. https://doi.org/10.1016/j.cub.2020.06.028.

186. Peixoto, T.P. (2023). Descriptive vs. Inferential Community Detection in Networks: Pitfalls, Myths and Half-Truths (Cambridge University Press). https://doi.org/10.1017/9781009118897.

187. Peixoto, T.P. (2014). Hierarchical Block Structures and High-Resolution Model Selection in Large Networks. Phys. Rev. X *4*, 011047. https://doi.org/10.1103/PhysRevX.4.011047.

188. Betzel, R., Puxeddu, M.G., and Seguin, C. (2024). Hierarchical communities in the larval Drosophila connectome: Links to cellular annotations and network topology. Proc. Natl. Acad. Sci. USA *121*, e2320177121. https://doi.org/10.1073/pnas.2320177121.

189. Peixoto, T.P. (2020). Merge-split Markov chain Monte Carlo for community detection. Phys. Rev. E *102*, 012305. https://doi.org/10.1103/PhysRevE.102.012305.

STAR★METHODS

KEY RESOURCES TABLE

REAGENT or RESOURCE	SOURCE	IDENTIFIER
Deposited data		
Adult male *Drosophila melanogaster* central nervous system electron microscopy dataset with segmentation, reconstructed neurons, skeletons, annotations and connectivity data	This paper	https://male-cns.janelia.org; https://neuprint.janelia.org
Experimental models: Organisms/strains		
Drosophila melanogaster: 5 day old adult males from isogenized CantonS strain G1 × w^{1118} cross	Bloomington Drosophila Stock Center	RRID:BDSC_64349; RRID:BDSC_3605
Software and algorithms		
malecns: Support for working with male CNS segmentation, meshes and annotations in R	This paper	https://github.com/natverse/malecns
coconatfly: analysis suite of comparative connectomics in R	Schlegel et al.[30]	https://github.com/natverse/coconatfly
fafbseg: support for working with FAFB/FlyWire segmentation, meshes and annotations in R	Bates et al.[153]	https://github.com/natverse/fafbseg
malevnc: support for working with MANC segmentation, meshes and annotations in R	Marin et al.[33]	https://github.com/natverse/malevnc
neuprintr: support for working with neuPrint databases in R	Bates et al.[153]	https://github.com/natverse/neuprintr
navis: Python library for neuroanatomical analyses	Schlegel et al.[154]	https://github.com/navis-org/navis; Zenodo: 10.5281/zenodo.18801093
neuprint-python: Python API for working with neuPrint databases	Plaza et al.[155]	https://github.com/connectome-neuprint/neuprint-python
bigclust: set of GUI tools for inspecting neuron clusterings and assigning annotations	This paper	https://github.com/flyconnectome/bigclust
cocoa: Python tools for connectivity co-clustering	Schlegel et al.[30]	https://github.com/flyconnectome/cocoa
NBLAST scoring matrices: scoring matrices for NBLAST generated from cross-matched neurons	This paper	https://github.com/flyconnectome/nblast-scoremats
fafbseg-py: support for working with FAFB/FlyWire segmentation, neuron meshes/skeletons and annotations in Python	Schlegel et al.[30]	https://github.com/navis-org/fafbseg-py
flybrains: Python package bundling spatial transform between various template spaces, including to/from the male CNS, used in combination with navis	Schlegel and Court[156]	https://github.com/navis-org/navis-flybrains; Zenodo: 10.5281/zenodo.17632973
graph-tool: Python package for network analysis and inference	Peixoto[157,158]	https://graph-tool.skewed.de/; https://git.skewed.de/count0/graph-tool
Other		
Resource website for this publication	This paper	https://male-cns.janelia.org

EXPERIMENTAL MODEL AND STUDY PARTICIPANT DETAILS

Drosophila melanogaster five-day-old males from a cross between Canton S strain G1 × w^{1118} were raised on a 12-h day-night cycle and dissected 1.5 h after lights on with a single specimen ultimately selected for imaging.

METHOD DETAILS

EM Sample Preparation

Methods for sample preparation were described in detail in Nern et al.,[39] an earlier study of the same sample. Briefly, hundreds of five-day-old *Drosophila melanogaster* males were dissected to extract the CNS intact, including the brain, VNC and neck connective. After a multi-stage fixation and staining process, each was inspected for significant damage, with special attention to the fragile neck connective. After initial inspection, 44 were examined in detail via X-ray CT imaging to check for more subtle flaws and to assess the staining. The sample identified internally as 'Z0720-07m' was selected as having the best quality.

Hot-knife cutting

As the *Drosophila* CNS is too large to image by eFIB-SEM as a contiguous block, we cut it into 20 μm-thick slabs via our "hot-knife" sectioning procedure[159] (Figure S8A). The VNC was sectioned first into a total of 31 slabs using cuts along transverse planes. The brain was then sectioned into 35 slabs with sagittal cuts (orthogonal to those in the VNC). Quality of each slab was assessed by LM, followed by mounting, laser-trimming, and further inspection by X-ray CT.

EM Volume Imaging

As explained in Nern et al.,[39] we followed the imaging methods first described in Takemura et al.[34] with minimal modifications. We employed a fleet of seven customized eFIB-SEM machines to separately image each of the 66 hot-knife slabs over the course of a year. SEM images were acquired at isotropic 8 nm in-plane resolution at 3 MHz using a 3 nA beam with 1.2 kV landing energy. FIB milling was performed with a nominal 8 nm step size using a 15 nA 30 kV Ga ion beam. The final 160 teravoxels (including fixative) occupied 0.082 mm^3 total volume of which 0.054 mm^3 contains tissue.

EM Volume Alignment

As the brain and VNC volumes of our sample were imaged and hot-knife sectioned separately, we first assembled and stitched the hot-knife slabs of each volume independently, following the methods described in Nern et al.[39]

Following a single cut through the neck that separated the sample into brain and VNC, the hot-knife sectionings of the brain and the VNC were performed orthogonally to each other (Figure S8A). Hot-knife sectioning fixes the two in-plane imaging axes, leaving the rotation around the milling axis as a free variable.

For convenient viewing and analysis, we chose to orient the brain volume such that all three of its anatomical axes approximately coincide with the volume coordinate axes. The faces of each hot-knife slab are sagittal sections, with the sagittal axis coinciding with the X axis of our aligned volume. We rotated the brain around the sagittal axis, tilting the head back by 18 degrees to align its dorsal-ventral axis with the Y axis of the volume and its anterior-posterior axis with the Z axis. In the VNC, the hot-knife cuts are transverse sections, with the Z axis reasonably aligned to the sample's anterior-posterior axis.

We then proceeded to stitch together the brain and VNC volumes at their interface in the neck connective (Figures S8B–S8D). The cut through the neck spanned four hot-knife slabs of the brain volume on the anterior side, whereas it formed the first slab surface of the VNC volume on the posterior side. To extract the cut surface in the brain volume, we adjusted our hot-knife surface finding code and mostly relied on the BigDataViewer-based interactive tool to manually define the heightfield describing the exact location of the surface in the brain volume. An angle difference of ∼25 degrees remained between the surfaces. To match both volumes seamlessly, we developed code that applied a single non-rigid transformation consisting of the surface deformation field, the surface heightfield (including the ∼25 degree rotation), and a global translation. The software reduces the magnitude of the transformation as a function of distance from the stitching plane to ensure a smooth transition that is limited to the neck region, since proofreading had already started in the brain volume. After interactively confirming the correctness of this complex transformation on the two large VNC and brain volumes in BigDataViewer, we joined both volumes into a single, seamless volume of the entire CNS.

EM Volume Segmentation

Segmentation for neurons and semantic masks (nuclei, glia, etc.) was performed with the same methods as the MANC VNC volume,[34] with some differences for this sample as described in Nern et al.[39] Because the complete CNS volume was imaged and aligned as three separate subvolumes to be stitched together (right hemisphere, left hemisphere, and nerve cord), the segmentation procedure was run three times. For the nerve cord portion, a separate semantic segmentation model was trained to properly differentiate between muscle tissue and the nerve cord. Stitching the main segmentation for the left hemisphere onto the right hemisphere (and the VNC onto the brain) required care, as the earlier portion had already undergone significant manual proofreading by then. The segmentation region for each subsequent subvolume was constructed to overlap with that of the preceding subvolume. In the unified agglomeration, merges across the stitching boundary were selected according to the highest count of shared voxels among agglomerated segments within the overlapping region. Separation constraints to forbid merges between nuclei and fibers in the same nerve bundle (or the cervical fiber bundle) helped to avoid introducing false merges in already proofread segments.

EM Volume Synapse Identification

We performed synapse prediction by extending the methods as described in the optic lobe reconstruction.[39] Two separate networks for presynaptic T-bar detection and postsynaptic partner detection from that reconstruction were further fine-tuned with additional training ground-truth synapse data collected in the brain and VNC regions of the full CNS sample.

As with the previous reconstruction, we collected separate validation ground-truth to assess the performance of the synapse identification. In total, synapses were densely labeled in 114 cubes of 300 × 300 × 300 voxels, spanning 81 ROIs. Cube locations were selected to cover distinct ROIs, and randomly selected within a given ROI. Altogether, the subvolumes contained 2,303 annotated T-bars and 16,870 annotated postsynaptic partners.

By selecting validation cubes that span many ROIs, we sought to better assess global synapse prediction accuracy, as well as identify any potential problematic ROIs. In our case, initially selected validation cubes in the lamina (LA) showed poor recall in the set of synapse predictions. This recall issue resulted from some presynapses in the lamina having a differing morphology, which

was not well-represented in the original training set. We subsequently used these annotated lamina cubes to fine-tune a new T-bar detector, which we applied to the lamina ROIs, adding any predictions made by the new detector that did not already exist in our original set. (New validation cubes were then sampled and annotated for the lamina.)

Figure S8E gives the overall precision-recall plots for T-bars alone and synapses as units (both components correctly predicted); performance is comparable to the optic lobe subset. Figure S1I gives the precision/recall for each ROI, for T-bars alone, and for synapses. Source data for the plots are provided in the accompanying github.com/flyconnectome/2025malecns repository. Circle area is proportional to ROI volume, and color indicates ROI location, with red used for brain ROIs and blue for VNC ROIs. There is some variation in accuracy across ROIs, but performance is largely clustered, and generally above 0.8 recall for T-bars alone and 0.7 recall for synapses.

Neurotransmitter prediction

Ground Truth

The ground truth for neurotransmitter prediction is made up of data from the literature, as well as experiments run at Janelia, and is available as a regularly updated resource on GitHub.[160] This resource maps cell types to the emission of ten neurotransmitters: acetylcholine, dopamine, GABA, glutamate, glycine, histamine, nitric oxide, octopamine, serotonin, tyramine. The data is kept in ternary form for each neurotransmitter, a value of -1 signifying an absence, a value of +1 signifying a presence, and a value of 0 signifying that the neurotransmitter was not tested for. The specific subset of cell types used to train our model can be found in the *gt_sources* directory of that repo.

The cell types from the resource were matched to male CNS cell types according to the *flywireType* and *mancType* neuprint columns, taking synonyms into account from FAFB/FlyWire. We then filtered the ground truth to exclude entries with an evidence confidence rating below 3, removed instances of co-transmission (multiple +1 values when pooled across studies of the same cell type) and dropped any cell types for which positive and negative evidence exists for the same neurotransmitter. Disjoint training and validation datasets of cells were created (80% and 20% of the neurons, respectively), stratified so that they held a similar distribution of neurons from each class. The automatically detected T-bar locations for each cell were listed, and we verified that the split (80/20) was still valid at the synapse-level.

Model training

We trained an image classifier network following Eckstein et al.[41] to predict neurotransmitter identity of a pre-synapse from a region of interest centered around a T-Bar, and spanning 640 nm^3. The network outputs a normalized score for each of the 7 neurotransmitters considered: the scores add up to 1, and are akin to a probability. The highest number is chosen as the predicted neurotransmitter.

The classifier network is a ResNet50[161] model. It was trained using stochastic gradient descent on 100,000 mini-batches of 32 volumes each. All input volumes were intensity-normalized to the range $[-1,1]$. The data was randomly augmented during training with random axis flipping; affine transformations with rotations up to $\pm\pi$ radians, shear up to ± 0.1, translations up to ± 10 voxels, and scaling within $\pm 10\%$; intensity scaling by $\pm 20\%$ with fixed mean; intensity shifts up to ± 0.2; Gaussian noise with mean 0 and standard deviation 0.1; and Gaussian smoothing with sigmas randomly sampled between 0.1 and 0.5 along each spatial axis. We used the AdamW optimizer with a learning rate of 1×10^{-4} and parameters β=(0.9,0.999), λ=0.01, where β corresponds to the momentum parameters and λ to the rate of weight decay. Code for training and inference is at https://github.com/funkelab/synister_malecns.

Assignment of neurotransmitter predictions

Each segment was assigned an aggregate neurotransmitter prediction according to the scheme described in Nern et al.[39] Accompanying the predictions we provide a confidence score for each segment's assigned prediction according to the formula in Eckstein et al.[41] Each presynapse in a segment is assigned a confusion score by selecting an entry from the synapse-level confusion matrix: the row is determined by the owning segment's overall prediction and the column determined by the presynapse's model prediction. The segment confidence score is defined as the mean of its presynapse confusion scores.

The database records the most frequent prediction among a neuron's presynapses in the *predictedNt* property, except for those marked *unclear* as noted below. The most frequent presynapse prediction when pooled across all cells of a common type is recorded in *celltypePredictedNt*, except for those marked unclear. The confidence score accompanying predictedNt is given in *predictedNtConfidence*, and the confidence accompanying *celltypePredictedNt* is given in *celltypePredictedNtConfidence*.

Neurons or fragments with fewer than 50 presynaptic sites or those whose *predictedNtConfidence* is below 0.5 are given a *predictedNt* of *unclear*. Similarly, cell types with fewer than 100 presynapses when pooled across all corresponding neurons or cell types whose *celltypePredictedNtConfidence* is below 0.5 are given a *celltypePredictedNt* of *unclear*.

Finally, the *consensusNt* property is a copy of *celltypePredictedNt*, except in cases where experimental ground truth for the cell type is available to override the model prediction. Additionally, all octopamine and serotonin results are set to *unclear* in *consensusNt*, owing to the relatively scant validation data used for those neurotransmitters. The *consensusNt* is the recommended property to use in most analyses.

EM Volume Proofreading

We carried out intensive manual and semi-automated proofreading, quality control, annotation and analysis targeting all neurons in the image volume to produce a connectome that can be considered finished and fully annotated[29–31,33,34] (as compared with draft

connectomes that are automatically segmented and partially proofread[32,162] or partially traced[43,142]) by the emerging standards of the field.

As detailed below, we inspected every neuron for false merges and repaired them as necessary. All significant branches and backbones from the automated segmentation were inspected and we attempted to merge them onto the appropriate neuron. We traced the cell body fiber from every soma to its cognate neuron, except when data artifacts prevented it. Neurons that could not be typed or matched by morphology and connectivity across datasets or hemispheres were reinspected. As an additional quality check in the central brain and right optic lobe, we compared neurons with their homologues from the opposite hemisphere or other optic lobe columns. Thus, to the best of our ability, the main segment of each neuron has been identified as such and is free of major errors that would preclude cell typing. In aggregate, the segments identified as neurons (as opposed to fragments) capture a fraction of all synapses in the volume that is comparable to prior connectomes which cover subsets of the CNS (hemibrain, FAFB/FlyWire, MANC).

We did not proofread individual synapses. We did revise our synapse prediction model using additional ground truth when it was found to have suboptimal performance in specific compartments. Overall and per-compartment synapse prediction accuracy is shown in Figures S8E and S1I, respectively.

After proofreading, the neuron segmentation and synaptic connections jointly define a connectome graph containing 25.58M edges between 166,483 neurons with a superclass annotation. Considering only connections with a strength of at least 5 synapses (a threshold sometimes used to remove weak connections), the remaining graph contains 6.24M edges between 165,536 neurons. A notebook to quantify the number of neurons in the dataset and the total number of neuron connections is provided in the accompanying github.com/flyconnectome/2025malecns repository.

Major phases of proofreading

Current state-of-the-art automated neuropil segmentation methods leave many unresolved errors requiring manual proofreading to identify and correct. The segmentation was proofread over 3 years by 29 expert proofreaders (estimated effort of 44 person-years). We executed a combination of bottom-up and top-down proofreading protocols using a software toolchain for connectomic reconstruction including NeuTu,[163] Neu3,[164] and DVID[165] (Figure S8F). Further descriptions and rationale are provided in Nern et al.[39] As the image volume was assembled in three major phases (right hemisphere, left hemisphere, and nerve cord), we repeated all major protocols in our proofreading process for each subvolume as it became available.

The first phase was cell-body fiber linking, in which we attached orphaned cell bodies (somata) to their main axons. Next, we followed our cleaving protocol in order to eliminate major false merges in all segments deemed significant according to their synaptic counts or other qualities, such as passing through the cervical fiber bundle.

With the dataset largely free of major false merges, we could begin efficiently assembling fragments together into recognizable cell shapes. In the backbone tracing protocol, we targeted synapse-rich segments for coarse tracing until no obvious false splits remained on large branches.

To increase the fraction of synapses captured by our traced backbones, we executed two bottom-up protocols aimed at connecting medium or small fragments to their target neurons. The focused merging protocol provided automatically selected merge proposals for directly adjacent segments to proofreaders as binary decisions. The orphan linking protocol tasked proofreaders with tracing a fragment to a backbone segment (without knowing which target it is destined for). We attempted to trace every fragment with 100 or more synaptic connections throughout the dataset. In the central brain and right optic lobe we went further, examining fragments with at least 50 synaptic connections.

The final phase of proofreading is purely top-down: neurons are assessed holistically to spot overlooked false merges or false splits. In this reconstruction of an entire CNS, we often had the benefit of examining pairs or groups of homologous neurons in tandem to spot gross inconsistencies between cells of the same type. This protocol was executed primarily by proofreaders in the central brain and right optic lobe, whereas we relied on the cell typing process to flag errors in the left optic lobe and VNC.

In addition to our major proofreading protocols, expert neuroanatomists from both Cambridge and Janelia examined all neurons as they typed and annotated them, providing a final quality check as poorly reconstructed neurons cannot be easily clustered and typed.

Our proofreading team was staffed almost entirely by annotators with experience from earlier connectomic reconstructions. Newly hired proofreaders received at least six weeks of training using a separate database before transitioning to the production environment. Regular "refresher" training was given to all proofreaders when we transitioned between major phases of proofreading. Two senior proofreaders took on a specialized role to provide oversight and quality control, reviewing the work of other proofreaders in addition to performing their own proofreading tasks. Based on an analysis of our edit logs and task management records, we estimate that our proofreading team spent approximately 44 person-years on the CNS dataset.

We proofread all fragments from the initial segmentation with > 100 synaptic connections. 98.9% of the 141,780 detected neuron-associated nuclei are part of a proofread neuron. After proofreading, only 0.6% of neurons with attached soma are composed entirely of fragments below this threshold. Thus, for the 1.1% of nuclei which remain unassociated with proofread arbours, we estimate that > 99% of the corresponding neurons have been proofread but have not been connected to their cognate nucleus in the cell body rind on the outside of the brain. For sensory neurons (without a cell body in the dataset), we seeded and traced axon profiles in all nerves entering the volume.

Excluding automated/scripted edits, we performed 4,117,544 merges, 147,212 cleaves (splits along supervoxel boundaries), and 6,046 supervoxel splits.

AutoProof

As described in the previous section, significant effort is spent manually proofreading the automated segmentation, and this process constitutes the most labor intensive component in generating a connectome reconstruction. With the accuracy of current automated segmentation methods, proofreading the entire segmentation is intractable. Manual effort is instead spent to target a specific connectivity coverage (see previous section). This workflow leaves a certain amount of the segmentation unexamined; within the orphan linking protocol, disconnected orphan fragments are only examined if they are above a threshold for synaptic weight.

We developed a new procedure, AutoProof, to automatically process these unexamined fragments and select a subset that can be joined to target neurons with high confidence. A machine learning model is first trained on the manual proofreading decisions from the focused merge protocol, thereby learning, given a pair of adjacent segments, whether the segments belong to the same body or not. This model is then applied to all unexamined orphan fragments in the central brain and nerve cord with a synaptic weight of ten or higher. The full details of AutoProof are given in Huang et al.[166]

A random sample of orphan-to-target merges proposed by AutoProof was manually verified, and used to select a highly conservative threshold, targeting a low estimated error rate of ~3%. All proposed merges above this threshold were automatically accepted without explicit human verification; the risk is in part mitigated as any given orphan is of small synaptic weight and therefore individual errors would have minimal impact on the overall connectivity.

For the male CNS reconstruction, AutoProof helped the completion rate significantly. About 200k orphan link proposals were automatically accepted, adding about 2.4M postsynaptic densities (PSDs) and 309k T-bars. These synapses added about 1.3% to the connectivity completion rate. At an estimated 200 tasks per day for a human annotator working in the orphan link protocol, this automated procedure was equivalent to about 4 person-years of work.

Quality metrics

The quality/completeness of a connectome can be assessed using a variety of metrics. First, we proofread all fragments from the initial segmentation with >100 synaptic connections. Second, 98.9% of the 141,780 detected neuron-associated nuclei are part of a proofread neuron; of the remaining 1.1% we estimate that >99% were proofread by the first strategy. Third, the resulting neuron counts match those reported for existing brain and VNC connectomes (Figure 1E). A small number of cells could not be reconstructed due to sample artifacts on the edge of the volume (e.g. some R1-6 photoreceptor neurons in the laminae) or segmentation issues (some sensory and motor neurons).

Another important quality metric is the overall fraction of presynapses and postsynapses which have been captured by 'traced' neurons, known as presynaptic and postsynaptic 'completeness'. As can be seen in Figure S8G, presynaptic completeness tends to be much higher than postsynaptic completeness, as presynapses typically reside on larger-calibre neurites which are more easily merged via both automated segmentation and manual proofreading. This trend is also observed in prior large-scale *Drosophila* connectomes.[29,31,34]

A synaptic connection is only useful to downstream analyses if both its presynapse and postsynapse belong to traced neurons, so a more informative metric is the connection completeness, i.e. the fraction of synaptic pre-to-post connections in which the neurons on both sides have been traced. Figure 1D shows the fraction of completed connections in each neuropil, with an overall average of 40.1%. Empirically, connection completeness is approximately equivalent to the product of presynaptic completeness and postsynaptic completeness.

However, not all neurons in a compartment are equally well traced. An informative neuron-centric metric is the 'downstream capture' of each neuron, which is defined as the fraction of synaptic outputs which connect to traced neurons. Even when a neuron is itself completely reconstructed, if its postsynaptic partners are poorly reconstructed then its connectivity to downstream neurons will be poorly characterized. The discrepancy between compartment-level completeness and neuron-level connection recall is revealed by the downstream capture metric. The distribution of downstream capture fractions among neurons in the major compartments of the CNS is shown in Figure S8H.

It is worth noting that the downstream capture distribution for the central brain is bimodal. The second peak is chiefly due to populations of neurons whose outputs are in areas with relatively high postsynaptic completeness: the EB, FB, and NO in the central complex; the antennal lobes; and all compartments of the mushroom bodies.

Another quality metric is the number of unmerged 'orphan' fragments in the dataset and their distribution of synapse counts. The largest of these orphans remain unmerged in our dataset due to data artifacts or especially complex morphologies which make it difficult or impossible to find the site at which they should be traced to a neuron. We inspected and attempted to eliminate all orphan fragments with 100 or more synaptic partners. There are 5,207 remaining orphan fragments at or above that threshold in the proofread dataset. In total, there are 84.6 million orphan fragments in the dataset, most of which contain very few synapses. The final distribution is shown in Figure S8I.

Spatial Transforms

We generated spatial transforms to register the male CNS to other coordinate spaces, including the JRC2018M brain light microscopy template[75] (procedure described in Nern et al.[39]), and the MANC, FAFB/FlyWire and hemibrain connectome datasets. In all cases, we began with an automated registration between synapse point clouds using either Elastix[167] or CMTK (RRID:SCR_002234) to produce a non-linear transform. Where necessary, we fine-tuned the transform using BigWarp[168] in ImageJ/Fiji by manually adjusting pairs of corresponding landmarks. In addition to these bridging transforms, we also generated a transform to mirror the male CNS

across the midline which aligns homologous neurons from the left hemisphere to the right or *vice versa*. All transforms are accessible with *navis-flybrains* (see key resources table) and can be chained with existing transforms to map to additional coordinate spaces, such as JRC2018 unisex brain, the JRC2018 unisex VNC, etc., using *navis*. Template-to-template transformation fields can be obtained from https://www.janelia.org/open-science/jrc-2018-brain-templates.

Defining anatomical regions in the EM volume

As described in Nern et al.,[39] the primary neuropil regions were initialized via transfer from the JRC2018M template[75] using the synapse point cloud to register the volume. We then refined the boundaries of those regions which did not align cleanly to the underlying EM data or relevant populations of segmented neurons.

Analysis Software

Data curation and analysis was carried out with a combination of free and open source software tools for R and Python, principally from the *natverse* (https://natverse.org/) and *navis* (https://navis-org.github.io/navis/) ecosystems developed in Cambridge. For details, see the key resources table.

Annotations

Each neuron in the dataset was given a set of annotations for various anatomical, developmental and descriptive features. We highlight some of the main ones below.

Superclass

Superclasses describe broad sets of neurons, grouped together by anatomy or general function. Bodies in the dataset are defined as neurons if they have a superclass. Bodies without one are fragments of neurons. We define 20 superclasses: intrinsic neurons are those contained entirely within the optic lobes, central brain or VNC; visual projection neurons connect the optic lobes and the central brain while visual centrifugal neurons do the opposite; sensory neurons extend their axons from the periphery into the CNS; sensory ascending or sensory descending neurons are sensory neurons that extend from the VNC into the brain or from the brain to the VNC, respectively; ascending neurons have their somas in the VNC and extend into the brain while descending neurons do the opposite.

Motor neurons extend their axons out of the CNS to connect to muscle; efferent neurons are non-motor efferents that can be found entirely contained in the central brain or VNC or connecting these two regions (descending or ascending); finally endocrine neurons connect the central brain to the corpora allata or cardiaca endocrine glands.

Superclasses that are found across the CNS, such as intrinsic and sensory, are given a prefix to distinguish between the populations in the optic lobe (ol-), central brain (cb-) and VNC (vnc-).

Hemilineage

Hemilineage annotations were transferred from the FAFB/FlyWire,[29,30] hemibrain,[31] and MANC[33,34] datasets according to cross-matched neuron types. Unmatched types and many:1 matches were reviewed as described in Schlegel et al.[30] Various hemilineage naming systems are used in the existing literature: Ito/Lee,[65,66] Hartenstein,[169,170] and Truman.[171] These nomenclatures represent a partially overlapping population, but some hemilineages are described in one but not the others: for example, the Truman nomenclature uniquely covers a large proportion of VNC neurons. Male CNS metadata contains Ito/Lee and Truman lineage names, but a mapping between Ito/Lee and Hartenstein nomenclatures is provided in previous work.[30] A subset of Truman hemilineages in the brain was annotated as putatively serially homologous to those in the VNC; details will follow in a companion study (Marin et al.,[33] in prep.).

Supertype

Supertypes were assigned on a per hemilineage basis to morphologically similar neurons in the central brain using morphological (NBLAST) clustering[30,42] and subsequent visual inspection. Neurons were grouped into a supertype if their main arbours aligned and if dendrites and axons were mostly overlapping in 3D space.

In some cases, as with the SLPal2 hemilineage, sex-specific terminal cell types can be linked together through their supertype designation. For example, supertype ''12551'' includes a group of sex-specific neurons previously described as the sexually dimorphic aSP-g[27,56] or aSP6[58] cluster. While these neurons differ widely in morphology and connectivity, preventing them from being linked at the level of terminal cell types, their classification under a common supertype reflects a shared development underpinning sex-specific functions within their respective neural circuits.[21,27,172]

Dimorphism

Dimorphism annotations were added to neurons on a per cell type basis according to a set of operational definitions used to describe three categories (1), isomorphic, (2) sexually dimorphic, and (3) sex-specific. Neurons from the FAFB/FlyWire, hemibrain (where possible), and male CNS datasets were clustered based on morphological (NBLAST) and connectivity (cosine similarity) metrics, and visualized with a dendrogram (Ward's method) or a low-dimensional embedding (UMAP) (see also Figures S3A–S3D). Isomorphic neurons were matched across hemispheres and datasets, while sex-specific neurons were defined as having no probable match across opposite-sex datasets despite bilateral consistency within sex. Sexually dimorphic neurons were annotated when neurons could be associated closely enough such that they were clearly arising from the same cell type, but demonstrated consistent numerical and/or morphological differences across sexes despite their shared developmental history. As a point of reference: at the level of individual neurons, the average dimorphic branch is 266 μm in length, with the smallest branch being just over 13 μm.

However, this represents an outlier and since we annotated dimorphism on a per-type basis, the better approach is to aggregate per type. With this, the average dimorphic branch length is 386 μm with a minimum branch length of 78 μm per dimorphic cell type (Figures S3R and S3S). In a few cases (particularly in sensory neurons, including DA1 ORNs and taste peg GRNs), large differences in cell number represent possible candidates for sexual dimorphism. However, our sample size of *n*=2 brains precludes formal statistical analysis, so we did not label these cells as dimorphic. In some developmental lineages (e.g. FLAa3), high morphological similarity between types obscured our type-to-type matches. In many cases, types that fall into this category are considered ''sex-specific'', but integration of future datasets may enable stronger type matching and these cells could turn out to instead be sexually dimorphic. Due to the lack of a fully annotated female VNC connectome, our dimorphism annotations are focused on the central brain and optic lobes. While we were able to add some additional dimorphism annotations for ascending neurons with extensive arbours in the brain, the majority of dimorphism annotations in the VNC come from existing literature.[57,62]

We offer a basic confidence assessment for our dimorphism annotations: dimorphic neurons are labeled either ''sexually dimorphic'' or ''potentially sexually dimorphic'', and sex-specific neurons are labeled ''male-specific'' or ''potentially male-specific''. We consider types with the qualifier ''potentially'' as lower-confidence annotations. However, analyses of dimorphism throughout the paper consider all dimorphism labels regardless of their confidence.

fruitless *and* doublesex

Neurons in EM data were annotated as putatively expressing *fruitless* and/or *doublesex* according to comparison with light microscopy data transformed and projected into a registered template space.[75,153] Our analysis focuses on the central brain but we did annotate a small number of *fruitless* and *doublesex*-expressing neurons in the VNC based primarily on previous annotations from the MANC dataset.[57,146] The light level image data were obtained from Virtual Fly Brain.[173] Original data were sourced from Cachero et al.[56] and Chiang et al.[70] for *fruitless*, and Nojima et al.[28] for *doublesex*. EM neurons were chosen for inspection against light data based on hemilineage assignment, since each light-level image was generated from individual lineages, or 'clones'.[70,174]

EM neurons were compared to light images based on overlap in three-dimensional space and scored as 'high', 'low', or 'NA', indicating the amount of overlap with the clone and/or other evidence of gene expression according to previously published immunohistochemistry or transcriptome data, including Allen et al.[147] Hemilineages were putatively assigned to clones according to Costa et al.[175] Annotations were further reviewed to ensure that neurons with the same cell type received the same annotation except in exceptional circumstances. Of all hemilineages with any *fru*- or *dsx*-expressing neurons, 15 contain only high-confidence annotations (e.g. ALlv1, CREa1_ventral, DL2_ventral, VPNd2, and SLPal1). Twenty-five hemilineages have at least 75% high confidence annotations, and 40 have at least 50% high-confidence annotations. Hemilineages in the GNG and central complex have the fewest high-confidence annotations, with 27 hemilineages containing no high-confidence annotations at all.

As a complementary strategy to identify *fru*- and *dsx*-expressing neurons within a given hemilineage, we performed NBLAST similarity scoring between registered light-level clone images and individual neurons reconstructed from electron microscopy (EM) connectome data. For each clone, the raw NRRD image was loaded and binarised at multiple intensity thresholds (10%, 50%, 100% of the non-zero intensity distribution) to assess sensitivity to thresholding. Each threshold image was converted to a dotprops representation (k=20 nearest neighbors, resampled at 1 μm). Skeletons for EM neurons were retrieved from neuPrint (male-cns:v1.0) for male and CAVE (FAFB v783) for female datasets and filtered according to hemilineage identity. Neurons were pruned to their primary backbone using Strahler ordering, then mirrored onto the left hemisphere. Neurons were converted to dotprops (k = 5 nearest neighbors, resampled at 1 μm). For female neurons, skeletons were first transformed from FAFB14 to male CNS template space. NBLAST was performed using version 2 scoring with normalisation, producing a per-neuron similarity score against clone images. Scores were annotated with the pre-existing manual *fru*/*dsx* annotations from metadata, and distributions were compared across expression categories and thresholds using median summary statistics. High-scoring neurons without a label and low-scoring neurons with a label were then manually reviewed. This review resulted in the addition or correction of 397 body IDs.

To validate the *fru*/*dsx* annotations, we compared our observed values to those expected from previous studies.[28,56,63] Considering only the brain lineages observed in Cachero et al.,[56] we identify 3,106 *fru*+ neurons in males and 2,042 *fru*+ neurons in females, compared to the expected 1,993.6 (±75.7) and 1,668.4 (±60.6), respectively. For *dsx*+ lineages reported in Nojima et al.,[28] we find 341 *dsx*+ cells in males and 128 in females, compared to 387.4 (±18.6) and 66 (±4.4) expected neurons (Figure S3L). Breaking this down per lineage shows that much of the discrepancy stems from lineages where prolific cell types have common morphologies, and this is consistent across sexes (Figure S3I). It is difficult to discern whether our labels are too inclusive, or whether methodological limitations in prior studies resulted in an underestimate. If the former is true, cell types with similar morphology may not always collectively express *fru* or *dsx*. For FAFB/FlyWire, our estimates for *fru*- and *dsx*-expressing neurons exceed those from a recent study in the same dataset.[137] Our inclusive labeling strategy, as well as our incorporation of light-level data from multiple datasets, may be responsible for this discrepancy.

Limitations due to lack of hemilineage assignment, ambiguity in lineage/cell type delineation, and technical limitations imposed by the genetic labeling prevented annotation for certain groups of cells. Specifically, MARCM clone data are missing most primary neurons, and *fruitless* and *doublesex* expression in the optic lobes where most neurons have a different pattern of neurogenesis has not yet been well-characterized. Finally, we excluded expression in mushroom body Kenyon cells where the subpopulation expressing *fruitless* cannot be clearly delineated.

Synonyms

The synonyms column was filled for EM neurons which could be matched to previously published literature, especially when more than one name is used to describe the same cell. For putatively *fruitless*- and *doublesex*-expressing neurons, the name of the matching light-level clone[56,58,70] was added to neurons according to lineage[175] after manual visual assessment.

Updated FlyWire annotations

In the process of adding annotations to the male CNS, we also added new (*fru_dsx* for *fruitless* and *doublesex* expression; *dimorphism* and *matching_notes* for dimorphic neurons; supertype matching the same field in neuPrint) and revised existing annotations for FAFB/FlyWire. The latter mostly affected *cell_type* and *hemibrain_type* but we also made minor adjustments to *super_class*, *ito_lee_hemilineage* and *side*. To reconcile cell types for optic lobe-intrinsic neurons, we also integrated the cell types from Matsliah et al.[74] with our original annotations. These updated annotations have been deposited at https://github.com/flyconnectome/flywire_annotations.

Typing in the central brain and the ventral nerve cord

Neurons were principally typed by cross-matching to the FAFB/FlyWire[29,30,74] (v783), the hemibrain[31] (v1.2.1) and the male adult nerve cord (MANC, v1.2.3).[33,34] The initial typing was principally morphology-based (NBLAST) and generated a pool of cross-matched types for uniquely identifiable, often large neurons such as MBONs, uniglomerular olfactory projection neurons, or peptidergic neurons. This provided a scaffold on which to compute connectivity-based similarities between neurons from the different datasets. The connectivity-based approach was often required to make matches at the level of terminal cell types. In order to accelerate running a neuron matching pipeline, we developed R and Python tools to generate and efficiently review large-scale clusterings (see *coconatfly*, *cocoa* and *bigclust* in key resources table and sections below for details). Connectivity and skeletons (NBLAST) for the male CNS, MANC and the hemibrain were obtained from neuPrint. For FlyWire, we used the same L2-based skeletons as in Schlegel et al.[30] For connectivity, we used the new "Princeton" FlyWire synapse predictions[152] (materialization version 783) available from https://codex.flywire.ai.

The above matching pipeline was run iteratively: cell type labels were added/refined and then used to update the connectivity similarities. While the terminal cell typing was primarily connectivity-based, we frequently used NBLAST to cross-check labels. Matches to each of the other datasets are recorded in a set of fields in neuPrint: *hemibrainType*, *flywireType*, *mancType* and *mancGroup*. For cases when male CNS neurons match multiple types in other datasets, the types are shown separated by a comma. The field *matchingNotes* includes, when necessary, relevant information for the cross-matching or typing. The primary *type* annotation represents the consensus type across all matched types. In a small number of cases, we modified existing types by defining a finer resolution subtype, merging two or more types, renaming the type or creating new types. For example, some of the tentative *CBXXXX* types introduced in FAFB/FlyWire were given new names following the hemibrain convention of *{main input region}{number}*. New male-specific types also follow this convention with an additional '*m*' suffix, e.g. "*SIP136m*". Please see also the section below for details on retyping of mechanosensory Johnston's organ (JO) neurons.

The *group* field was used to record candidate matches early in the annotation process but retained later on as a more granular label than type. For the VNC, serially homologous neurons may have the same type but different groups in different neuromeres. In other cases, we think that differences between neurons with a different *group* but the same *type* may be the result of natural variation and not stereotypical differences observed across individuals. The field *instance* merges together *type* and *somaSide* or *rootSide* for sensory neurons.

Optic lobe typing

Cell typing for the left optic lobe largely followed the methods described in Nern et al.,[39] combining morphological similarity with connectivity. Extensive comparisons were made to the typed cells of the right side, greatly accelerating the process compared to the previous *de novo* cell typing effort. For Figure S4 and Data S1 we retain the cell type groups introduced in Nern et al.[39]: optic neuropil intrinsic neurons (ONINs), optic neuropil connecting neurons (ONCNs), visual projection neurons (VPNs) and visual centrifugal neurons (VCNs). We note that Figure 4 combines ONINs and ONCNs into one group OLINs. We are omitting the category of cell types grouped as "other" in Nern et al.[39] in Figure S4 and Data S1, as these cells are central brain neurons with minor optic lobe connectivity, and in many cases, while present in both hemispheres, do not have synapses in both optic lobes. The latter difference may be due to natural variability or reflect differences in precise boundaries of neuropil ROIs between hemispheres. The new, complete dataset provides a more complete description of the connectivity and brain region innervation of optic lobe associated cell types with synapses outside the (right) optic lobe. We found that three previously assigned[39] optic lobe cell types were present in only one hemisphere (or, in one case, only had a marginal match between the candidate cell on each side) and appear to be also absent from other datasets. These cases may represent aberrant cells of unknown type rather than well-defined types.

Unmatched neurons

We cross-matched 96.1% of central brain and 99.7% of optic lobe neurons to FAFB/FlyWire and/or hemibrain datasets, and 93.1% of VNC neurons to MANC (Figure 1H). We were unable to match a fraction of efferent (17%) and sensory (15%) neurons in the VNC due to limitations in data quality and intrinsic variability which was not well-captured in cell typing in previous datasets. In addition, while ascending neurons could be confidently matched between male CNS and the previous MANC nerve cord connectome, around one third of these neurons could not be matched with the FAFB/FlyWire brain connectome since their arbours in the brain are too small for confident matching. Similar issues prevented confident matching of 29% of sensory ascending neurons that project from VNC to brain with the MANC dataset – reliable identification requires analysis of both brain and VNC.

JO retyping

In FlyWire[30] and MaleCNS v0.9, types for mechanosensory Johnston's organ (JO) neurons had been carried forward from Kim et al.[106] for JO-A/B and Hampel et al.[104] for JO-C/D/E/F/mz. Types in both these publications were principally based on morphological features from manual (pre-FlyWire) neuronal reconstructions of just one hemisphere of the FAFB electron microscopy image dataset.[43] Here, we combine data from four connectome hemispheres (FAFB/FlyWire left/right + MaleCNS left/right) and apply the same pipeline used for cross-matching to generate across-dataset types for JO neurons in both FlyWire and MaleCNS v1.0.

For JO-A and JO-B we split the previous coarse types into a number of smaller terminal types: *JO-A1* through *4* and *JO-B1* through *4* (connectivity subtypes are indicated by *_a*, *_b*, and *_c* suffixes). For JO-C/D/E/F/mz, which had been subtyped very finely, we adjusted some cell type boundaries. Where possible, we reused existing nomenclature: for example, the "new" *JO-FV* type corresponds ~90% to the original *JO-FV*. For types less correlated to any of the original types, we tried to stay close to the original nomenclature: for example, the new *JO-EV1* through *6* largely correspond to the original *JO-EV** (*JO-EVM*, *JO-EVL*, *JO-EVP,* etc.) types.

Due to segmentation issues in JO neurons (in particular on the right-hand side of the Male CNS) a number of neurons received the type *JO_unclear*. As a consequence, neuron counts for some types are imbalanced between hemispheres of the same dataset or across datasets (i.e. male versus female). We do not believe this to be a sign of sexual dimorphism.

Connectivity co-clustering

For terminal cell-typing and across-dataset matching of neurons we calculated a connectivity-based (cosine) similarity score. To efficiently run this pipeline on hundreds of thousands of neurons we developed various R and Python tools: *coconatfly* and *cocoa*, respectively (see key resources table). For a given population of neurons – e.g. central brain neurons in FlyWire and male CNS, or VNC-intrinsic neurons in MANC and male CNS – we generated an observation vector from a matrix where each row is a neuron and each column is an already cross-matched cell type. The values in that vector represent the number of synapses between a given neuron and the cross-matched cell type. We typically considered both the neurons' inputs and outputs to generate the vector, i.e. each cross-typed cell type has one column for connections to (inputs) and one column for connections from it (outputs). On a case-by-case basis, where neurons lack substantial connections on one side, we would also occasionally just consider the inputs or the outputs. For example, outputs alone were used when clustering sensory neurons, which have few or no upstream partners within the dataset, and inputs alone were used when clustering motor neurons, which have few or no downstream partners. Based on the connectivity vector we then computed pairwise cosine similarity, which is defined as the cosine of the angle between two vectors. Because this metric only considers direction and ignores magnitude, it automatically normalises for systematic differences in absolute edge weights between neurons from different datasets. The cosine similarities were converted to distances from which we calculated either linkages (using Ward's method) for visualization as dendrograms, or low-dimensional embeddings (UMAP) for visualisation as 2-dimensional scatter plots. See section below on the manual inspection of clustering results.

Connectivity data for the male CNS, MANC and the hemibrain were obtained from neuPrint. For FlyWire, we used the new FlyWire synapse predictions[152] at materialization version 783 available for download from https://codex.flywire.ai.

Morphological co-clustering

Morphological similarity scores were generated using NBLAST[42] as previously described.[30] In brief, we obtained neuron skeletons from either neuPrint (for male CNS, hemibrain and MANC) or via the L2 cache (FlyWire) and pruned twigs smaller than 5 μm. Male CNS, hemibrain and MANC skeletons were additionally downsampled to the average resolution of the L2 FlyWire skeletons (one node every 2.7 μm of cable). Depending on the NBLAST, we additionally either transformed skeletons into a common brain space and/or mirrored them onto the same side. From the processed skeletons we generated dotprop representations using the 5 nearest-neighbors (k=5) for each point to calculate the tangent vector. Dotprops were fed into the NBLAST function to compute both forward (neuron A → neuron B) and reverse (neuron B → neuron A) similarity scores. The final score was then calculated as the minimum between the forward and reverse scores. All relevant functions are implemented in *nat*, *neuprintr*, *fafbseg* (R) and *navis*, *neuprint-python*, *fafbseg-py*, *flybrains* (Python) (see key resources table). For inspection of the results, similarities were converted to distances from which we calculated either linkages (using Ward's method) for visualization as dendrograms, or low-dimensional embeddings (UMAP) for visualization as 2-dimensional scatter plots. See section below on the manual inspection of the results.

Inspection of clusterings

We developed various tools to efficiently inspect and integrate results of morphological or connectivity co-clusterings. For small-scale (10s to 100s of neurons) clusterings, we used functionality implemented in *coconatfly* (R) and *cocoa* (Python) to visualize similarities as dendrograms and/or heatmaps. For larger datasets, we developed *bigclust* (see key resources table) which enables interactive exploration of clusterings of 100,000s of neurons as either dendrograms or low-dimensional embedding (UMAP) with linked visualization of neuronal morphologies across datasets.

Sensorimotor information flow analysis

Long-range flow of information from sensory inputs to motor neurons was assessed via maximum flow analysis of the synaptic graph. Unlike analyses of indirect connectivity,[176,177] graph traversal,[67] or dynamics of indirect connectivity traversal (influence)[143] from only a source population of neurons, maximum flow can yield a distinct measure of information flow for each pairing of sensory source and

motor sink populations. This analysis is also suited to long-range information flow, since maximum flow values do not necessarily exponentially attenuate like most multiplicative indirect connectivity measures. However, a limitation of maximum flow is that it does not identify alternate routes with equal or slightly less total flow value, so negative inferences about information flow based on low maximum flow values must be made with caution. Note that information flow does not consider the sign of interactions, i.e. neurotransmitter predictions were not considered in this analysis.

Maximum flow was computed for each combination of sensory source modality class annotation and motor domain subclass annotation. Efferents, endocrine neurons, and other nervous system outputs were not included. Input-normalized synaptic connectivity was used as edge capacities. Pseudo-source and -sink nodes were added to the graph with unit capacity connections to all source and from all sink neurons, respectively. All other inputs to sources and outputs from sinks were ignored. Thus the upper bound of each potential maximum flow was the minimum of the number of source and sink neurons. Maximum flow was computed using Dinic's method[49] on a sparse graph representation,[178] with floating point edge capacities in [0, 1] discretized into integral capacities in [0, 10000] and flows renormalized to [0, 1] after computation.

These calculations defined a large ensemble of paths traversing the connectome graph from sensory to motor neurons; each path is characterized by a single maximum flow value. We computed a number of additional summary statistics from these values in order to summarise the extent to which interneurons within the connectome were specific to a sensory modality, a motor domain or a pairwise combination of a sensory modality and motor domain. Each statistic depends on identifying a subset of paths flowing through a given interneuron and comparing their max flow values with those for a larger ensemble of paths.

We computed flow preference scores for each sensory modality in turn by taking the mean flow of the paths for that modality traversing a given neuron and dividing it by the mean flow for all paths originating from that sensory modality. Likewise a preference score for motor domains for all neurons was computed as a mean over all flows from all sensory modality sources. Overall sensory or motor flow specificity for each neuron was computed as the maximum flow preference normalized by the sum preference for all sensory modality preferences and motor domain preferences, respectively. A corresponding combined sensorimotor specificity score was computed as the maximal flow value through a neuron normalized by the sum flow for all pairs of sensorimotor flows.

Due to the large number of abdominal motor neurons and their distance from most sensory neurons, flows targeting them often spread broadly over neck connective neurons and caused these neurons to have relatively high preference values for the abdominal domain. To aid motor domain preference analysis for this population, a separate maxflow analysis was performed with the same sensory and motor annotation categories, except with abdominal motor neurons partitioned into separate domains for each annotated neuromere. This flow was not used for any other purposes; all other mentions of the sensorimotor flow analysis refer to the version with a single abdominal motor domain.

Analysis and visualization of sequential relationships in flows was performed using a pseudo-layering order, where neurons are assigned a layer value preferring to be one greater than the layer value of their flow inputs, weighted by the input-normalized flow value. Since the flow graph is a directed and acyclic, these layer assignments for all neurons, $\overrightarrow{l}$, are computed using the (pseudo-)inverse of the Laplacian of the input-normalized flow adjacency matrix, F:

$$\left(\overrightarrow{l} + \overrightarrow{1}\right)F = \overrightarrow{l},$$

$$\overrightarrow{l} = -\overrightarrow{1}F(F - I)^{-1}.$$

The data for all sensorimotor flows are provided in the accompanying github.com/flyconnectome/2025malecns repository.

Sensorimotor clusters

For analysis of sensorimotor flow structure, descending and ascending neurons were clustered on the basis of a UMAP embedding of their sensorimotor flow. For clustering, the embedding was generated with 20 neighbors and a minimum distance of 0, using Euclidean distance. Clustering was performed on the mean sensorimotor flow aggregated by neuron type, projected into this embedding. Clustering was performed by simple k-means, with the number of clusters selected from a parameter sweep between [2, 60] maximizing the silhouette score. Cluster labels were reordered by clustering them via average agglomerative linkage of the cosine distance of their concatenated incoming and outgoing cluster connectivity.

Behavioral category compatibility of clusters was computed by multiplying the mean sensorimotor flow matrix of each cluster with a compatibility matrix for each behavioral category. Because the purpose was to demonstrate ease of interpretation of sensorimotor flow as it relates to putative function and behavioral hypotheses, rather than produce an optimal predictive algorithm, the compatibility matrices were manually constructed using simple rules of which sensorimotor pairings are likely predictive of compatibility with which behaviors. For those that are, those entries in the compatibility matrix are 1, while all others are 0. These pairing rules are as follows: for VNC sensation, any flow originating from gustatory, tactile, or proprioceptive modalities; for escape, any flow originating from vision targeting the legs or wings; for feeding, any flow originating from gustation or olfaction not targeting the abdominal domain, and any flow targeting the proboscis; for flight, any flow targeting the wings or halteres; for grooming, any flow originating from mechanosensory or tactile modalities targeting proboscis, neck, or front leg domains; for reproduction, any flow targeting the abdominal domain; for walking, any flow originating from any mechanosensory modality targeting leg domains. Both the

compatibility and flow matrices are L_1 normalized before multiplication. The receiver operating characteristic area under the curve is 0.83 when compatibility is treated as a multilabel classifier of described behavioral category.

The data for all sensorimotor clusters are provided in the accompanying github.com/flyconnectome/2025malecns repository.

Effective connectivity

In Figure S4J (Visual system) we used the Connectome Interpreter tool[179] to compute and visualise measures of effective connectivity (which can be computed for both direct and multi-hop pathways). We first found direct and two-hop paths from all visual projection neurons (VPN) to either descending neurons (DN) that are sexually dimorphic or sex-specific, or descending neurons for which there is existing research on the function of the cell type. We next filtered the paths for both male and female, such that all direct connections are stronger than 1% of the input of the postsynaptic cell type. We further selected from the filtered paths, ones that are unique to one sex, by removing paths that exist in the brain of the other sex, regardless of connection weight. We finally selected only the paths that contained at least one sexually dimorphic or sex-specific cell type.

We calculated the effective connectivity based on the selected paths: if the VPN connects directly to the DN, we used the connection strength. If the connection is through an intermediate neuron (i.e. two-hop), we used the square-root of the product of the input-normalised connection weights.

In Figure 4H, DNs reached within two hops were included, using a 2% input threshold – except for DNa02, DNae002 and pIP1, where a 0.5% threshold was used. AOTU008 did not meet the DN threshold but was included because its top two input partners are VES200m and VES202m. For Figure S4J, we extracted all the direct and two-hop connections from visual projection neurons in Figure 4H, to descending neurons with known functions or sexual dimorphism. We then filtered the pathways such that the direct connections are stronger than 1% normalized input of the postsynaptic cell type.

Edge normalization

Connections are either input- or output-normalized as defined in the text and figure legends.

Input normalization quantifies the relative contribution of each presynaptic partner to a postsynaptic neuron's total input. For a connection from neuron A to neuron B, input normalization is calculated as:

Input normalized strength = (synapses from A→B) / (total synapses received by B)

Output normalization quantifies how a presynaptic neuron distributes its synaptic output across its postsynaptic targets. For the connection from neuron A to neuron B, output normalization is calculated as:

Output normalized strength = (synapses from A→B) / (total synapses given by A)

Input normalization reveals the relative influence of individual presynaptic partners on their downstream targets, while output normalization reveals the specificity and distribution of synaptic outputs.

Definition of dimorphic edges

To define edges as either dimorphic or isomorphic (Figure 7), we first constructed a type-to-type graph for all cross-matched or sex-specific neurons with arbours in the central brain: superclasses *ascending_neuron*, *cb_intrinsic*, *cb_motor*, *cb_sensory*, *descending_neuron*, *endocrine*, *visual_projection* and *visual_centrifugal* for the male CNS and corresponding superclasses for FAFB/FlyWire. Connections made in the ventral nerve cord (VNC) of the male CNS were excluded. For FlyWire, we used the new synapse predictions[152] for materialization version 783 (available from https://codex.flywire.ai).

Connection weights (i.e. number of synapses) were divided up between the left and right hemisphere using the source neuron's soma (*somaSide*) as point of reference. For the small number of unpaired medial neurons that belong to neither side of the brain, we used the target's side if possible. For connections between unpaired medial neurons (i.e. where neither source nor target belong to the left or right hemisphere), we split the weight evenly between left and right. For sensory neurons, we used the side of the nerve through which their axons enter the nervous system. To align connection weights between the male and female datasets, we modeled the systematic differences between them using a simple principal component analysis (PCA), using only edges between isomorphic types. To make this more robust, we first removed outliers by computing a Mahalanobis-like distance in the 2D (weight in male versus female) space using median centering and MAD scaling, then excluded points with distance > 3.0. A PCA on the remaining data yielded a scaling factor of 0.79 which we applied to all male CNS edge weights for cross-dataset comparisons (i.e. there are generally more synapses in the male CNS; see Figure S7D).

This produced a table like this:

type_pre	type_post	weight_total male, scaled	weight_left male, scaled	weight_right male, scaled	weight_total female	weight_left female	weight_right female
AVLP532	CL110	14.22	6.32	7.9	20	12	8

To identify connections that are significantly different between male and female we used a t-statistic, i.e. the ratio of an estimate's departure from its hypothesised value to its standard error. We began by applying a square root transformation to the absolute

(scaled) synapse weights, as commonly used for count data to stabilise variance and reduce right skew. The t-statistic t_{AB} for a connection between cell types A and B is then defined as:

$$t_{AB} = \frac{(\underline{x}_m - \underline{x}_f)}{s_p \times \sqrt{\frac{1}{n_m} + \frac{1}{n_f}}},$$

where $\underline{x}_m$ and $\underline{x}_f$ are the means of the transformed (square root) number of synapses connecting A and B on the left and right hemisphere in male (m) and female (f), respectively.

The pooled standard deviation s_p is defined as:

$$s_p = \sqrt{\frac{(n_m - 1)s_m^2 + (n_f - 1)s_f^2}{n_m + n_f - 2}},$$

where s_m and s_f are the standard deviations of the transformed (square root) number of synapses between A and B for the left and right hemispheres in male and female, respectively. The number of observations (n_m and n_f) is 2: one from the left and one from the right hemisphere, so this expression for s_p simplifies to

$$s_p = \sqrt{\frac{s_m^2 + s_f^2}{2}}.$$

And the combined expression is therefore:

$$t_{AB} = \frac{\underline{x}_m - \underline{x}_f}{\sqrt{\frac{s_m^2 + s_f^2}{2}}} \text{ or } \frac{\sqrt{2}\,(\underline{x}_m - \underline{x}_f)}{\sqrt{s_m^2 + s_f^2}}.$$

From the t-statistic, p-values were calculated using a two-sided two-sample t-test with 2 degrees of freedom as implemented in scipy.stats.t.sf.[178] Where the left and right hemisphere weights agree exactly within both sexes, s_p is zero and the t-statistic diverges; we assigned these edges the limiting value $p = 0$ (153k edges, 4.1%, the large majority of which were present in only one sex and subsequently fell below the noise threshold; see below). The resulting p-values were adjusted to control the false-discovery rate using the Benjamini-Hochberg procedure as implemented in *scipy.stats.false_discovery_control*.

We considered all edges with $p \leq 0.1$ to be potentially dimorphic. Across all 3.76M edges between cross-matched neurons in the central brain, we find 179k edges (4.7%) with significant (FDR-corrected $p \leq 0.1$) male-female differences, 157k (4.1%) of which are highly significant (FDR-corrected $p \leq 0.01$). This pool of candidate dimorphic edges includes a number of edges with small but very consistent male-female differences. We therefore additionally apply a threshold of at least 30% difference which reduces the number of candidate dimorphic edges to 171k. As demonstrated previously,[30,180] we find that weak isomorphic connections are unstable: around 60% of single-synapse connections in one hemisphere are not at all present in another hemisphere from either the same or another brain (Figure S7E). To achieve a 90% probability of an isomorphic edge in the male also being present in the female dataset, it needs to consist of >10 synapses. In the opposite direction, that threshold is >7 synapses – likely due to the generally stronger edges in the male CNS. We consider edges below these thresholds to be unreliable and treat them as noise. Because edge weight distribution is heavily skewed with many weak edges (Figure S7B), around 80% of all cross-matched edges fall below these thresholds. Crucially though, the remaining above-threshold edges collectively contain 90% of all synapses in the male (89% in female) (Figures S7F and S7G).

For subsequent analyses (Figure 7F and following), this initial set of edge-level dimorphism labels was corrected using the cell type-level dimorphism labels: false-negatives (edges involving sex-specific types on either end) were set to ''dimorphic'', and likely false-positives (edges involving only isomorphic types) were set to ''isomorphic''. For the latter: 0.4% of all edges between two isomorphic cell types (12.9k) were flagged as significantly different between sexes, suggesting that some cell types may have evaded our initial neuron-level search. A manual review of the 500 isomorphic types that showed up most frequently led to fewer than 5 changes in dimorphism status. Rather, most differences in male-female connectivity were explained by segmentation issues or inconsistent cell type definitions across datasets. Given the available evidence that most of these edges are false-positives (i.e. not actually dimorphic), we excluded them from further consideration. Conversely, only 32% of all above-noise threshold connections involving sex-specific types on either end were flagged as dimorphic.

In summary, we would flag the need for expert review of the nodes (i.e. neurons) to draw robust conclusions as individual edge level statistics are both noisy and affected by technical artefacts of each individual dataset. Node level review simultaneously eliminated many false positives and allowed many true positives to be called, increasing the number of dimorphic edges from 29k → 48k. We believe that further refinements to these analyses are possible, including the use of population level rather than per edge variance estimates, and provide cross-matched type-to-type edge weights and inferred dimorphism labels in the accompanying github.com/flyconnectome/2025malecns repository.

GRAPH TRAVERSAL

We employed a probabilistic graph traversal model first published in Schlegel et al.[67] to calculate the distance from sensory inputs for isomorphic, dimorphic and sex-specific neurons (Figure 3L). Using a pool of all sensory neurons as seeds, the model pulls direct downstream partners and repeats the process until all nodes in the graph have been traversed. We used a linear function to determine the probability of traversal such that if neuron A makes up 30% or more of neuron B's inputs, there is a 100% chance of traversal. The chance of traversal for any neuron outside the pool connected to a neuron already in the pool is independent. We repeated the traversal 10,000 times and calculated the layers as the mean across all runs. The results of this analysis are provided in the accompanying github.com/flyconnectome/2025malecns repository.

OLFACTORY SYSTEM ANALYSIS

The *Drosophila* olfactory system consists of approximately 1,300 olfactory receptor neurons (ORNs) in each hemisphere grouped into 53 types according to their receptor expression profiles.[130,181–183] ORNs expressing the same receptors project to the same antennal lobe compartment, or glomerulus, where they synapse with second-order projection neurons (ALPNs) that carry sensory information from particular glomeruli to higher brain centres. Antennal lobe local neurons (ALLNs) provide lateral inhibition and excitation.[184] In parallel, the AL also integrates thermo- (heat) and hygro- (humidity) sensation in 7 distinct glomerular subcompartments in the AL (VP glomeruli, VP1-5) through their own receptor neurons (TRNs and HRNs, respectively). There are around 100 of these neurons grouped into 7 or 8 types.[185] We use "RNs" to collectively refer to olfactory, thermosensory, and hygrosensory receptor neurons, and "ORNs" when referring exclusively to olfactory neurons.

Sensory neurons are often difficult to reconstruct due to their fine calibre particularly as they cross the antennal commissure, and artifacts likely associated with truncation of their axons during specimen preparation. Receptor neurons (RNs) in the male CNS were no exception with reconstruction status summarised in Figure S6A. Almost all RNs are bilateral (projecting to homologous glomeruli in left and right antennal lobes) with the side of entry into the neuropil annotated as *rootSide*. We annotated 2,635 ORNs (53 types) and 91 T/HRNs (8 types). While the majority of RNs (~70%) were fully reconstructed, some neurons could not be followed as they crossed over the midline leaving two separate fragments for which the side of origin was uncertain. When quantifying the number of RNs we use the term 'neurons' when we have accounted for the duplication of bodies where their side of origin is unknown, and 'bodies' when we have not. However, even accounting for this, there appeared to be asymmetries in both neuron numbers and synapse numbers between the two hemispheres (Figure S6B). For these reasons we opted to use the total number of RNs in our analysis rather than presenting an interhemispheric comparison (our approach in most other parts of the CNS). Furthermore, for most of our analyses, we were able to leverage the hemibrain dataset to provide an additional data point. However, this comparison was not satisfactory since ~50% of glomeruli in that dataset are truncated and/or have fragmented RNs.[67]

In the male CNS we annotated 72 types of uniglomerular ALPNs (286 neurons) and 108 types of multiglomerular ALPNs (400 neurons) as well as 6 ALON types (14 output neurons which have distinctive morphology compared with classic ALPNs). References to ALPNs in the text include these ALONs. We defined pheromone ALPNs as receiving at least 5% input from pheromone ORNs and their uniglomerular PNs. To test whether ALPNs with high sex-specific or sexually dimorphic output ($\geq$10% of presynapses; Figure 6H) differ in their odour input composition, we first assigned each ORN/uPN to one of five mutually exclusive valence categories (adapted from ref[67]). For bootstrapping, we resampled (with replacement) the remaining set of ALPNs 1000 times, and for each sample calculated the mean percentage input received from ORNs/uPNs in each valence category. This produced a bootstrap distribution of means per category, which we compared with the observed values for the high sex-specific/dimorphic output group.

Gustatory system analysis

To compare the downstream synaptic partners of each GRN class, connectivity data were pooled across five sensory subtypes: leg bristle (local), leg bristle (ascending), labellar bristle, pharyngeal sensilla, and wing bristle (excluding taste pegs). For each subtype, partner identity, connection weight, sexual dimorphism classification, and neuron type were extracted and combined into a single dataset.

Connection weights were summed within each source–type–dimorphism grouping and normalised to the total synaptic weight per source, yielding a proportional connectivity measure. Partners belonging to other sensory neuron classes (labellar bristle, pharyngeal, wing, or leg neurons) were excluded from downstream analyses, as were partners lacking type annotations. Neurons were classified as either isomorphic or dimorphic according to metadata. Within each source–dimorphism combination, up to ten partner types with the highest proportional connectivity were included. The cell types for each class are as follows:

GRN class	sex-specific/dimorphic partners	isomorphic partners
Pharyngeal sensilla	AN05B035, GNG064, mAL_m10, DNg37, DNpe041, mAL_m4, AN10B009, GNG494, GNG702m, mAL_m9	GNG035, GNG406, GNG039, GNG319, GNG320, GNG001, GNG016, GNG014, GNG551, GNG022
Labellar bristle	AN09B017e, mAL_m10, mAL_m9, AN05B035, GNG064	ANXXX462a, GNG016, GNG038, GNG042, GNG087, GNG175, GNG229, GNG397, GNG453, GNG592
Leg bristle (ascending)	DNpe041, AN05B035, ANXXX151, mAL_m5a, AN05B102d, AN09B042, AN09B017d, AN09B017e, mAL_m9, mAL_m4	AN05B023a, GNG016, GNG195, AN27X021, ANXXX470, AN09B033, AN27X020, ANXXX196, Z_lvPNm1, mAL6
Leg bristle (local)	AN05B102c, AN05B035, ANXXX151, AN05B102d, ANXXX013, AN09B017d, AN09B017g, AN09B017f, AN09B017b, AN09B017e	AN05B102a, IN05B011a, AN13B002, IN05B002, AN05B023b, IN05B011b, AN05B023d, DNge153, IN01B065, AN05B023c
Wing bristle	AN05B102c, ANXXX151, AN05B102d, ANXXX013, IN12A002, ANXXX050, TN1c_a, IN10B013	IN05B011a, AN05B102a, AN13B002, IN05B002, AN05B023b, ANXXX093, AN05B023d, IN11A020, AN23B002, IN06B028

Network analyses

Hierarchical community detection

The hierarchical community structure is determined to analyse the contributions of isomorphic and dimorphic/sex-specific cell types in the network structure. Here, we fit a nested stochastic block model (SBM) to the data to infer partitions of nodes by their network connectivity. The SBM is a generative model for networks in which nodes are partitioned into blocks (or groups), and edges are placed between blocks according to block-specific connection probabilities. Given a particular partition, the likelihood that the observed network was generated under the model can be computed. To identify the best partition, this inference relies on the minimum description length (MDL) principle: the best model is the one that provides the most concise description of the data. In practice, this involves jointly encoding (i) the model parameters and assumptions (e.g., the block structure and probabilities) and (ii) the data given the model. The description length, measured in bits, is minimized when the model strikes the best trade-off between complexity (number of parameters) and goodness of fit (how well it explains the observed network). Importantly, this balance means that it does not overfit noisy data as is the case for modularity-maximization-based approaches.[158,186,187] The hierarchical partitions and the number of communities inferred are optimal by the above criteria. The procedure was employed with the male cell-type connectivity graph of the central brain, where the synapse counts (edge weights) are modelled with a discrete geometric distribution, as determined to be optimal in the larval brain.[188] The graph-tool library was used to run the hierarchical block assignment.[157,158] We first obtained a greedy nested block model assignment and performed 1000 iterations of 10 Markov Chain Monte Carlo (MCMC) merge-split sweeps to improve the solution.[189]

Cluster enrichment analysis

Our hierarchical block structure provides a set of clusters which we evaluate for statistically significant enrichment in male-specific or dimorphic types. We used the hypergeometric distribution to assign each cluster a probability of randomly drawing at least the observed number of non-isomorphic types. We calculated this probability for each cluster across the whole hierarchy. Then, using the Benjamini-Hochberg method accounting for the false discovery rate (FDR), we designated clusters as enriched at $\alpha = 0.01$. We obtained 12 enriched clusters of 311 at the highest granularity level (level 6). The cell type and neuron composition of all clusters at this level are available in the accompanying github.com/flyconnectome/2025malecns repository.

Optic lobe analysis

The annotation and analysis of the right optic lobe was previously presented in Nern et al.[39] We extended this to the left optic lobe, assigning each columnar neuron to a specific column and defining ROIs for columns and layers. We also improved the identification of pale and yellow columns in both hemispheres. Full details are provided in Data S1.

Neuron visualization

Three-dimensional neuron renderings to show whole-brain projection views and optic lobe slice-views (Figure 4; Data S1) were generated using the Blender-based pipelines developed in Nern et al.[39]

Comparison of edge weights in the optic lobes

Plots showing the percentage of inputs to the postsynaptic cells for pairs of connected cell types (for comparing males and females) or instances (for comparing the left and right optic lobe) in the optic lobes (Figure S4H; Data S1) include only connections with a combined synapse count above a threshold on at least one side of each comparison. Connection pairs that show high technical variability (e.g. those involving photoreceptors or cells in the lamina) or are entirely absent from one side of a comparison (i.e. sex-specific or present in only one optic lobe) are also omitted.

Eye maps for visual projection neuron analysis

For the spatial coverage heatmaps of visual projection neurons in Figures 4F and S4I, we first mapped the spatial locations of input synapses to column ROIs (described below). This spatial pattern together with the synapse count in each column was then visualized

on a new eye map, representing the visual field of the compound eyes. This eye map was based on the data and methods of Zhao et al.,[76] but extended to accommodate the medulla column ROIs in the male CNS brain.

Cell Type Explorer interactive web resources

The Cell Type Explorer web resource was substantially updated to include bilateral optic lobe analyses and expanded to encompass connectivity summaries for all central brain neurons. The web interface now features enhanced interactivity, enabling users to filter and sort connectivity tables and browse cell types across the entire male CNS connectome. The right optic lobe web resource will remain at its original URL: https://reiserlab.github.io/male-drosophila-visual-system-connectome/, while the updated version is hosted from https://reiserlab.github.io/celltype-explorer-drosophila-male-cns/.

Sex-specific branch analysis

For the analysis of sex-specific branches (Figures S3R and S3S) we examined ~120 dimorphic cell types. 46 types (135 individual neurons) with well-defined extra axonal or dendritic branches in the male were split into the isomorphic and male-specific parts (Figure S3R). We manually placed annotations in Neuroglancer to define cut points that would separate sex-specific from isomorphic branches. We then split skeletons for each of the 46 types using *navis* (see key resources table). All splits were manually inspected to confirm correctness.

QUANTIFICATION AND STATISTICAL ANALYSIS

This study reports one male CNS specimen with comparisons to two previously published datasets. In some instances, the two hemispheres of each specimen could be treated independently, but animal level statistical analysis was not possible. The unit of analysis is stated and is the neuron, cell type, type-to-type connection or network cluster rather than the animal. Statistical details, including tests, exact n and thresholds, are given in the method details subsections ''Definition of dimorphic edges,'' ''Cluster enrichment analysis,'' ''Graph traversal,'' and ''Olfactory system analysis,'' and in the legends of Figures 3, 6, and 7.

Edgewise dimorphism analysis used a two-sided two-sample t test on square-root-transformed, scaled edge weights with $n = 2$ per sex (one observation per hemisphere), the centre given by the mean across hemispheres, dispersion by the pooled standard deviation and 2 degrees of freedom, with Benjamini–Hochberg false discovery rate correction across all tested edges; cluster enrichment used the hypergeometric distribution with the same correction at alpha = 0.01; olfactory input composition was compared by bootstrap resampling (1000 iterations). We used non-parametric summaries for distributions (median, quartiles and 1.5 × interquartile range, as stated in the figure legends).

ADDITIONAL RESOURCES

A resource website linking to data artifacts and code and allowing interactive data exploration and queries is linked here: https://male-cns.janelia.org/.